NASA/TM–2001–104606, Vol. 20

Technical Report Series on Global Modeling and Data Assimilation

Max J. Suarez, Editor

Volume 20

The Climate of the FVCCM–3 Model

Yehui Chang, Siegfried D. Schubert, Shian-Jiann Lin, Sharon Nebuda, and Bo-Wen Shen

August 2001

Available from:

NASA Center for AeroSpace Information
7121 Standard Drive
Hanover, MD 21076–1320
Price Code: A17

National Technical Information Service
5285 Port Royal Road
Springfield, VA 22161
Price Code: A10

Abstract

This document describes the climate of version 1 of the NASA-NCAR model developed at the Data Assimilation Office (DAO). The model consists of a new finite-volume dynamical core and an implementation of the NCAR climate community model (CCM-3) physical parameterizations. The version of the model examined here was integrated at a resolution of 2° latitude by 2.5° longitude longitude and 32 levels. The results are based on a simulation that was forced with observed sea surface temperature and sea ice for the period 1979-1995, and are compared with NCEP/NCAR reanalyses and various other observational data sets. The results include an assessment of seasonal means, subseasonal transients including the Madden Julian Oscillation, and interannual variability. The quantities include the zonal and meridional winds, temperature, specific humidity, geopotential height, stream function, velocity potential, precipitaion, sea level pressure, and cloud radiative forcing.

Contents

List of Figures

1 Introduction

The NASA-NCAR GCM is part of the next generation Data Assimilation System (DAS) currently being developed within the Data Assimilation Office (DAO) of the Goddard Laboratory for Atmospheres. It is the follow-on to the GEOS GCM development – see the DAO's Algorithm Theoretical Basis Document (DAO 1996) for a description of the GEOS-2 DAS. The main characteristics of this new model-analysis system are described in da Silva and Lin (2001).

The NASA-NCAR GCM is being developed jointly by the DAO and the Climate and Global Dynamics Division (CGDD) at NCAR. The model is based on the finite-volume dynamical core developed at the DAO (Lin and Rood 1996, Lin and Rood 1997, Lin 1997, Lin and Rood 1998), with physical parameterizations from the NCAR CCM (Kiehl et al. 1996). The main features of the model are summarized in the next section.

This document describes the climate of the initial version of this model (internal version number 1.1.2d) consisting of the finite-volume dynamical core and an implementation of version three of the NCAR climate community model (CCM-3) physical parameterizations. The model was integrated at a resolution of 2° latitude by 2.5° longitude and 32 levels. The results are based on a single simulation for the period 1979-1995 forced with observed sea surface temperature and sea ice (Reynolds and Smith 1994). All output from the simulation was saved every 6 hours as instantaneous fields. All quantities presented here are based on daily mean values (the average of the four times daily values).

1.1 The NASA-NCAR Model

The finite-volume dynamical core has a horizontal discretization builtupon the Flux- Form Semi-Lagrangian (FFSL) transport algorithms (Lin and Rood 1996; Lin and Rood 1997). The vertical structure is based on the Lagrangian control-volume concept of Lin (1997) and Lin and Rood (1998). This physically based dynamical core allows circumventing many of the problems associated with sigma, pressure, or isentropic coordinates, increasing the physical integrity and computational efficiency of the model. The novel attributes of the dynamical core can be summarized as follows:

- Terrain-following Lagrangian control-volume vertical coordinate with a monotonicity-preserving and mass-, momentum-, and total energy-conserving mapping algorithm to the "fixed" Eulerian reference coordinate.
- Two-dimensional conservative flux-form semi-Lagrangian transport between two bounding "horizontal" Lagrangian surfaces that define the finite control-volume.
- Accurate representation of the terrain. Accurate and physically consistent finite-volume integration of pressure gradient force for the terrain-following Lagrangian control-volume.

- Highly adaptable and computationally efficient algorithm design for vector or RISC-based parallel computers.

The vertical coordinate consists of a hybrid sigma-pressure coordinate. The approximate pressure levels of the model used here are given in Table 1. We note that, while this version of the model has 32 levels, more recent versions of the model have additional levels to better resolve the stratosphere.

Table 1: Approximate pressure levels of the 32-layer model

L	mb	L	mb	L	mb	L	mb
1	0.7000	2	1.5000	3	2.8500	4	5.0000
5	8.1500	6	12.5500	7	18.3500	8	25.3000
9	32.9000	10	41.0750	11	50.2000	12	60.5613
13	72.2925	14	85.4390	15	100.5145	16	118.2502
17	139.1150	18	163.6615	19	192.5410	20	226.5135
21	266.4789	22	313.4988	23	368.8161	24	433.8927
25	510.4555	26	600.5238	27	696.7930	28	787.7000
29	867.1572	30	929.6455	31	970.5525	32	992.5550

The NCAR physical parameterizations represent a set of processes with a long history of development and documentation (Kiehl et al., 1996 for CCM3, Hack et al., 1993 for CCM2). The components of the CCM3 physics that are implemented in the initial version of the NASA/NCAR model consist of the following:

- Moist physics: M
  - deep convection (Zhang and McFarlane 1995) with updrafts and downdrafts
  - mid and shallow convection (Hack 1998)
  - large-scale condensation (Sundqvist 1988)
  - rain evaporation
- Radiation and clouds: R
  - Kiehl et al. 1994;1996
  - long wave computation includes CO2,O3,CH4,N2O,H2O,CFC11,CFC12
  - short wave computation includes a background aerosol (0.14 optical depth)
  - diagnostic clouds are a generalization of Slingo (1987)
- Land and Ocean surface: S
  - Land surface model (Bonan 1996)
  - Prescribed sea surface temperature

- Planetary Boundary Layer: T
  - first order closure scheme
  - local and non-local transport (Holtslag and Boville 1992)
- Gravity wave drag: W
  - McFarlane 1987

In the current setup of the model the dynamics and the physical parameterizations are operator-split as follows:

$$w_{n+1} = W(T(S(R(M(D(w_n))))))) \tag{1}$$

where w represents the prognostic variables (the state vector), D the finite-volume dynamical core, M the moist physics packages (cumulus convection with both updrafts and downdrafts, mid and shallow convection, and the large-scale condensation and rain re-evaporation), R the cloud and radiation packages (diagnostic clouds; short and long wave radiation schemes), S the surface models (prescribed sea-ice and SST; the land surface model), T the PBL mixing/turbulence parameterization, and W is the gravity wave drag parameterization. The model is effectively two-time-level with each operator (from D to W in alphabetic order) performing instant "adjustments" to the state vector w.

The next generation of CCM parameterizations (CCM4) will include prognostic cloud water, a revised radiation scheme, a new moist convection scheme, and the common land model (CLM). In addition, to allow higher vertical resolution, an improved cloud overlap specification scheme will be incorporated.

1.2 Verification Data

The upper air prognostic fields and their statistics are compared with the NCEP/NCAR reanalysis (Kalnay et al. 1995) averaged for the same period as the model simulation.

The precipitation fields are compared with the combined gauge and satellite estimates of Xie and Arkin (1997).

Outgoing long–wave radiation (OLR) is compared with the satellite estimates from the National Oceanic and Atmospheric Administration (NOAA) National Environmental Satellite, Data and Information Service. The OLR estimates have been computed for June 1974 to the present (Gruber and Kruger 1984) based on theoretical and empirical relationships between total flux and the 11 μm window radiance measurements. The measurements are from the scanning radiomenter in the NOAA 2–5 advanced very high radiation radiometer (AVHRR) instrument on TIROS–N and NOAA 6–10.

Cloud forcing is compared with estimates from the Earth Radiation Budget Experiment (ERBS) based on measurements from the ERBS, NOAA 9 and NOAA 10 satellites between

November 1984 and February 1990. We limit our comparsion to the years 1985-1989. More information on ERBE may be obtained from
(http://asd-www.larc.nasa.gov/erbe/ASDerbe.html).

Estimates of total precipitable water (TPW) are those generated by Wentz (1992) from the Special Sensor Microwave Imager (SSM/I) measurements. The radiative transfer algorithm uses three channels of microwave measurements (22V, 37V, 37H) and a model that accounts for absorption and emission in the atmosphere. The model uses a surface emissivity value over oceans appropriate for a wind–roughened sea surface. The model does not account for scattering by raindrops or by frozen hydrometers and is, therefore inaccurate for high rain rates. No calculation is done over land or sea ice, because of the complexity of the surface emissivity. These data are available starting in June 1987.

2 Results

In the following we present some selected results from the 17-year model simulation and compare them with observations and NCEP/NCAR analysis data. The discussion is meant to serve as a baseline evaluation of this version of the model, and to highlight those aspects of the simulation that require improvement. For some quantities, our verification data cover only a subset of the 17 years. In that case, the comparison with the model simulation is restricted to only those years. This is noted in the Figures.

The first section presents the seasonal mean fields, both as global maps and zonal means. The seasons are defined by the calendar months December-January-February (DJF), March-April-May (MAM), June-July-August (JJA), and September-October-November (SON). The quantities consist of the zonal wind, eddy (deviations from the zonal mean) height, eddy stream function, velocity potential, sea level pressure, precipitation, surface temperature, short- and long- wave cloud forcing, total precipitable water, and outgoing long wave radiation. The next section shows the interannual variability of the seasonal mean fields, including the 50mb, 200mb, and 850mb zonal wind, the 300mb height, 200mb stream function, 200mb velocity potential, sea level pressure, and precipitation. The subsequent sections deal with variability on sub-seasonal time scales, including all sub-monthly, 2.5-6 day, and 10-30 day time scales. The quantities include, the height field, kinetic energy, and northward momentum and heat fluxes. The last section of the results examines tropical variability with time scales of 20-90 days. The analysis includes a complex empirical orthogonal function decomposition and a wavelet decomposition to help assess the ability of the model to represent the Madden-Julian Oscillation (Madden and Julian 1972).

2.1 Seasonal Means

Overall the model does a good job in capturing the seasonal cycle of the zonal mean zonal and meridional wind fields (Figures 1-6). The model does show some tendency to produce too strong westerlies in the Southern Hemisphere and too strong tropical easterlies during all seasons. The seasonal cycle of the zonal mean temperature and humidity (Figures 7-12) is also generally reasonable, though the polar regions (especially the southern hemisphere)

are generally too cold between about 400 and 100mb. The model is consistently drier than the reanalysis in the boundary layer, and wetter than the reanalysis in the tropics above the boundary layer. It should be noted that for the reanalysis data, the quality of both the zonal mean meridional wind and the specific humidity is suspect since these are highly dependent on the model used in the assimilation system, and therefore impacted by model bias. The main difference between reanalysis and the simulated mass stream function (Figures 13-15) is the tendency for the model to have a stronger lower and mid tropospheric circulation.

The zonal wind is well simulated at both 50mb (Figures 16-17) and 200mb (Figures 18-19). At 200mb during DJF, the main deficiencies are a somewhat too strong westerly saddle in the eastern tropical Pacific, and a North American jet that is too strong. During the transition seasons, the east Asian jet is retracted compared with the reanalysis. In the Southern Hemisphere, the stronger zonal mean westerlies mentioned earlier, manifest themselves at 200mb as a more zonally elongated jet in the South Pacific, compared with the reanalysis, especially during JJA and SON when it extends eastward across South America. At 850mb (Figures 20-21) the Southern Hemisphere westerlies are generally too strong, and the east Asian westerly summer monsoon flow does not extend far enough to the east across Indo-China. Over the Pacific, the tropical easterlies tend to be too strong during all seasons.

The model produces realistic stationary wave patterns during DJF and MAM (Figures 22-23), though the amplitude of the east Asian trough tends to be somewhat weaker than in the reanalysis. During JJA the high latitude wave one pattern is stronger than that in the reanalysis. The 200mb eddy stream function (Figures 24-25) is generally well simulated. The main difference from the reanalysis is the tendency for the model to produce weaker anticyclones in the eastern hemispheres northern subtropics.

While the model generally reproduces the main features of the velocity potential field (Figures 26-27), the minimum over the Indonesia and the western tropical Pacific during JJA is much too weak compared with the reanalysis. This would suggest a weak east Asian monsoon, and is consistent with the retracted low level monsoon westerlies mentioned earlier. This problem is also evident during SON.

The simulation reproduces the basic seasonal evolution of the sea level pressure (Figures 28-29). During DJF the Aleution low is, however, somewhat weak and shifted to the west. Also, the North Pacific and North Atlantic anticyclones during JJA tend to be too strong. In the Southern Hemisphere, the climatological high pressure belt near 30° is somewhat too zonal and has maximum pressures higher than those found in the reanalysis.

The simulated and observed precipitation (Xie and Arkin 1997) are shown in Figures 30 and 31, respectively. During DJF the simulated precipitation over the Indian Ocean and western Pacific tends to lie north of the equator, while the observed maximum precipitation tends to lie south of the equator. The model also appears to have excessive precipitation over the Andes Mountains between the equator and 30°S during DJF. During JJA the model has insufficent precipitation over Indochina, and much of the Pacific warm pool region, consistent with the weaker velocity potential field noted earlier (this problem continues into the next season, SON). Also, the heaviest east Asian monsoon precipitation extends too far north across eastern China. During MAM the model produces a somewhat exaggerated

split in the Pacific InterTropical Convergence Zone (ITCZ).

The overall distribution and seasonal evolution of the simulated shortwave cloud radiative forcing is quite realistic (Figures 32-33). The model appears to capture the short wave cloud forcing associated with the west coast marine stratus clouds. Some of the main regional deficiences include insufficient DJF cloud forcing in the South Pacific Convergence Zone, a weak Pacific ITCZ during MAM, and too much shortwave cloud forcing over the subtropical anticyclones. The model longwave cloud forcing distribution is also quite good (Figures 34-35). The main deficiencies are the weak cloud forcing over the Pacific warm pool, and excessive cloud forcing over the western Indian Ocean during JJA. Similar results are obtained from a comparison of the simulated and observed outgoing longwave radiation (OLR) in Figures 36-37.

Figures 38-39 compare the simulated total precipitable water (TPW) against SSM/I for July 1987 through January 1992. The model tends to be dry throughout much of the tropics. The unrealistic split in the Pacific ITCZ during MAM mentioned earlier for the precipitation is also evident in the TPW field.

2.2 Interannual Variability of Seasonal Means

In this section we present the global distribution of the interannual variability of selected seasonal mean fields. At each grid point the unbiased estimate of the variance of a quantity x is computed as

$$s_{IA}^2 = 1/(N-1)\sum_{i=1}^{N}(x_i - \overline{x})^2, \tag{2}$$

where x is the mean over the N years.

Figures 40-41 show the interannual standard deviation (s) in the 50mb zonal wind. The model shows no evidence of the relatively large tropical interannual variability evident in the reanalysis during all seasons. At 200mb (Figures 42-43) the model produces realistic DJF variability over the Pacific Ocean, though the region of maximum variability over the North Pacific is displaced somewhat to the north and west of the reanalysis values. Also for DJF, the model produces excessive variability over the eastern United States and the Gulf of Mexico. During JJA, the model produces greater than observed variability over the tropical eastern Pacific and Atlantic Oceans. At 850mb (Figures 44-45), the model produces excessive JJA zonal wind variance over the Indian Ocean, and unrealistically large variance over and just west of central America.

The comparison of the 300mb height standard deviation (Figures 46-47), indicates that the model produces a reasonable spatial distribution and seasonal evolution of the variance. The main discrepancy with the reanalysis data is the larger variance over the North Pacific, North America and the North Atlantic regions during DJF. Similar results are obtained from the comparison of the standard deviation of the 200mb streamfunction (Figures 48-49).

The interannual standard deviation of the velocity potential is shown in Figures 50 and 51, for the model and reanalysis, respectively. The model has much larger variance than the reanalysis over the eastern Pacific and western Indian Ocean during JJA and SON. Also, the reanalysis shows variance maxima over Indonesia during DJF, MAM and SON, that are too weak in the model. The OLR variance fields (Figures 52-53) show that the model tends to produce too much variability throughout the tropics, during all seasons.

Figures 54-55 compare the simulated and observed interannual standard deviation in precipitation. The general pattern of high variability in the tropics is reasonably well reproduced by the model. During DJF and MAM the model, however, tends to extend the region of high tropical Pacific variability too far east. Also, during JJA the model produces excessive variability in the Indian Ocean south of the equator, while there is too little variability over the Pacific warm pool.

Figures 56-57 show the simulated and observed interannual standard deviation in sea level pressure. The basic regions of high variability are well simulated by the model. There is some tendency to produce too much variability over the North Pacific and North Atlantic during DJF.

2.3 Intra-monthly Variability

In this section we focus on sub-monthly variability. We begin by examining the total variability with time scales less than one month (but greater than 1 day). The subsequent subsection isolates the contributions to the sub-monthly variability coming from time scales between 2.5 and 6 days, and time scales between 10 and 30 days. These frequencies are isolated by applying band-pass digital filters similar to those of Blackmon (1976) to the daily data (see also Schubert 1986).

2.3.1 Total

The total sub-monthly variability is computed for each season as

$$s^2_{SM} = 1/N \sum_{i=1}^{N} \left(1/3 \sum_{j=1}^{3} (s^2(j) \right)_i , \tag{3}$$

where

$$s^2(j) = 1/(M-1) \sum_{k=1}^{M} (x_k(j) - \overline{x}(j))^2. \tag{4}$$

Here $x_k(j)$ is the kth daily mean value for month j, $\overline{x}(j)$ is an average of x for month j, M is the number of days in the month, and the subscript i indicates a sum over the N years. The sum over j in (3) is computed for the 3 calendar months of each season.

Zonal Means

The zonal mean submonthly variability in the height field is quite good (compare Figures 58-59). The simulated zonal mean transient kinetic energy (Figures 60-61) is also quite good. The main difference from the reanalysis is a general tendency to underestimate the maxima in the northern hemisphere. The zonal mean northward zonal momentum transport (Figures 62-63) is also well simulated, though the model tends to overestimate the peak values in both hemispheres. The model reproduces the reanalysis zonal mean northward sensible heat transport quite well (Figures 64-65).

Global Distribution

The spatial distribution of the submonthly variability in the 300mb height field is well reproduced by the model (Figures 66-67). The model also produces a good overall distribution of the 200mb sub-monthly kinetic energy (KE, Figures 68-69). The simulated KE is, however, somewhat weak over the northern middle latitude oceans and the region of maximum KE over Australia and the western South Pacific is placed too far to the east during the colder seasons. The model produces a good overall distribution of the northward zonal momentum transport at 200mb (Figures 70-71). The main difference from the reanalysis is a tendency for too strong transports from the sub-monthly transients throughout the middle latitudes of both hemispheres (see also the zonal means in previous subsection). The northward sensible heat flux at 850mb due to the sub-monthly transients (Figures 72-73) is also good. One exception is the poorly defined signature of the North Pacific storm track during JJA and SON.

2.3.2 Filtered Fields

In this section we take a brief look at some band-pass statistics. In this case, the variances are computed as define in (3), however, the daily fields are first filtered to retain only time scales between either 2.5 to 6 days, or 10-30 days as described above.

Figures 74-75 together with Figures 82-83 show that the model does a good job of partitioning the 300mb height variability between synoptic (2.5-6 days) and low frequency (10-30 days) variability. One discrepancy is that during DJF the model underestimates the 2.5-6 day variance maximum associated with the east Asian storm track.

Comparing Figures 75-76 with Figures 84-85, we see that the model does a reasonable job in partitioning the 200mb kinetic energy between the synoptic (2.5-6 days) and low frequency (10-30 days) time scales. It is interesting that at 2.5-6 days, the model tends to underestimate the KE in the Northern Hemisphere, but it overestimates the KE in the Southern Hemisphere. We also see that the cold season eastward displacement of the region of maximum KE over Australia and the western South Pacific noted earlier is primarily in the lower frequencies.

Turning to the zonal momentum fluxes, the model has too much southward transport in the Southern Hemisphere at 2.5-6 days (compare Figures 78 and 79), though, overall, the simulated momentum transports are reasonable in both frequency ranges (see Figures 78,

79, 86 and 87). The simulated 850mb northward sensible heat fluxes also show a very realistic partitioning between the synoptic and low frequency submonthly time scales (compare Figures 80-81 with 88-89).

2.4 The Madden-Julian Oscillation

The Madden-Julian Oscillation (MJO) is the dominant mode of subseasonal variability in the tropics, and occurs on time scales of about 30-60 days. The MJO is clearly evident in the velocity potential field as a large-scale (zonal wave number 1) eastward propagating mode, that occurs in conjunction with eastward evolving convective anomalies in the tropical eastern hemisphere. The MJO has substantial impacts on short-term climate variability throughout the tropics and subtropics, and these may extend into middle latitudes.

In this section, we isolate that part of the variability in the 200mb velocity potential field that is largely tied to the MJO by filtering in both time and space. For the former we employ a Fourier transform to retain time scales between 20 and 90 days. For the latter, we employ a complex empirical orthogonal function (CEOF) decomposition (see below). The time series of the dominant CEOF is decomposed using a wavelet analysis. Various other fields are composited during a typical cycle of the first CEOF. The composites are computed over those times when the modulus of the first CEOF of the 200mb velocity potential exceeds one standard deviation.

2.4.1 Data processing

The data used in this analysis consist of the daily 200 mb velocity potential, 200mb streamfunction, outgoing longwave radiation (OLR) and total precipitable water. A Fourier spectral transform was used to remove time scales shorter than 20 days and longer than 90 days.

The CEOF decomposition is done following (Pfeffer et al. 1990). For a time series, $\psi(x, y, t)$, we obtain

$$\psi(x, y, t) = \frac{1}{2} \sum_{k=1}^{K} (\Psi_k(y, t) e^{-ikx} + \Psi_k^*(y, t) e^{ikx}), \tag{5}$$

where x is the longitude, t is time, k is the wavenumber, $2K + 1$ is the number of equally spaced points around the longitude circle at which ψ is specified in y, $\Psi_k(y, t)$ is the Fourier transform of $\psi(x, y, t)$ and the asterisk denotes a complex conjugate. We then seek orthogonal function expansion of $\Psi_k(y, t)$ of the form

$$\Psi_k(y, t) = \sum_{p=1}^{N} A_p(t) C_p(y, k), \tag{6}$$

in which we impose the condition, $\sum_{n(k,y)}^{N} C_p(y, k) C_q^*(y, k) = \delta_{p,q}$ for orthonormality of the basis functions. Here, $\delta_{p,q}$ is the Kronecer delta. $A_p(t)$ are determined by projecting $\Psi_k(y, t)$

onto $C_p(y,k)$, then we have

$$A_p(t) = \sum_{n(k,y)=1}^{N} \Psi_k(y,t) C_p^*(y,k). \tag{7}$$

We determine $C_p(t)$ by maximizing the variance of the largest component subject to the eigenvalue problem

$$\sum_{m=1}^{N} C_{n,m} C_p(m) = \lambda_p C_p(n), \tag{8}$$

where $C_{n,m} = \overline{\Psi_k(y,t)\Psi_k^*(y,t)}$ is the covariance matrix and the eigenvalue λ_p is real and the eigenvector $C_p(n)$ is the complex empirical orthogonal function (EOF). We may express $\psi(x,y,t)$ as follows:

$$\psi(x,y,t) = \frac{1}{2}\sum_{p=1}^{N}[A_p(t)B_p^*(x,y) + A_p^*(t)B_p(x,y)]. \tag{9}$$

where

$$B_p(x,y) = \sum_{k=1}^{K} C_p^*(y,k) e^{ikx}. \tag{10}$$

By expressing the complex functions $A_p(t)$ and $B_p(y,k)$ in terms of their moduli and phases, we may write (9) in the form

$$\psi(x,y,t) = \sum_{p=1}^{N} \alpha_p(t)\beta_p(x,y) cos(\theta_p(x,y) - \phi_p(t)), \tag{11}$$

here $A_p(t) = \alpha_p(t)e^{i\phi_p(t)}$ and $B_p(t) = \beta_p(x,y)e^{i\theta_p(x,y)}$. The expression of the phase angles, $(\theta_p(x) - \phi_p(t))$ determines only to within an arbitrary constant which can be added to one and subtracted from the other without changing their difference. Each component of (11) may be thought of as representing a wave with shape $cos\theta_p(x,y)$ and time dependent phase $\phi_p(t)$, the amplitude of which is modulated in phase space by $\beta_p(x,y)$ and in time by $\alpha_p(t)$. At a fixed position (x,y), the number of highs or lows per unit time is a measure of local frequency $d\phi_p(t)/dt$. At a fixed time t, the number of highs or lows of this function per increment of longitude is a measure of the local wavenumber $d\theta_p(x,y)/dx$. $\psi_p(x,y,t)$ depicts the shape and motion of the wave and the spatial and temporal modulations of its amplitude, wavenumber and frequency.

The above CEOF decomposition provides an efficient spatial representation of a traveling disturbance such as the MJO. Since the MJO tends to occur episodically and on a broad range of time scales, the temporal behavior of the MJO is best represented in terms of a wavelet decomposition. The wavelet transform (e.g. Weng and Lau 1994)is based on the convolution of a time series, $f(t)$, with a set of functions derived from a prototype $\psi(t)$. If $\psi(t)$ is admissible and $f(t)$ is square integrable, the continuous wavelet transform, $\mathcal{W}_f(a,\tau)$, is defined as,

$$\mathcal{W}_f(a,\tau) = \int f(t)\ \psi_{a,\tau}^*(t)dt\ , \tag{12}$$

where a, τ are real and $a > 0$, a is the scale parameter and τ is the translation parameter. The $\psi^*_{a,\tau}(t)$ is the conjugate of the transformed and dilated "basic wavelet" which is given by

$$\psi_{a,\tau}(t) = \frac{1}{\sqrt{a}} \psi\left(\frac{t-\tau}{a}\right) , \tag{13}$$

where the constant $\frac{1}{\sqrt{a}}$ is used for energy normalization.

The basic wavelet used in this study was designed by Morlet (1983) and has since been used in many studies

$$\psi(t) = e^{i\xi_o t}\, e^{-t^2/2}, \tag{14}$$

where ξ_o equals $\pi(2/ln2)^{1/2}$ in order to satisfy the admissibility condition. In Fourier space, this wavelet is given by,

$$\hat{\Psi}(\xi) = \frac{1}{2\pi}\, e^{-(\xi-\xi_o)^2/2} . \tag{15}$$

In our application the input function $f(t)$ to the wavelet transform is the complex time series associate with the first CEOF of the 200mb velocity potential field.

2.4.2 Results

We begin by showing in Figure 90 the variance of the 20-90 day filtered 200mb velocity potential averaged over all seasons for 1979-95. The simulated variability is considerably less than that found in the reanalysis, especially west of the dateline over the Pacific warm pool region and the Indian Ocean. Figure 91 shows the spatial pattern and eastward propagation of the first CEOF of the 20-90 day filtered 200mb velocity potential from the reanalysis and model simulation. The figure shows the evolution of CEOF 1 as it goes through one complete cycle, though note that the zero and positive lags are basically a repeat of the negative lags with reversed sign. The model produces a reasonably good simulation of the zonal wave 1 structure and eastward propagation. The reanalysis, however, shows a stronger east-west asymmetry with anomalies over the Indian Ocean and Indonesia that are stronger than those over the western hemisphere. Also, the first mode explains 3/4 of the filtered variance in the reanalysis, while the first mode explains about 1/2 the variance for the model.

Figures 92 and 93 show the modulus of the wavelet decomposition of the first CEOF for the model and reanalysis. The results show clearly the episodic nature of the MJO. The results from the reanalysis shows, as expected, that the MJO tends to have much of its power on time scales between 30 and 60 days, though there are clearly times when it has both shorter and longer time scales. For the model CEOF 1 has less of a preference for 30-60 days, and tends to have more variability at shorter time scales as is common for many AGCMs.

Figures 94-96 show composites of various quantities using the amplitude of the first velocity potential CEOF time series as an index. Only time periods when the amplitude exceeds one standard deviation (the MJO is considered active) contribute to the composites. Figure 94 shows the composite evolution of the OLR. The reanalysis/observations show a strong coupling between the velocity potential and OLR over the Indian Ocean and wetsern Pacific. The simulation shows a much weaker coupling. The composite evolution of the TPW

(Figure 95) shows, for the reanalysis, a clear signal of enhanced moisture on the leading edge of the region of rising motion (negative velocity potential anomaly): this apparently contributes to the eastward development of the MJO. The model results show less organized moisture anomalies linked to the evolution of the first CEOF. Finally, Figure 96 shows the model and reanalysis composite evolution of the 200mb stream function associated with the first velocity potential CEOF. This shows, for the reanalysis, a substantial Rossby wave component associated with the MJO, while for the simulation it is rather weak. This is not surprising in view of the model's weak coupling with convection in the western Pacific and Indian Oceans associated with the first CEOF (see Figure 94).

3 Conclusions

The results presented in this atlas shows that, overall, the FV-CCM3 model produces a very good simulation of the seasonal mean climate and its variability. The model does particularly well at simulating the zonal mean and spatial distrution of the subseasonal transients , the seasonal mean cloud radiative forcing, and the seasonal mean upper tropospheric/lower stratospheric zonal wind.

The primary deficiencies are in the simulation of the JJA divergent circulation and precipitation associated with the south Asian summer monsoon. Most notable is the deficient precipitation over the Pacific warm pool region. Like many GCMs, this model has insufficient interannual variability in the tropical lower stratosphere, and it is deficient in the representation of MJO and its coupling with convection over the western Pacific and Indian Oceans.

Despite these deficiencies, we feel this initial version of the model is a very good system with which to carry out data assimilation and climate simulation studies. It also serves as a valuable benchmark for assessing the impact of on-going model improvements such as the current implementation of the next generation (CCM-4) of physical parameterizations.

References

Blackmon, M.L., 1976: A climatological spectral study of the 500mb geopotential height of the Northern Hemisphere. *J. Atmos. Sci.*, **33**, 1607-1623.

Bloom, S.S., L.L. Takacs, A. M. da Silva, and D. Ledvina, 1996: Data Assimilation Using Incremental Analysis Updates. *Mon. Wea. Rev.*, **124**, 1256-1271.

Bonan, G.B., 1996: A land surface model (LSM version 1.0) for ecological, hydrological, and atmospheric studies: technical description and user's guide. NCAR tech. Note NCAR/TN-417+STR, 150 pp. [Available from National Center for Atmospheric Research, Boulder, CO 80307.]

Cohn, S. E., A. da Silva, J. Guo, M. Sienkiewicz, D. Lamich. 1998: Assessing the Effects of Data Selection with the DAO Physical-space Statistical Analysis System. *Mon. Wea. Rev.*, **126**, 2913-26.

DAO, 1996: Algorithm Theoretical Basis Docoment for Goddard Earth Observing System Data Assimilation System (GEOS DAS) With a Focus on Version 2. Available on-line from http://dao.gsfc.nasa.gov/subpages/atbd.html.

Da Silva, A. and S.-J. Lin, 2001: The DAO Physical-space/Finite-volume Data Assimilation System. Part I: Algorithm Theoretical Basis for the "Violet" Core System. DAO Office Note. In preparation.

Gates, W. Lawrence, 1992: AMIP: The Atmospheric Model Intercomparison Project. *Bull. Am Met. Soc.*, **73**, 1962-1970

Gruber, A. and A.F. Krueger, 1984: The status of the NOAA outgoing longwave radiation data set. *Bull. Amer. Meteor. Soc.*, **65**, 958-962.

Hack, J. J., 1998: Sensitivity of the simulated climate to a diagnostic formulation for cloud liquid water. *J. Climate*, **11**, 1497-1515.

Hack, J. J., B. A. Boville, J. T. Kiehl, P. J Rasch and D. L. Williamson, 1993: Description of the NCAR Community Climate Model (CCM2). *NCAR Technical Note*, **NCAR/TN-382+STR**, Boulder, CO, 108 pp.

Holtslag, A. A. M., and B. A. Boville, 1993: Local versus nonlocal boundary-layer diffusion in a global climate model. *J. Climate*, **6**, 1825-1842.

Kalnay, E., M. Kanamitsu, R. Kistler, W. Collins, D. Deaven, J. Derber, L. Gandin, S. Sara, G. White, J. Woollen, Y. Zhu, M. Chelliah, W. Ebisuzaki, W. Higgins, J. Janowiak, K. C. Mo, C. Ropelewski, J. Wang, A Leetma, R. Renolds, R Jenne, 1995: The NMC/NCAR Reanalysis Project. *Bull. Amer. Meteor. Soc.*, **77**, 437-471.

Kiehl, J.T., J.J. Hack, and B. P. Briegleb, 1994: The simulated earth radiation budget of the NCAR CCM2 and comparisons with the Earth Radiation Budget Experiment (ERBE). *J. Geophys. Res.*, **99**, 20815-20827.

Kiehl, J. T., J. J. Hack, G. B. Bonan, B. A. Boville, B. P. Briegleb, D. L. Williamson, and P. J. Rasch 1996: Description of the NCAR Community Climate Model (CCM3). *NCAR Technical Note*, **NCAR/TN-420+STR**, Boulder, CO, 152pp.

Lin, S.-J., 1997: A finite-volume integration method for computing pressure gradient forces in general vertical coordinates. *Q. J. Roy. Met. Soc.*, **123**, 1749-1762.

Lin, S.-J., and R. B. Rood, 1997: An explicit flux-form semi-Lagrangian shallow water model on the sphere. *Q. J. Roy. Met. Soc.*, **123**, 2477-2498.

Lin, S.-J., and R. B. Rood, 1996: Multidimensional Flux Form Semi-Lagrangian Transport schemes. *Mon. Wea. Rev.*, **124**, 2046-2070.

Lin, S.-J., and R. B. Rood, 1998: A Flux-form semi-Lagrangian general circulation model with a Lagrangian control-volume vertical coordinate. The Rossby-100 symposium, Stockholm, Sweden.

Madden, R. A. and P. R. Julian, 1972: Description of global scale circulation cells in the tropics with a 40-60 day period. *J. Atmos. Sci.*, **29**, 1109-1123.

McFarlane, N. A., 1987: The effect of orographically excited wave drag on the general circulation of the lower stratosphere and troposphere. *J. J. Atmos. Sci.*, **44**, 1775-1800.

Molod, Andrea, H.M. Helfand, and L.L. Takacs, 1996: The Climatology of Parameter- ized Physical Processes in the GEOS-1 GCM and their Impact on the GEOS-1 Data Assimilation System. *J. Climate*, **9**, 764-785.

Morlet, J., 1983: Sampling theory and wave propagation. NATO ASI Series, FI, Springer, 233-261.

Pfaendtner, J., S. Bloom, D. Lamich, M. Seablom, M. Sienkiewicz, J. Stobie, and A. da Silva, 1995: Documentation of the Goddard Earth Observing System (GEOS) Data Assimilation System - Version 4. *NASA Tech. Memo. 104606*, **4**.

Pfeffer, R. L., J. Ahlquist, R. Kung, Y. Chang and G. Li, 1990: A study of baroclinic wave over bottom topography using complex principal component analysis of experimental data. *J. Atmos. Sci.*, **47**, 67-81.

Reynolds, W. R. and T. M. Smith, 1994: Improved global sea surface temperature analyses using optimum interpolation. *J. Climate*, **7**, 929-948.

Schubert, S. D., 1986: The structure, energetics and evolution of the dominant frequency-dependent three-dimensional atmospheric modes, *J. Atmos. Sci.*, **43**, 1210-1237.

Schubert, S. D., J. Pfaendtner and R. Rood, 1993: An assimilated data set for Earth Science applications, *Bull. Am Met. Soc.*, **74**, 2331-2342.

Slingo, J. M., 1987: The development and verification of a cloud prediction scheme for the ECMWF model. *Quart. J. Roy. Meteor. Soc.*, **113**, 899-927.

Sundqvist,H., 1988: Parameterization of condensation and associated clouds in models for weather prediction and general circulation simulation. *Physically Based Modelling and Simulation of Climate and Climate Change*, M.E. Schlesinger, Ed., Vol. 1, Kluwer Academic Publishers, 433-461.

Weng, H. and K.-M. Lau, 1994: Wavelets, period doubling, and time-frequency localization with application to organization of convection over the tropical western Pacific. *J. Atmos.Sci*, **51**, 2523-2541.

Wentz, F., 1994: User's Manual, SSM/I Geophysical Tapes. Remote Sensing Systems, 11 pp.

Xie, P. and P. Arkin, 1997: Global precipitation, a 17-Year monthly analysis based on gauge observations, satellite estimates and numerical model outputs. *Bull. Am. Met. Soc.*, **78**, 2539-2558.

Zhang, G. J., and N. A. McFarlane, 1995: Sensitivity of climate simulations to the parameterization of cumulus convection in the Canadian Climate Centre general circulation model. *Atmos.-Ocean*, **33**, 407-446.

SEASONAL MEAN ZONAL MEANS

Zonal wind

Meridional wind

Temperature

Specific Humidity

Mass stream function

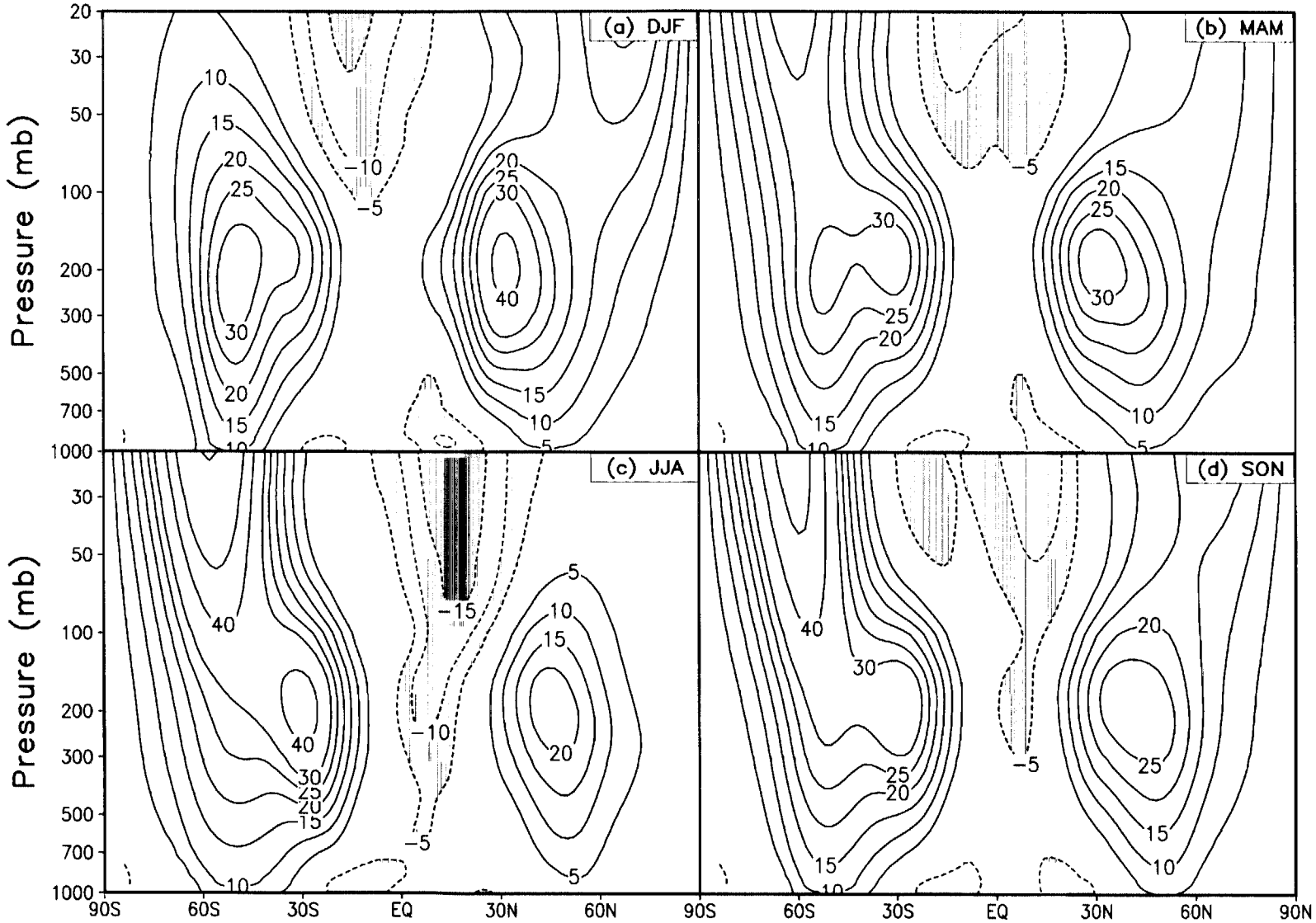

Figure 1: Seasonal means of zonally averaged u-wind for the model. The contour intervals are ± 5, 10, 15, 20, 25, 30, 40, 50 m s^{-1}. Negative values are shaded.

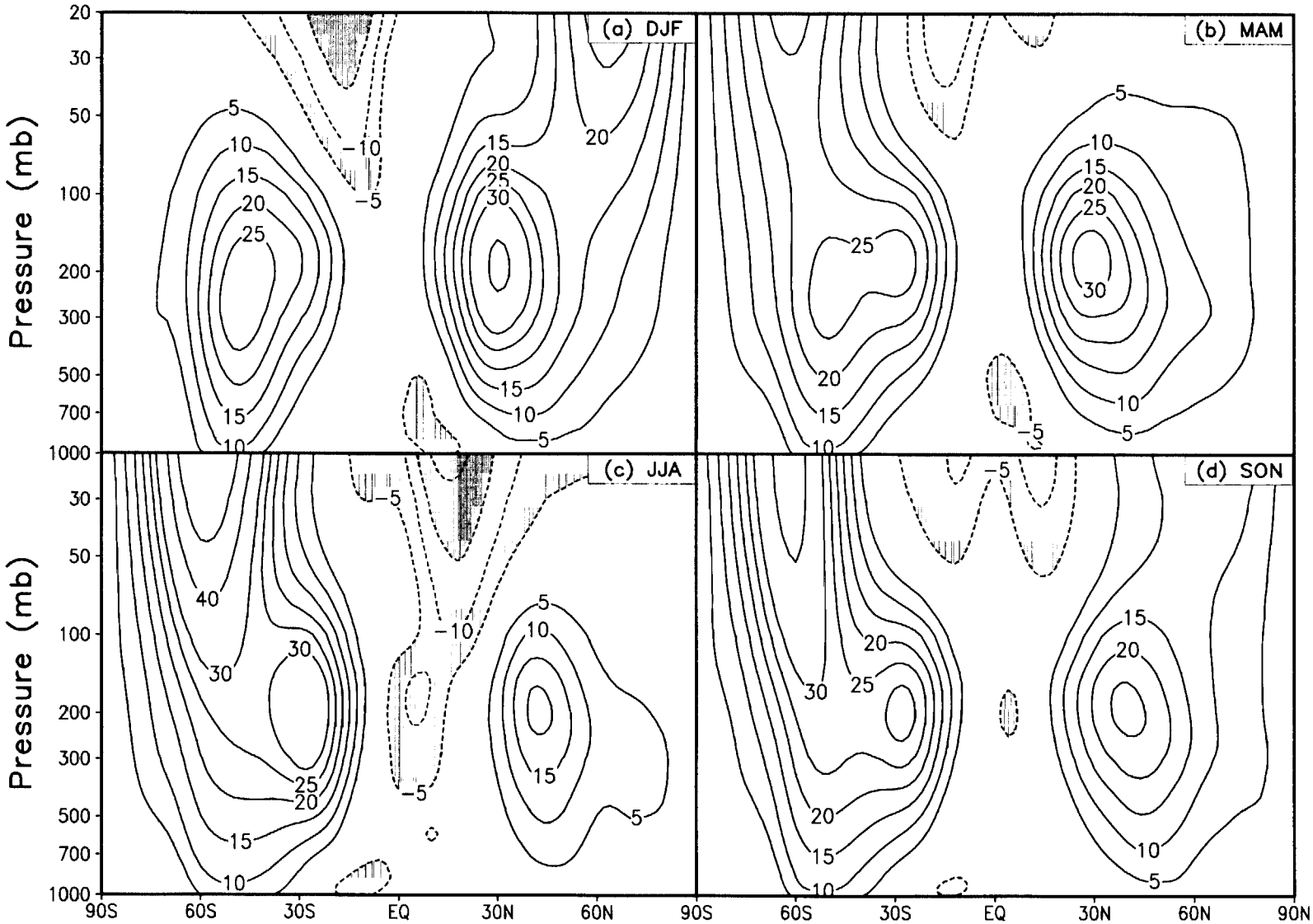

Figure 2: Seasonal means of zonally averaged u-wind for the reanalysis. The contour intervals are ± 5, 10, 15, 20, 25, 30, 40, 50 m s^{-1}. Negative values are shaded.

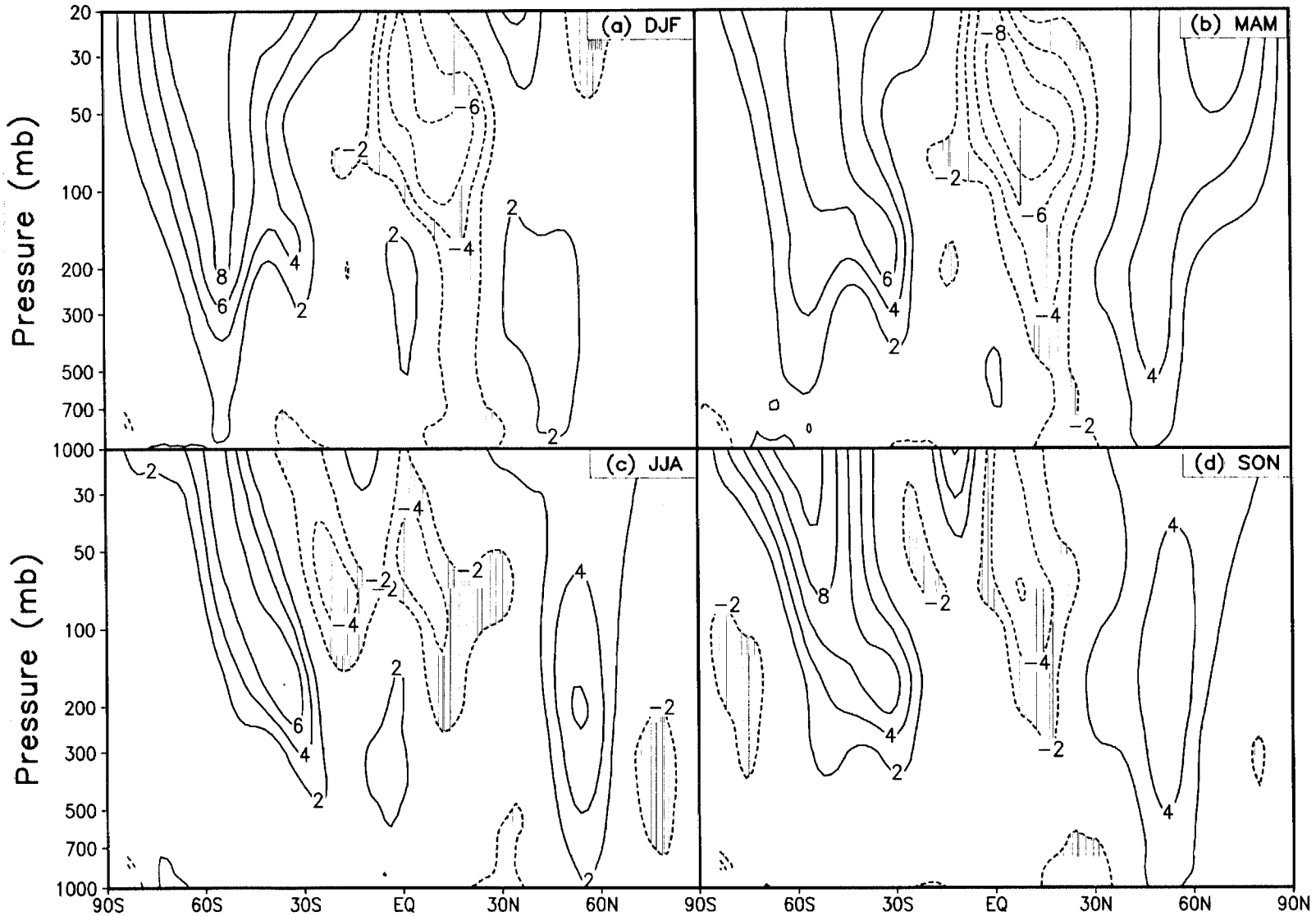

Figure 3: Seasonal means of zonally averaged u-wind difference between the model and the reanalysis. The contour interval is 2 m s^{-1}. Negative values are shaded.

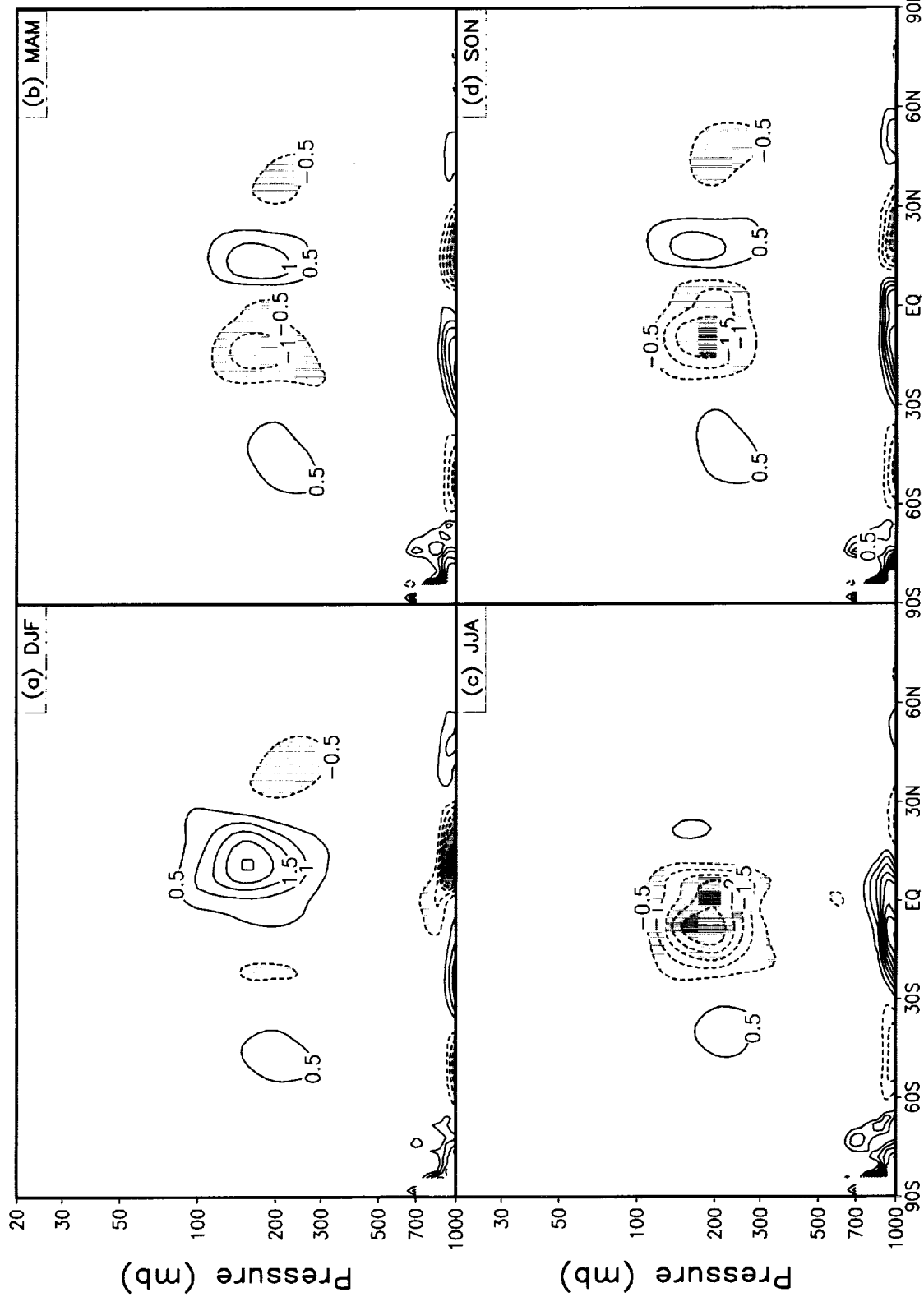

Figure 4: Seasonal means of zonally averaged v-wind for the model. The contour interval is 0.5 m s^{-1}. Negative values are shaded.

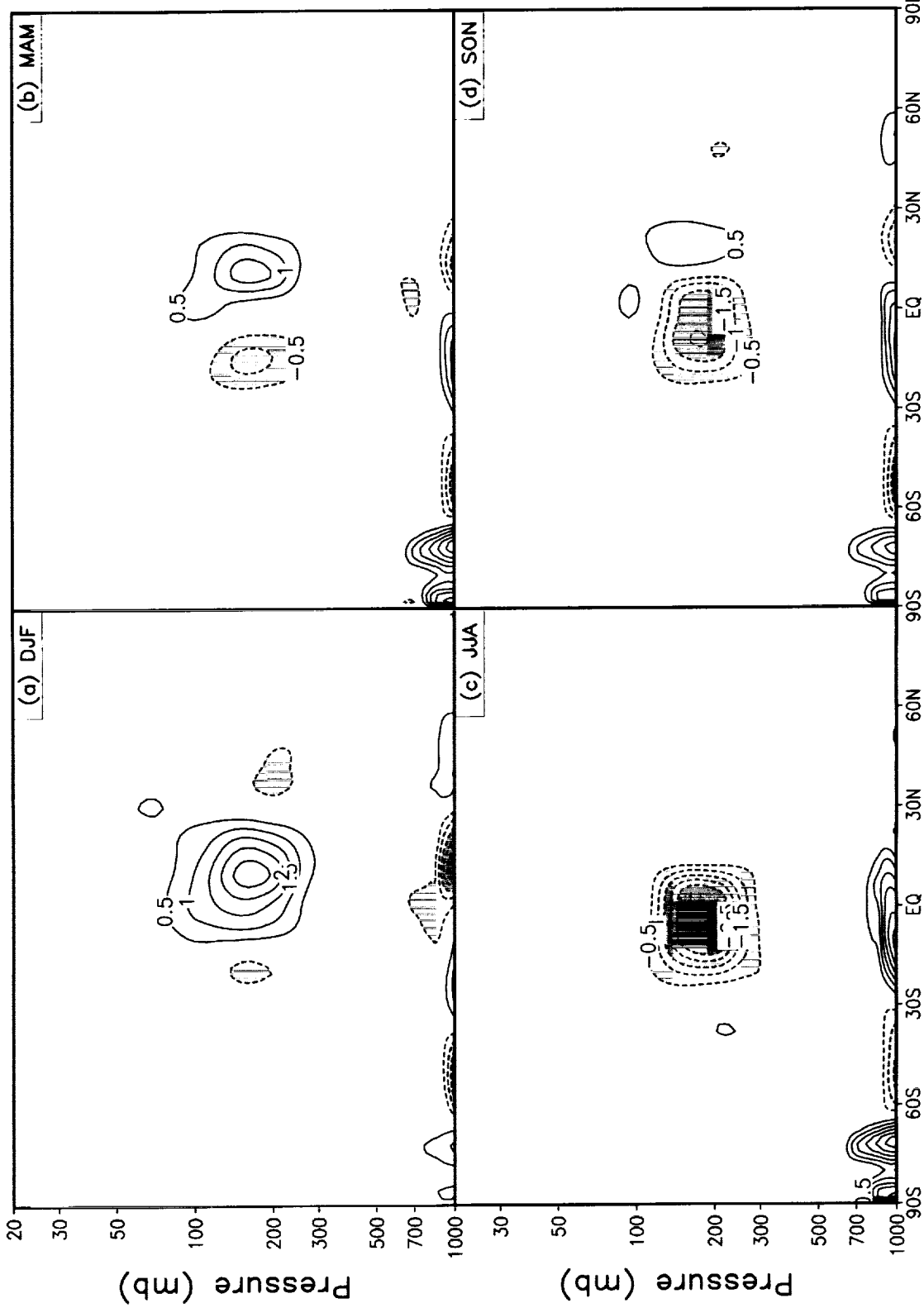

Figure 5: Seasonal means of zonally averaged v-wind for the reanalysis. The contour interval is 0.5 m s^{-1}. Negative values are shaded.

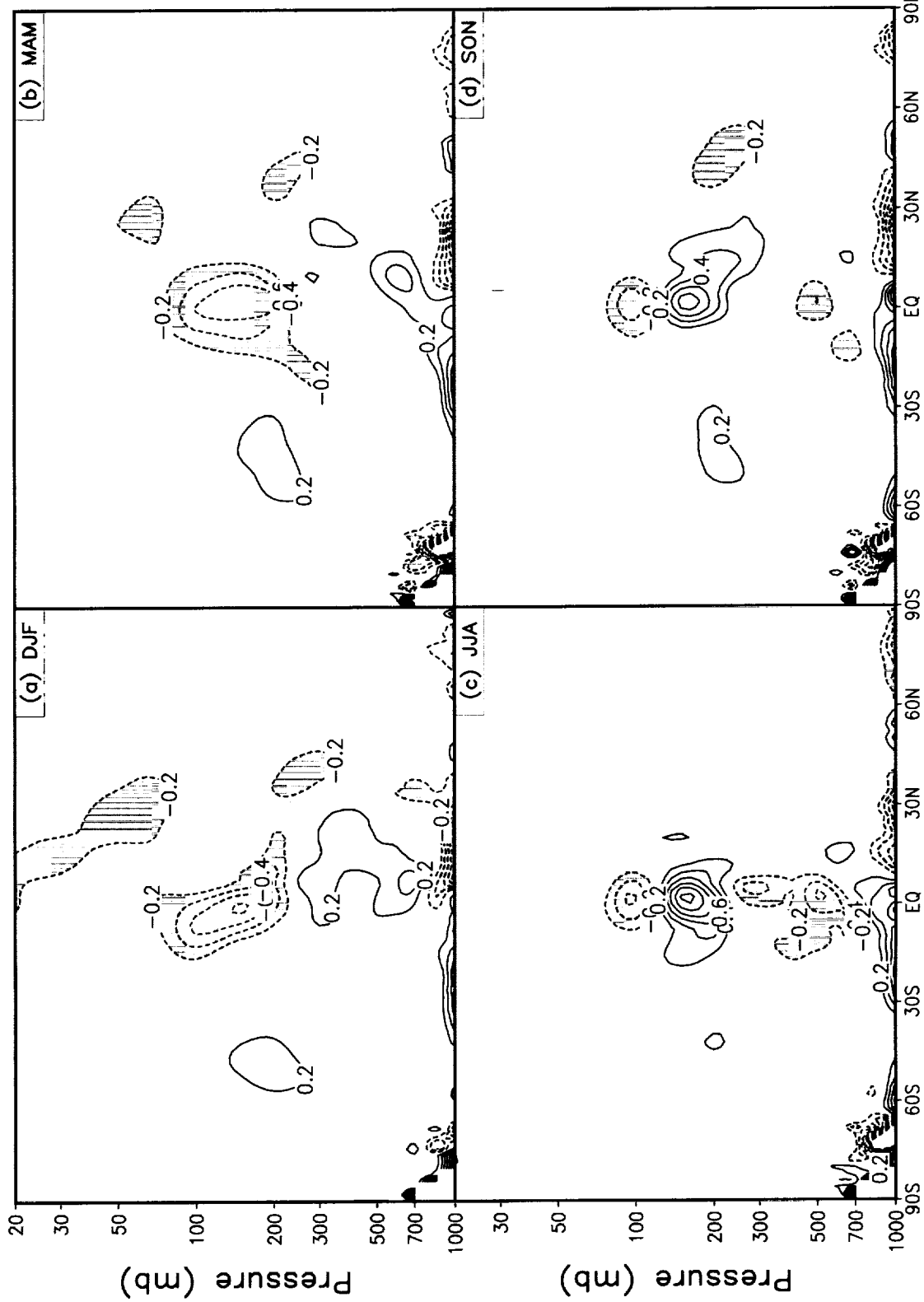

Figure 6: Seasonal means of zonally averaged v-wind difference between the model and the reanalysis. The contour interval is 0.2 m s^{-1}. Negative values are shaded.

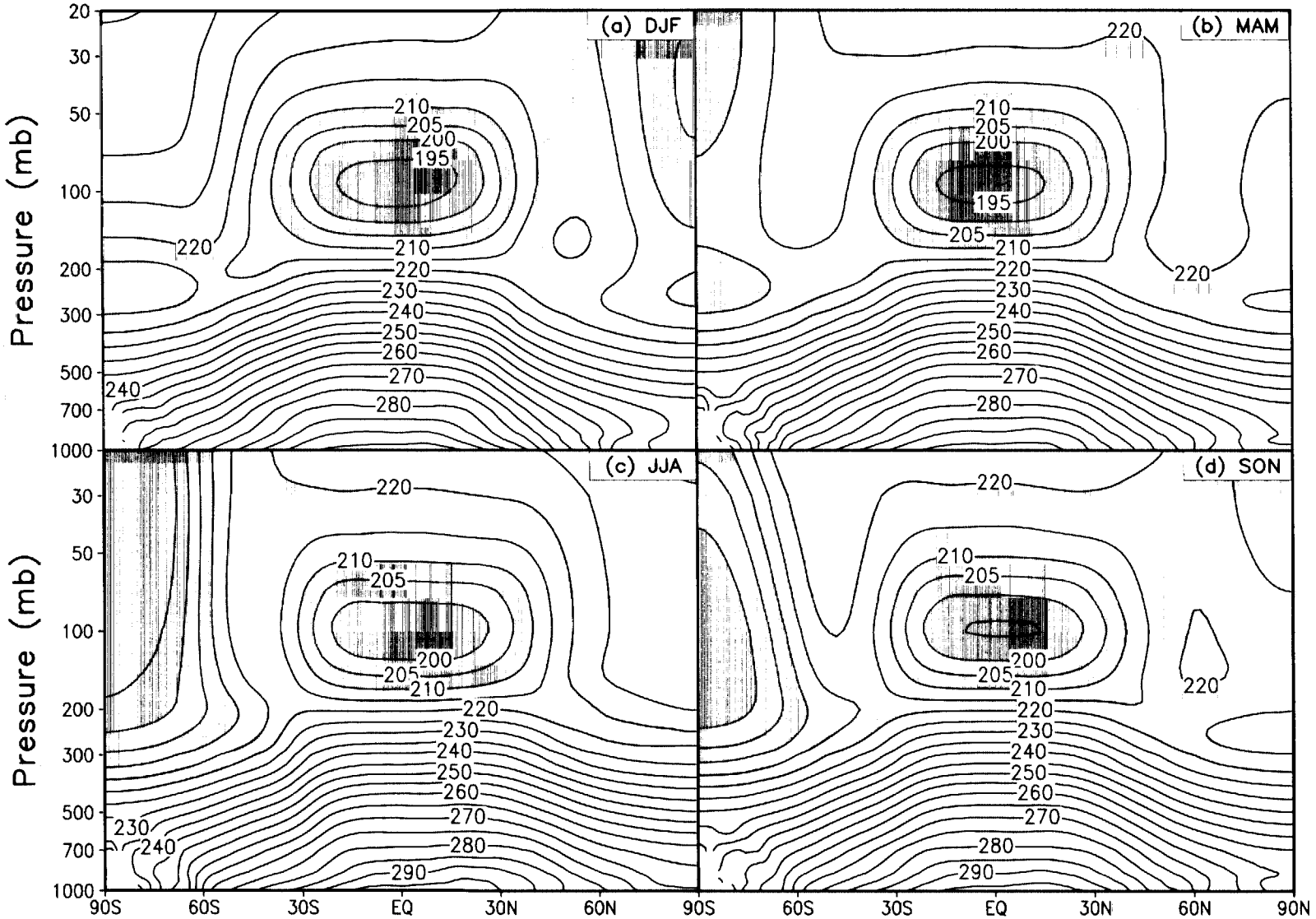

Figure 7: Seasonal means of zonally averaged temperature for the model. The contour interval is 5°K. Values less than 220°K are shaded.

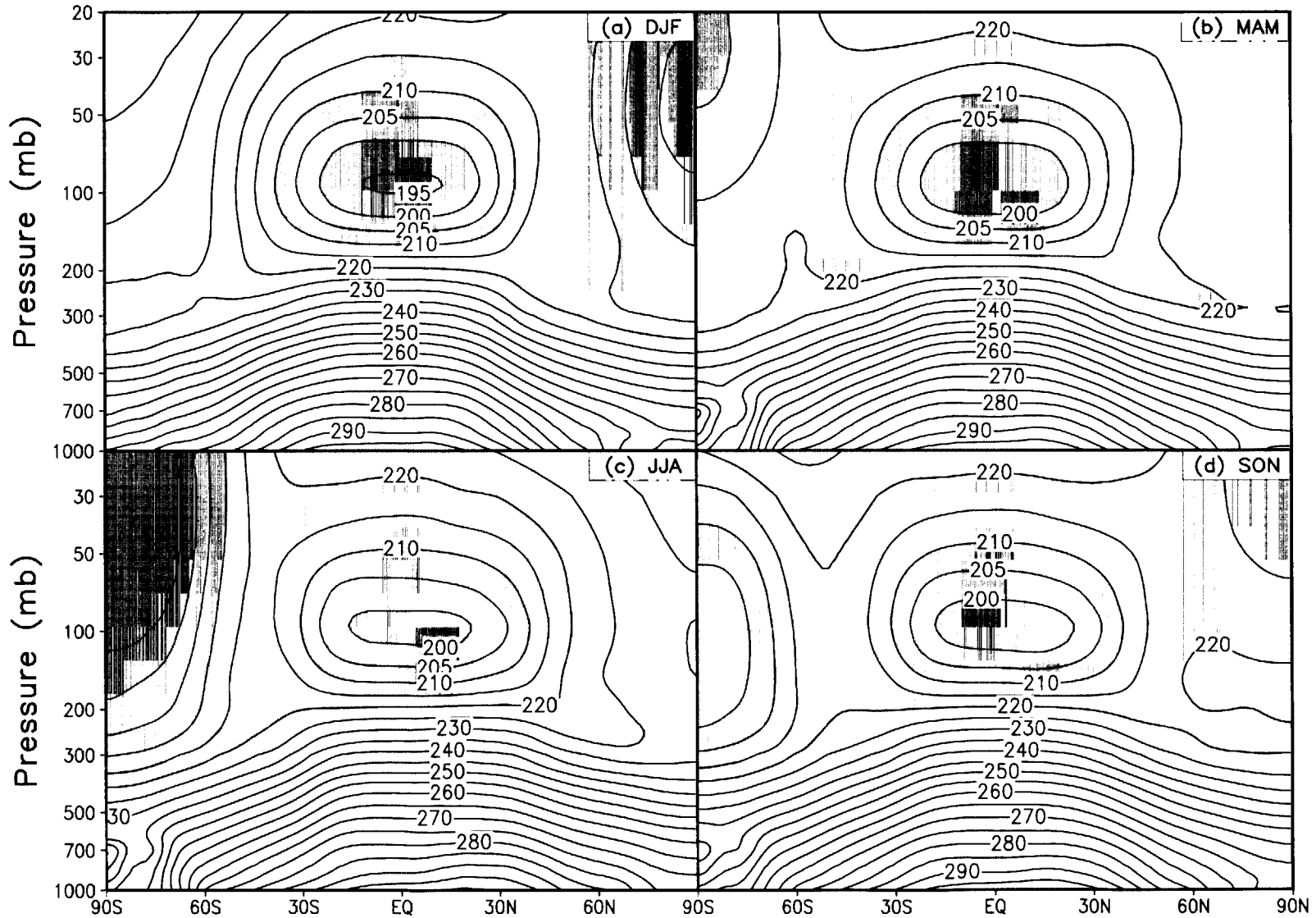

Figure 8: Seasonal means of zonally averaged temperature for the reanalysis. The contour interval is 5°K. Values less than 220°K are shaded.

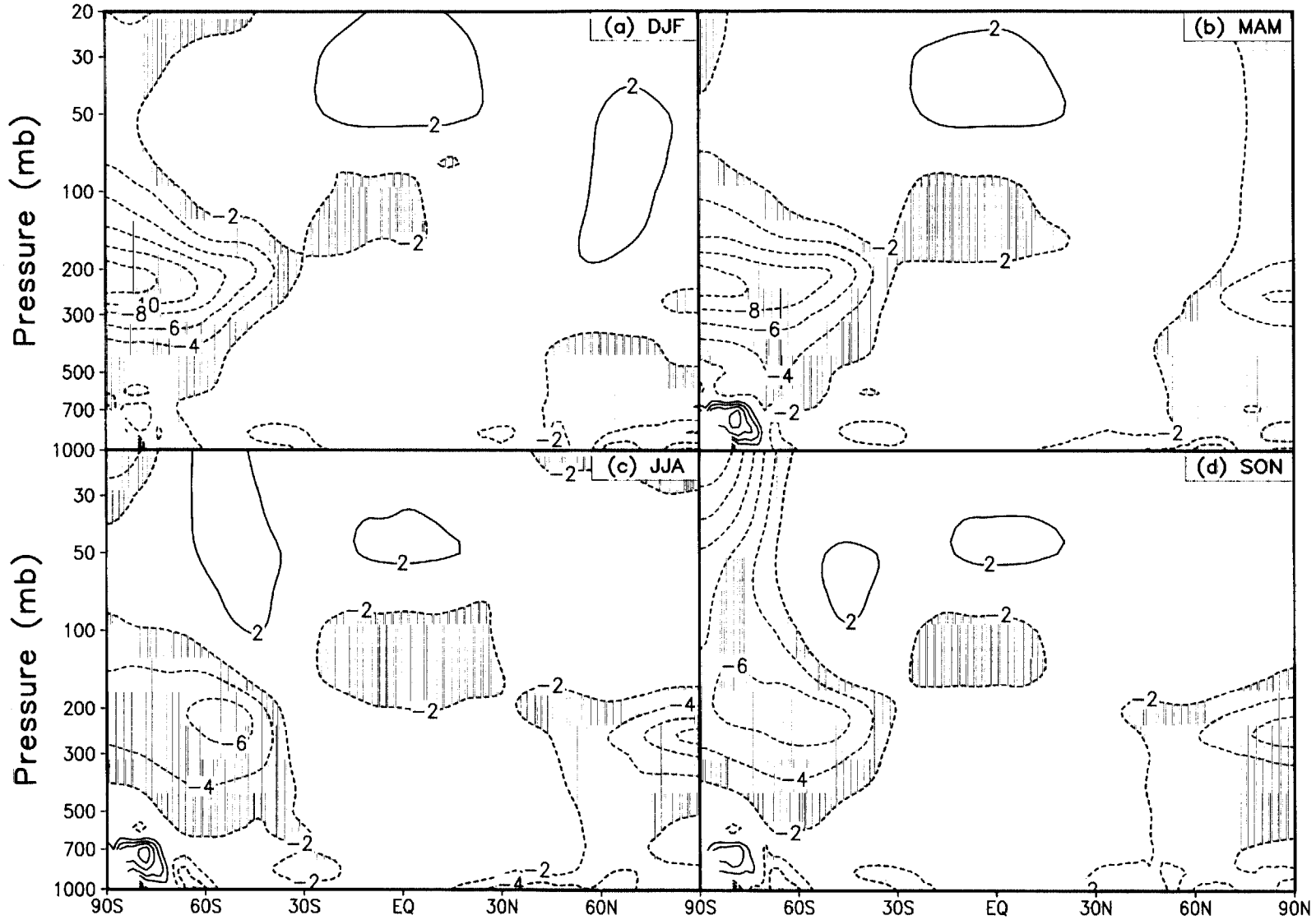

Figure 9: Seasonal means of zonally averaged temperature difference between the model and the reanalysis. The contour interval is 2°K. Negative values are shaded.

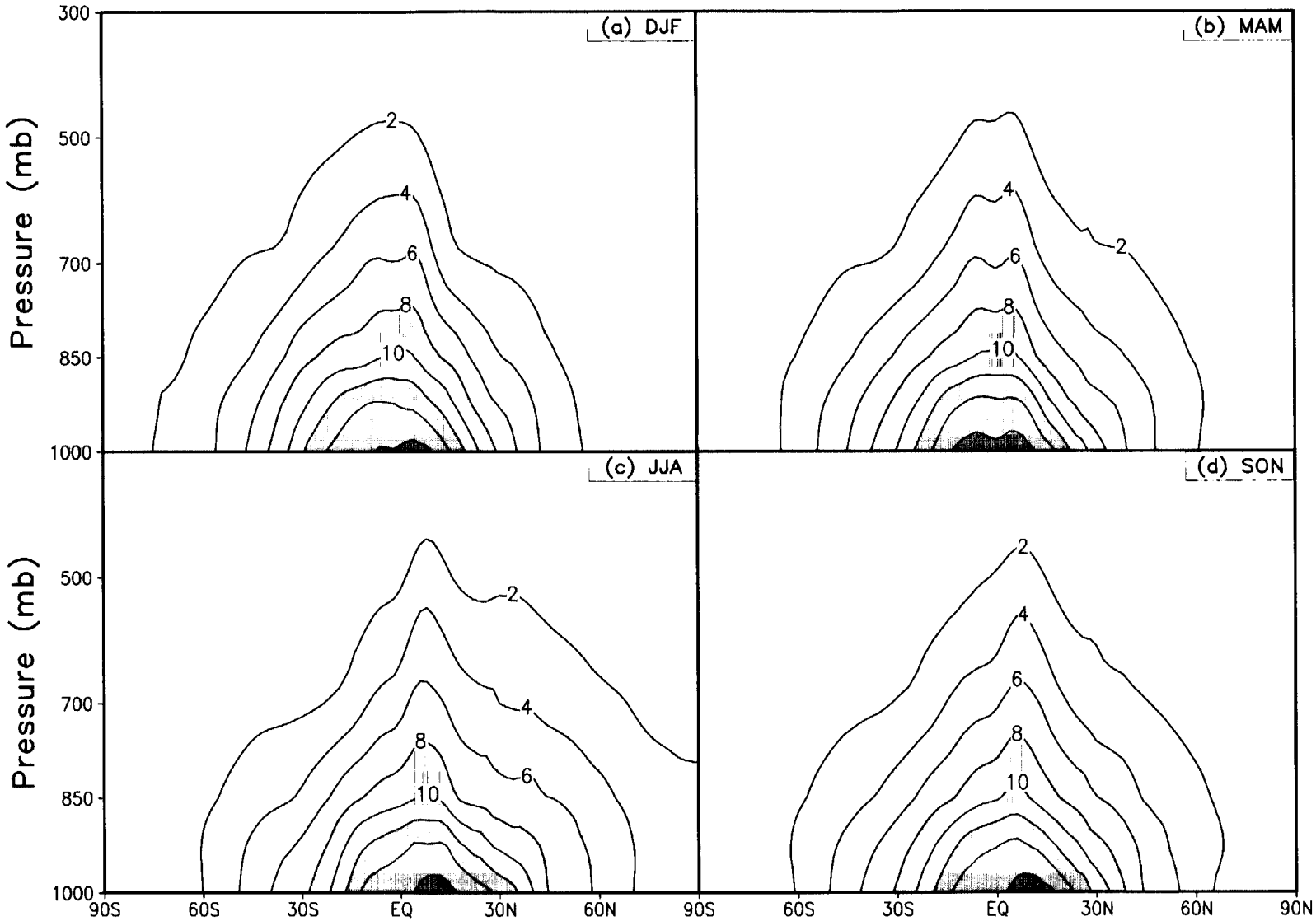

Figure 10: Seasonal means of zonally averaged specific humidity for the model. The contour interval is 2 g kg^{-1}. Values larger than 8 g kg^{-1} are shaded.

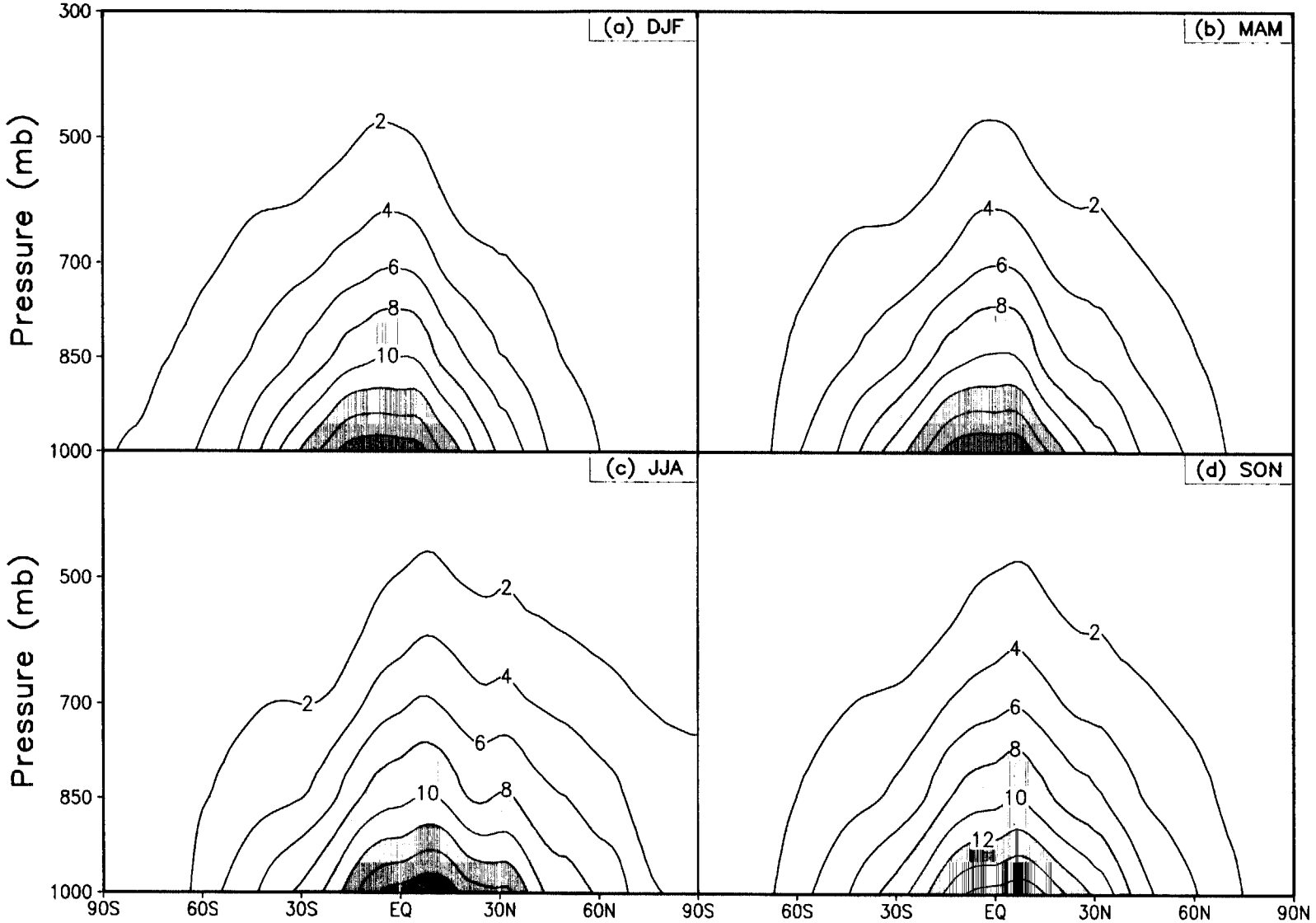

Figure 11: Seasonal means of zonally averaged specific humidity for the reanalysis. The contour interval is 2 g kg^{-1}. Values larger than 8 g kg^{-1} are shaded.

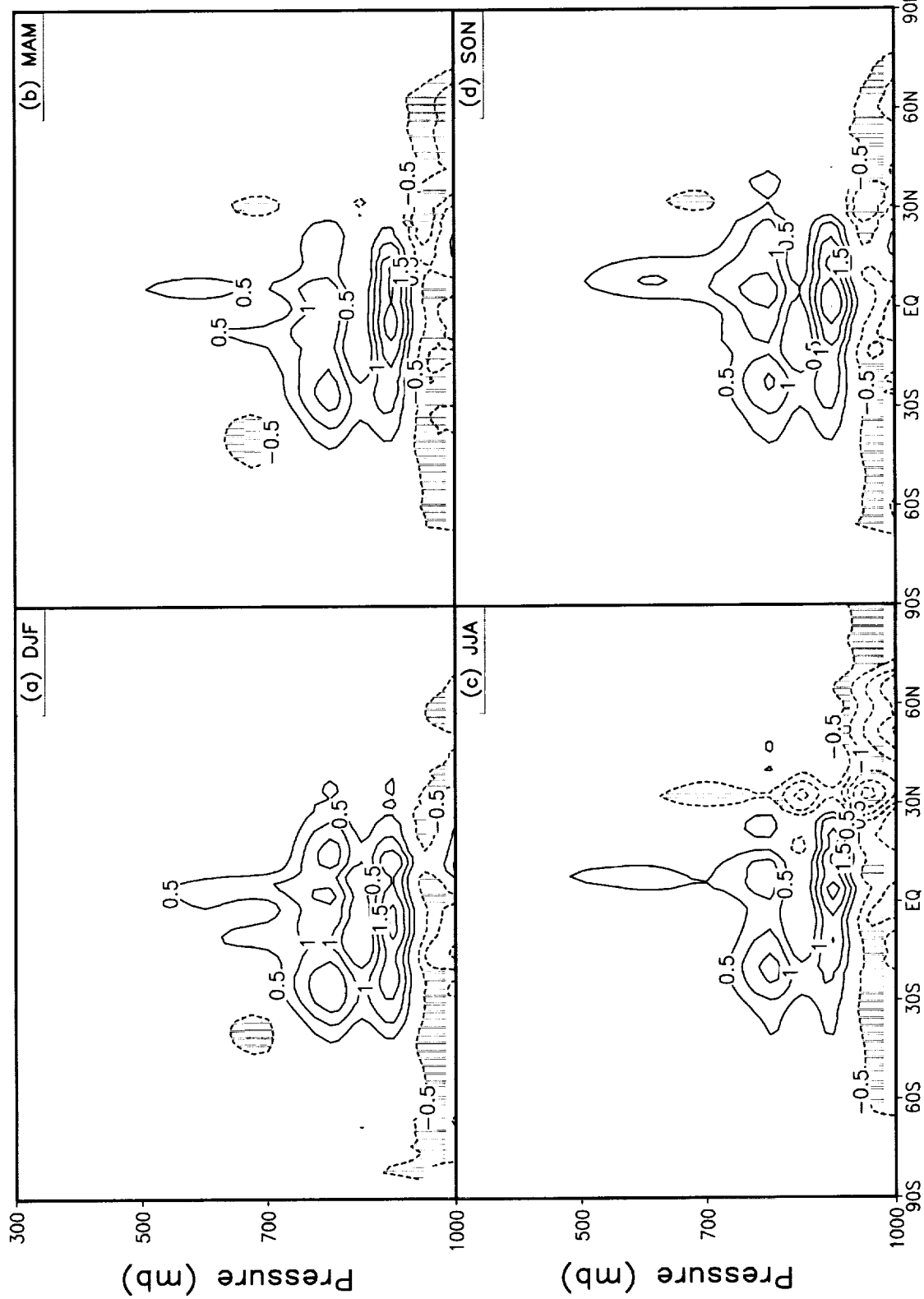

Figure 12: Seasonal means of zonally averaged specific humidity difference between the model and the reanalysis. The contour interval is 0.5 g kg^{-1}. Negative values are shaded.

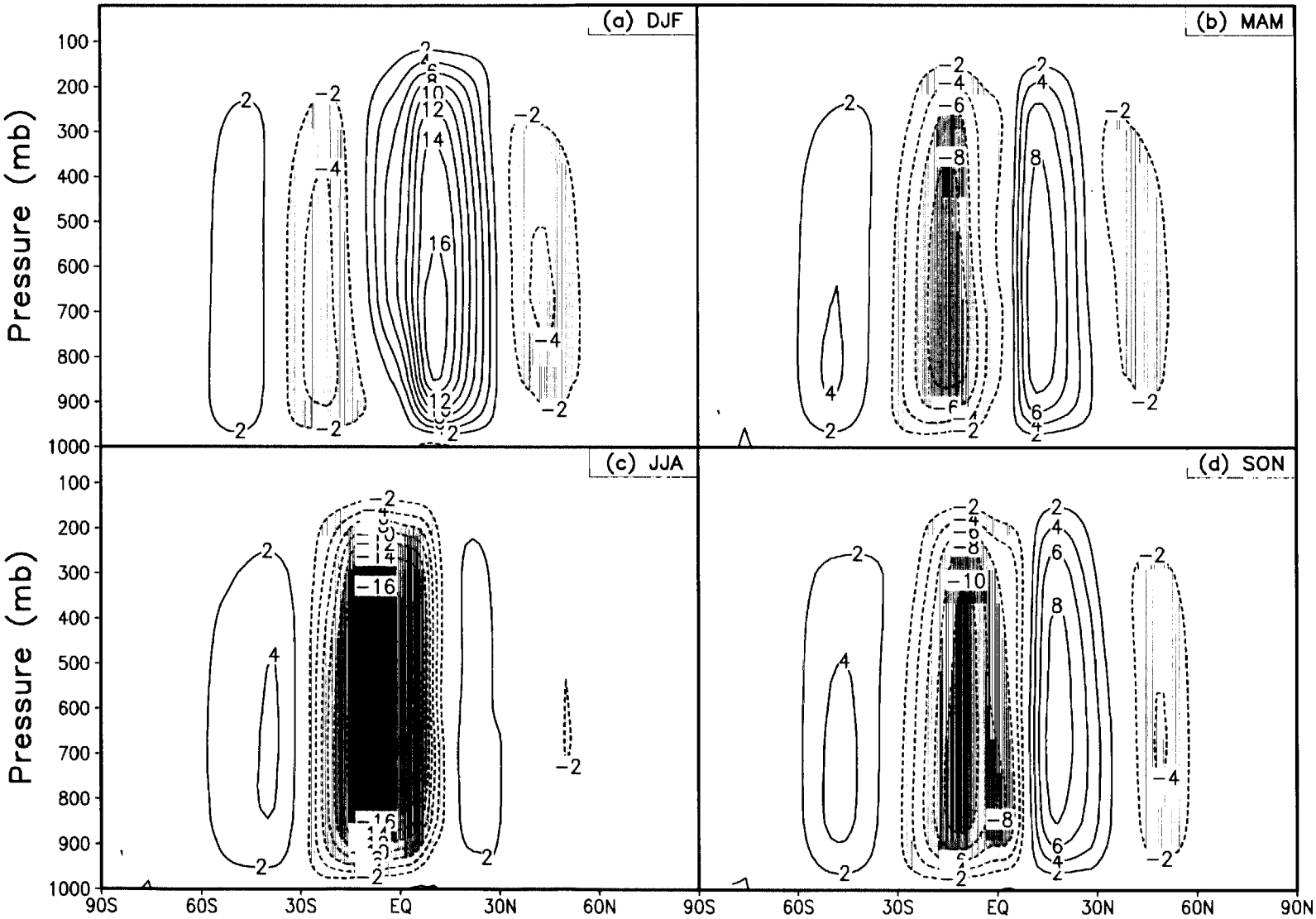

Figure 13: Seasonal means of zonally averaged mass stream function for the model. The contour interval is 2×10^{10} kg s^{-1}. Negative values are shaded.

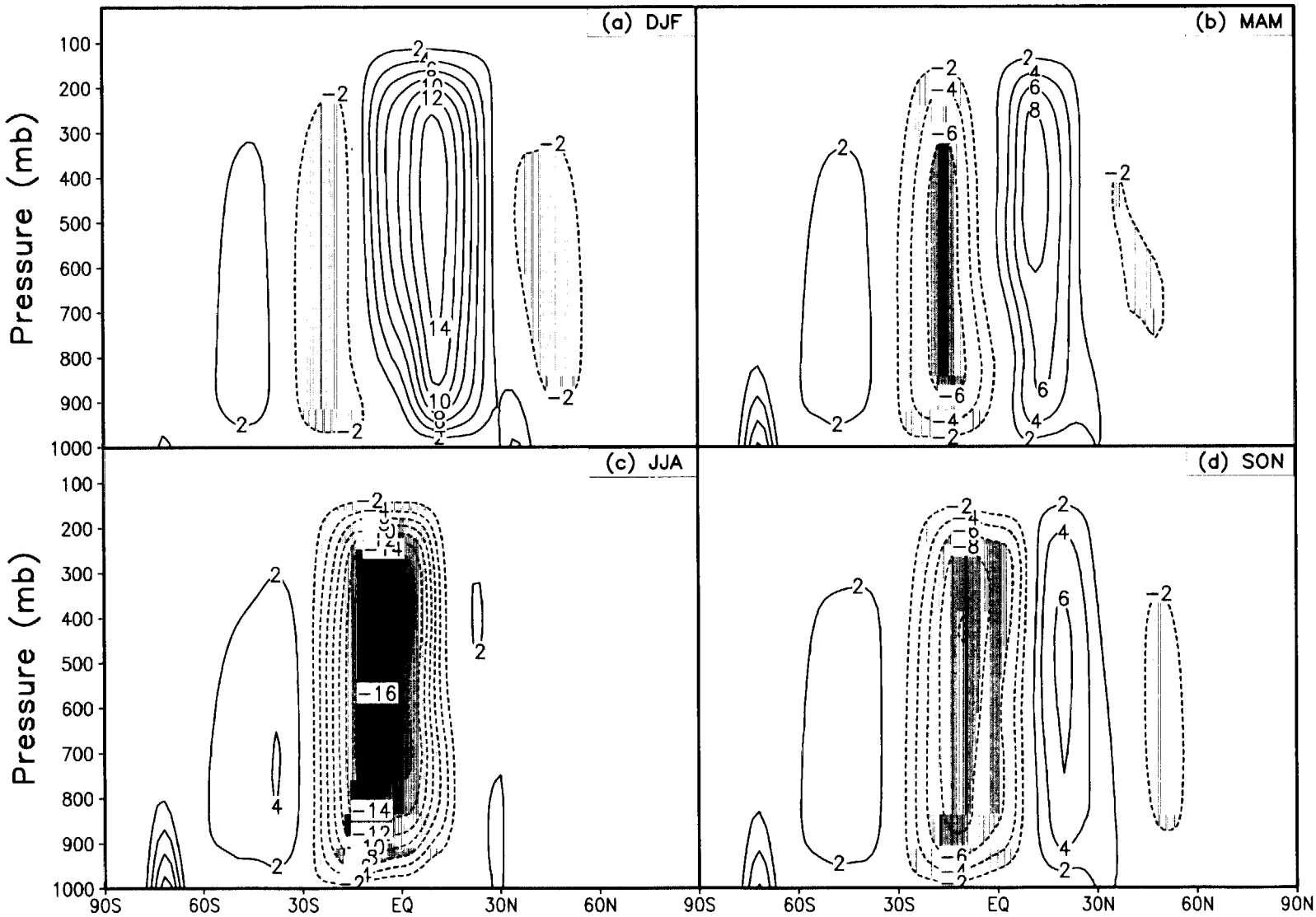

Figure 14: Seasonal means of zonally averaged mass stream function for the reanalysis. The contour interval is 2×10^{10} kg s^{-1}. Negative values are shaded.

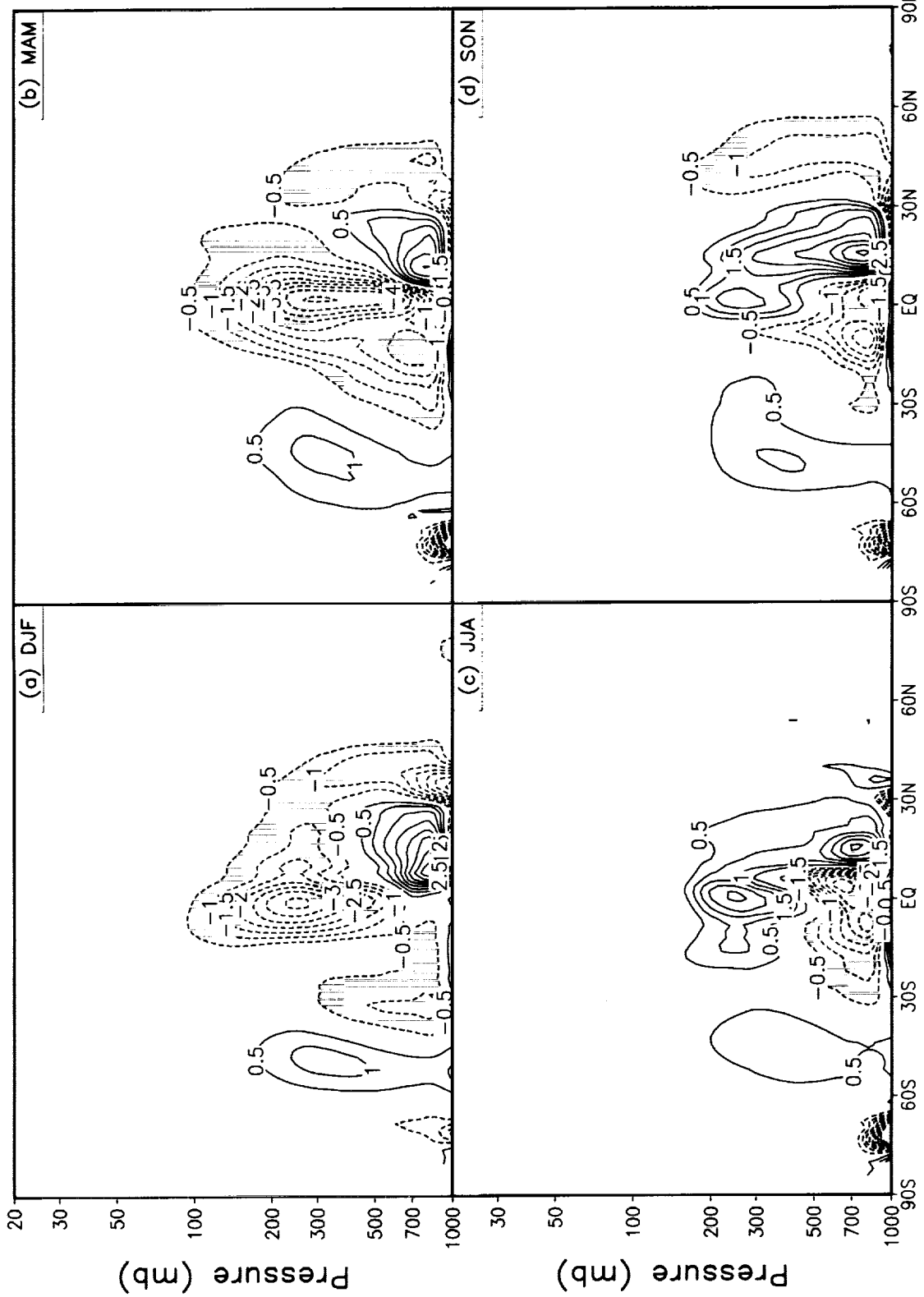

Figure 15: Seasonal means of zonally averaged mass stream function difference between the model and the reanalysis. The contour interval is 0.5×10^{10} kg s^{-1}. Negative values are shaded.

SEASONAL MEAN GLOBAL MAPS

50mb zonal wind

200mb zonal wind

850mb zonal wind

300mb eddy height

200mb eddy stream function

200mb velocity potential

Sea level pressure

Precipitation

Shortwave cloud forcing

Longwave cloud forcing

Total precipitable water

Outgoing longwave radiation

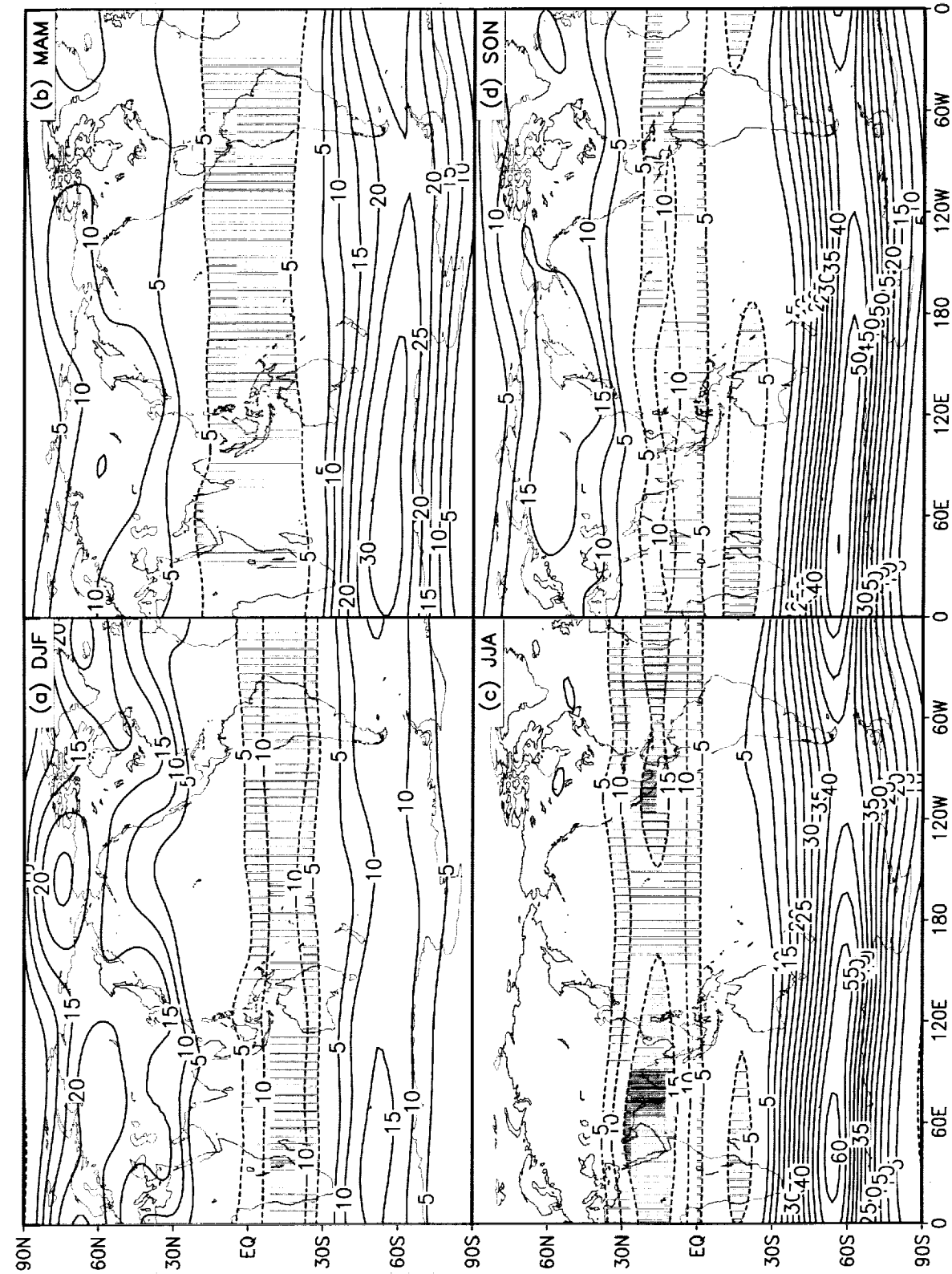

Figure 16: Seasonal means of 50 mb u-wind for the model. The contour interval is 5 m s^{-1}. Negative values are shaded.

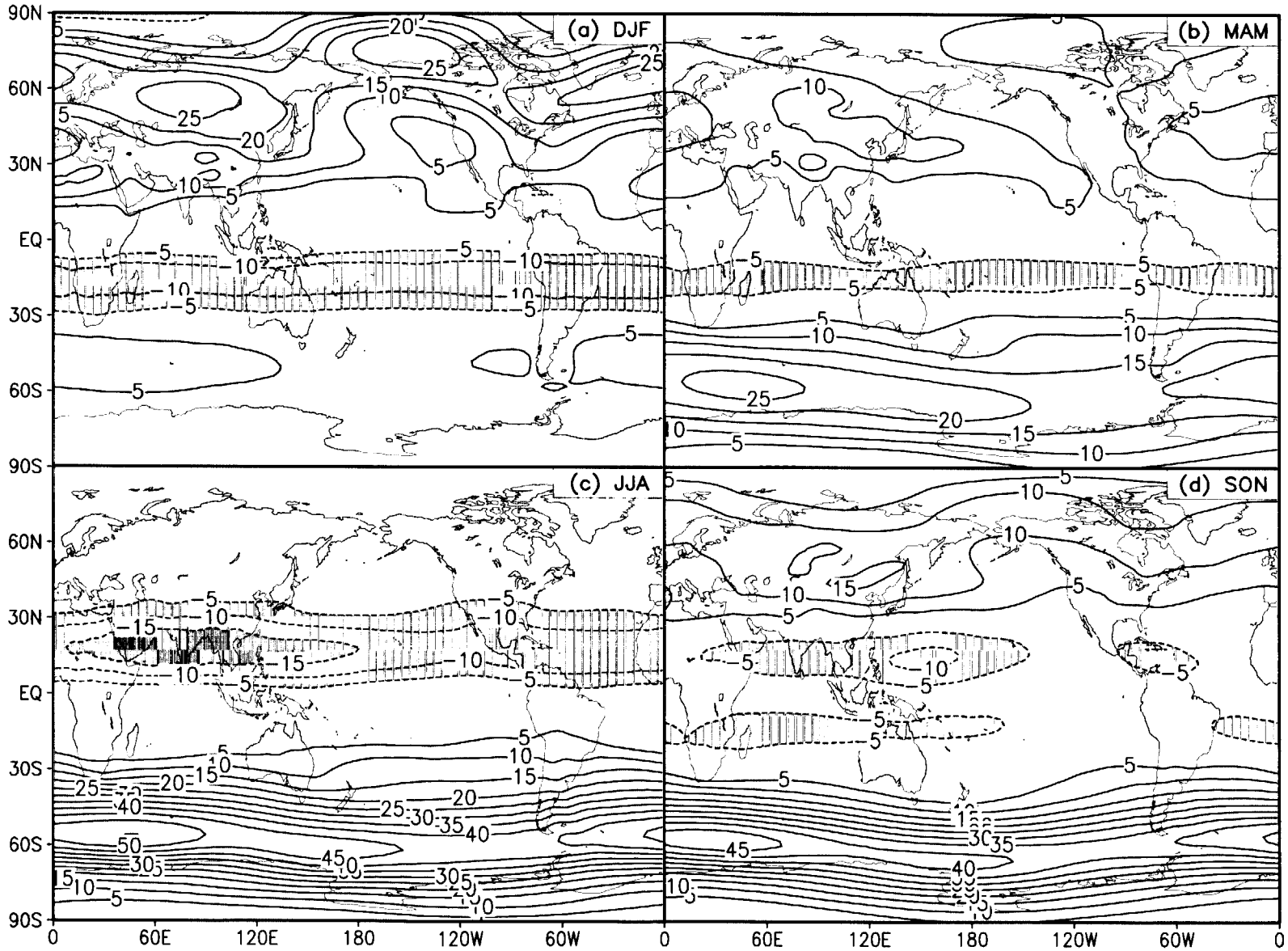

Figure 17: Seasonal means of 50 mb u-wind for the reanalysis. The contour interval is 5 m s^{-1}. Negative values are shaded.

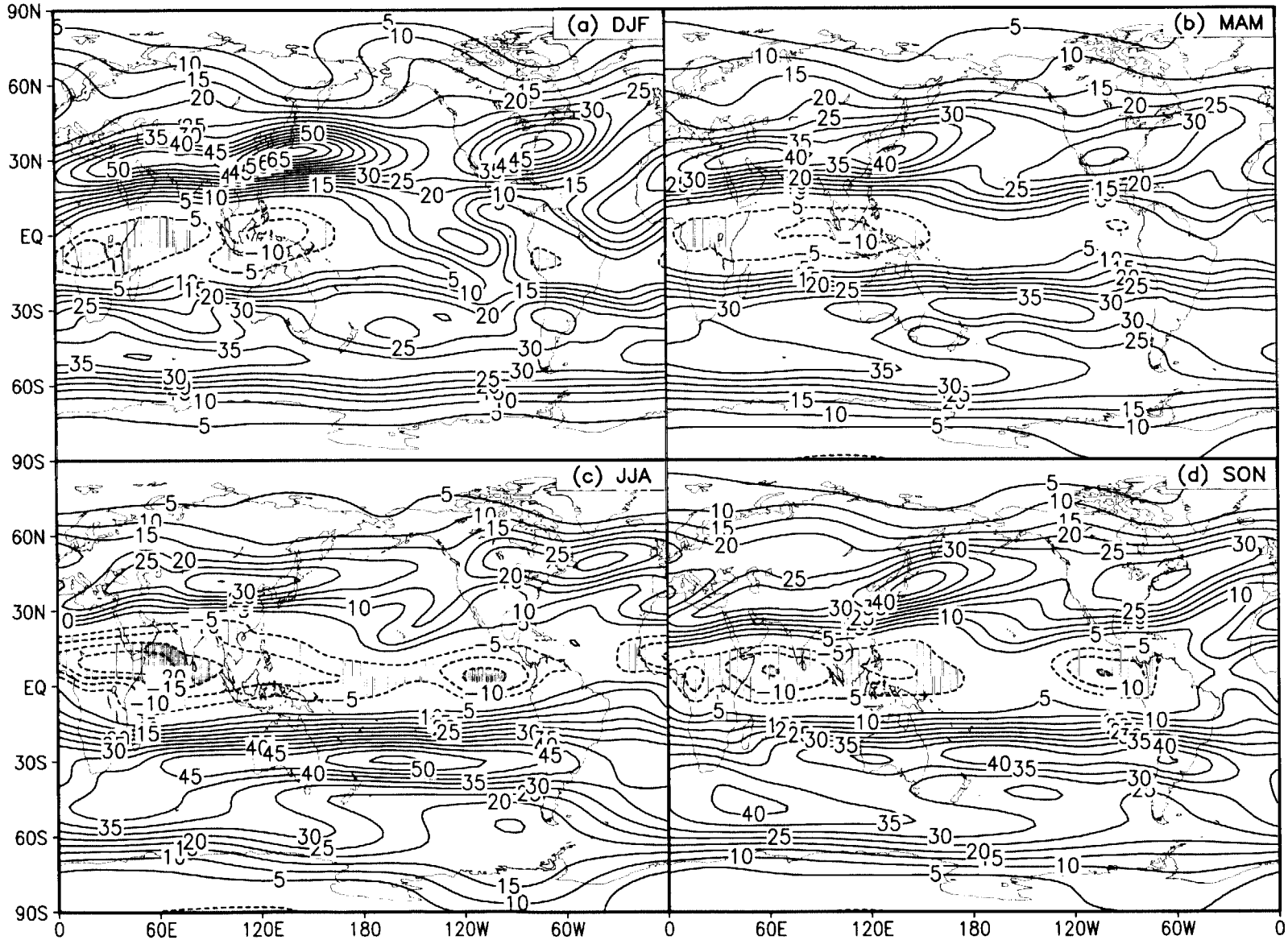

Figure 18: Seasonal means of 200 mb u-wind for the model. The contour interval is 5 m s^{-1}. Negative values are shaded.

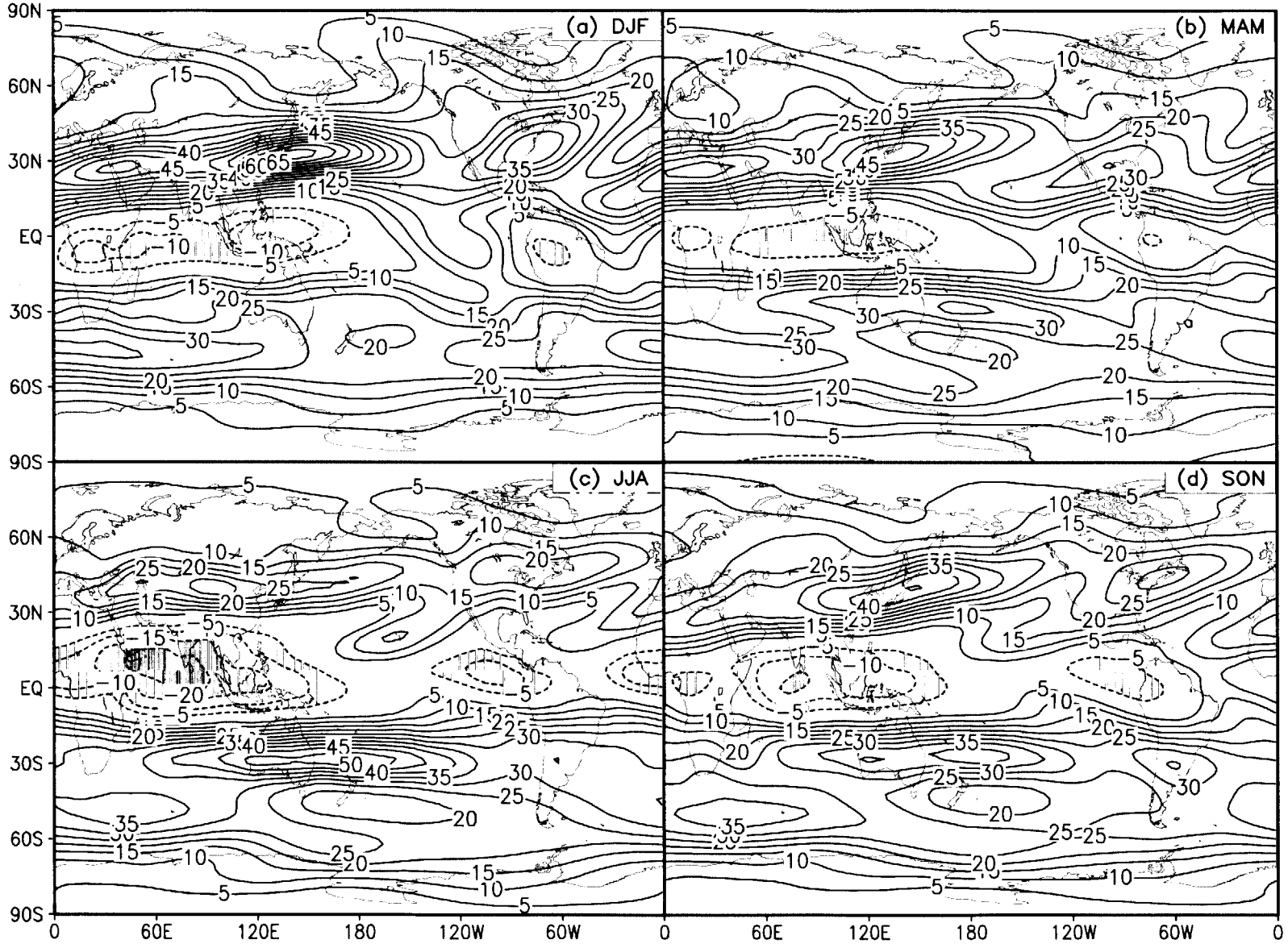

Figure 19: Seasonal means of 200 mb u-wind for the reanalysis. The contour interval is 5 m s^{-1}. Negative values are shaded.

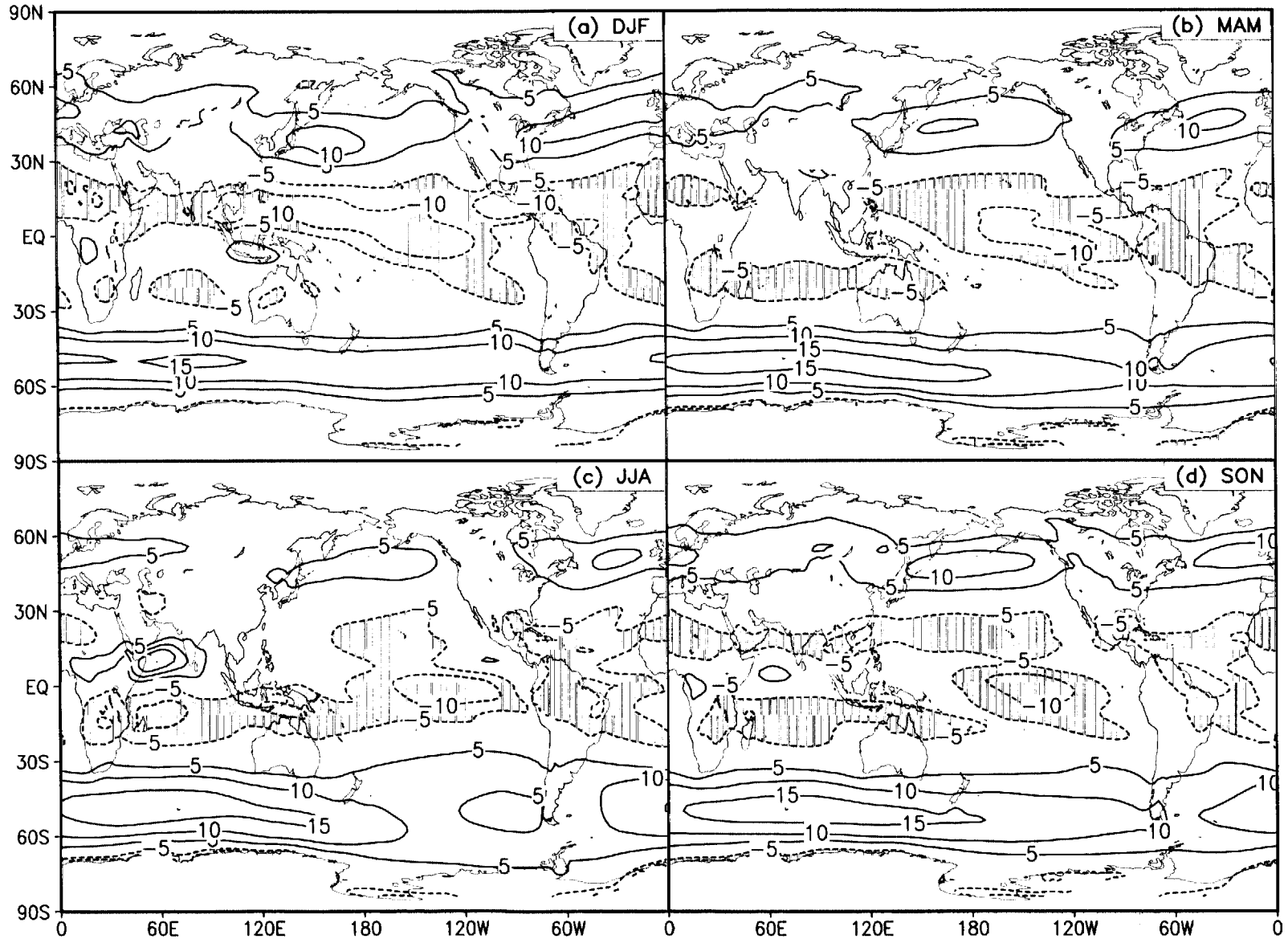

Figure 20: Seasonal means of 850 mb u-wind for the model. The contour interval is 5 m s^{-1}. Negative values are shaded.

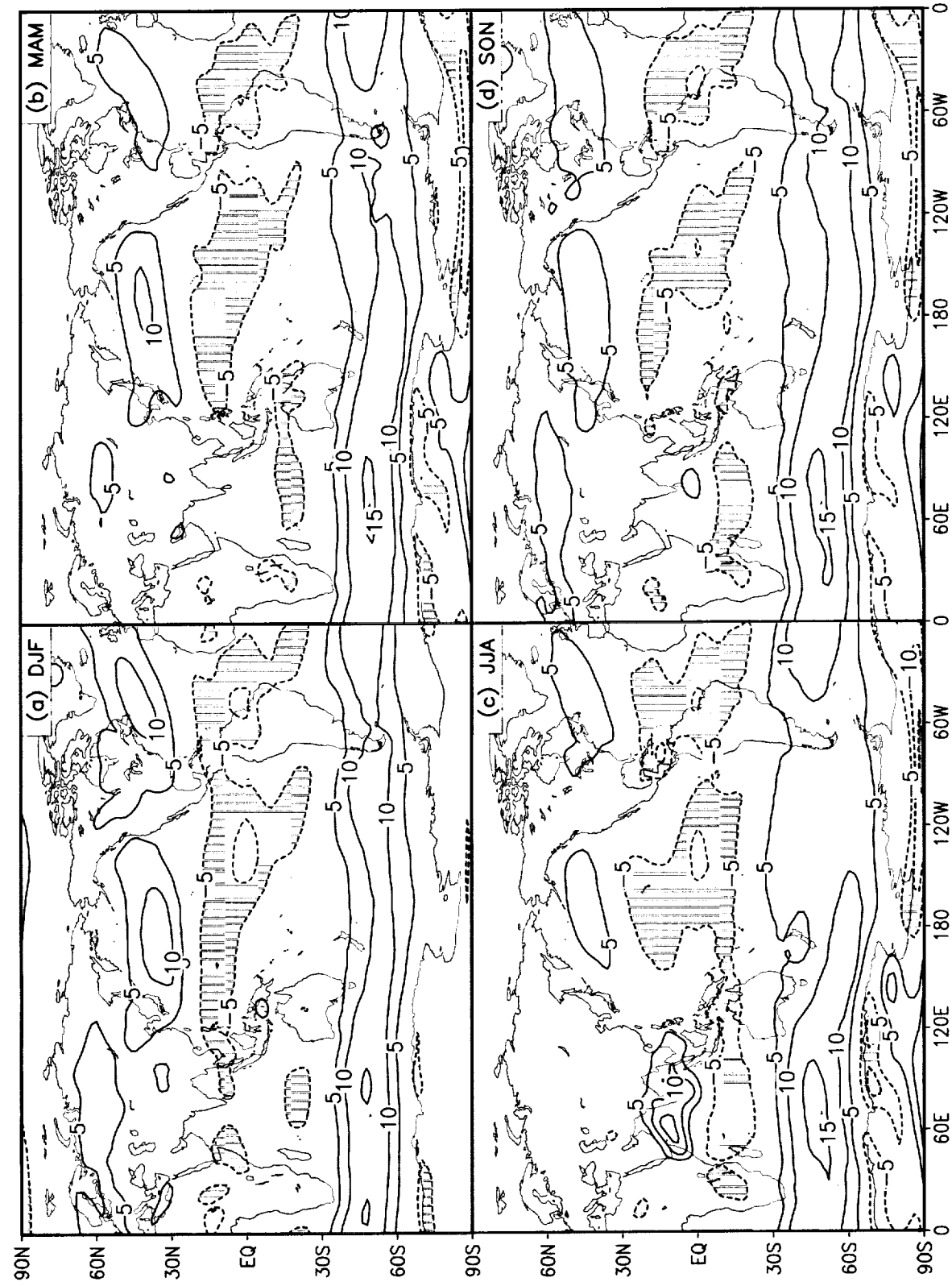

Figure 21: Seasonal means of 850 mb u-wind for the reanalysis. The contour interval is 5 m s^{-1}. Negative values are shaded.

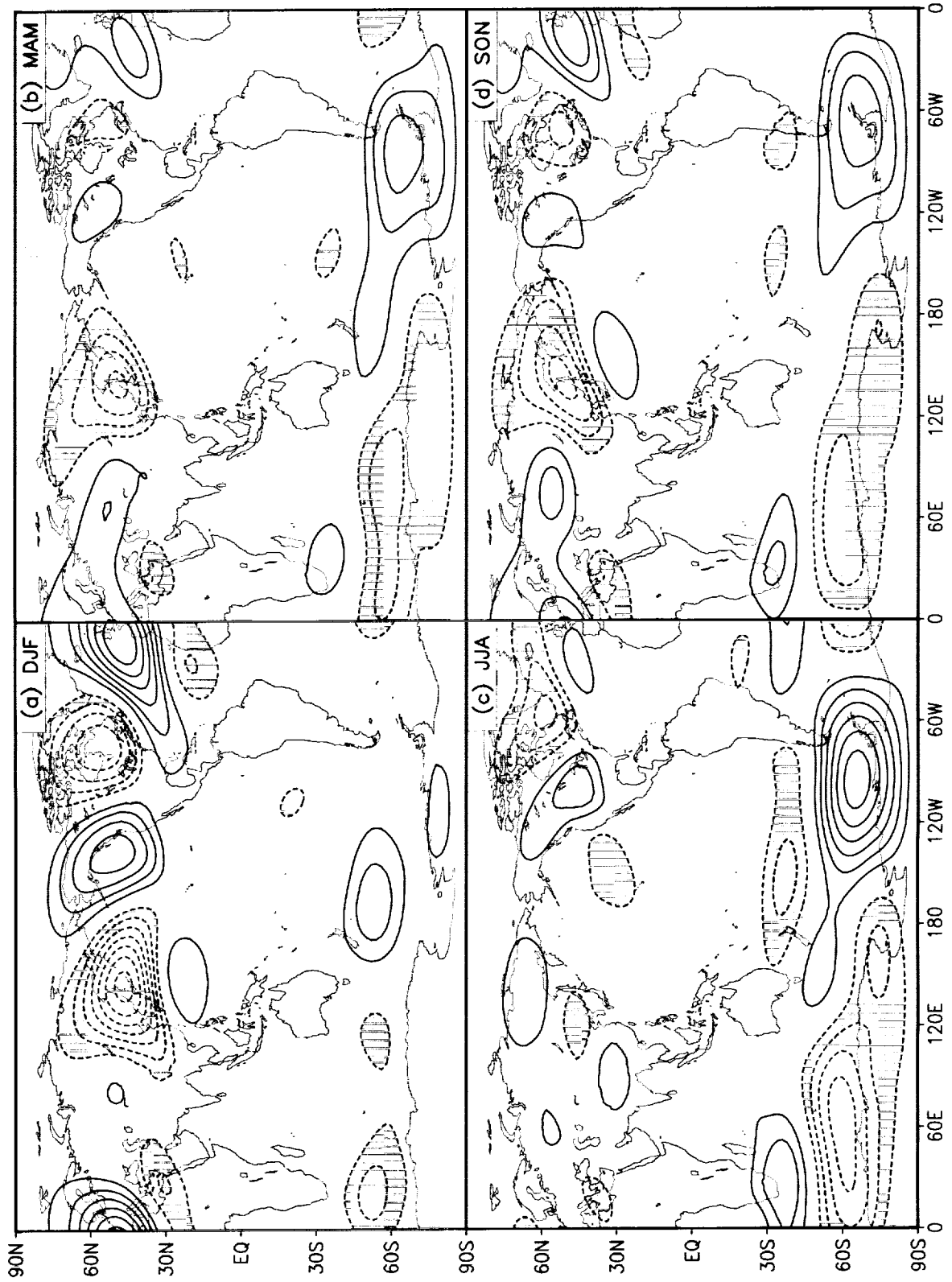

Figure 22: Seasonal means of 300 mb eddy height for the model. The contour interval is 40 m. The zero contour is omitted. Negative values are shaded.

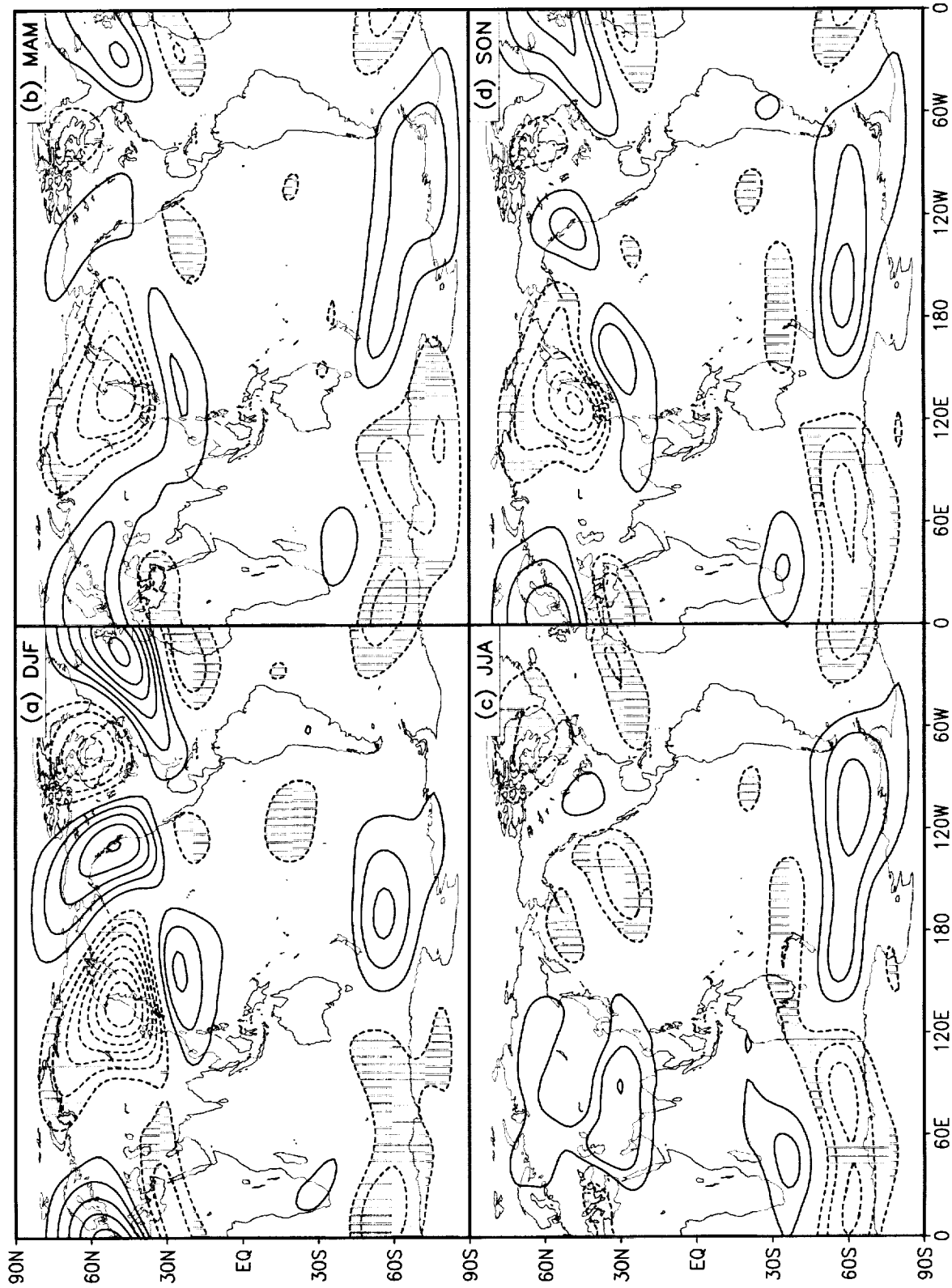

Figure 23: Seasonal means of 300 mb eddy height for the reanalysis. The contour interval is 40 m. The zero contour is omitted. Negative values are shaded.

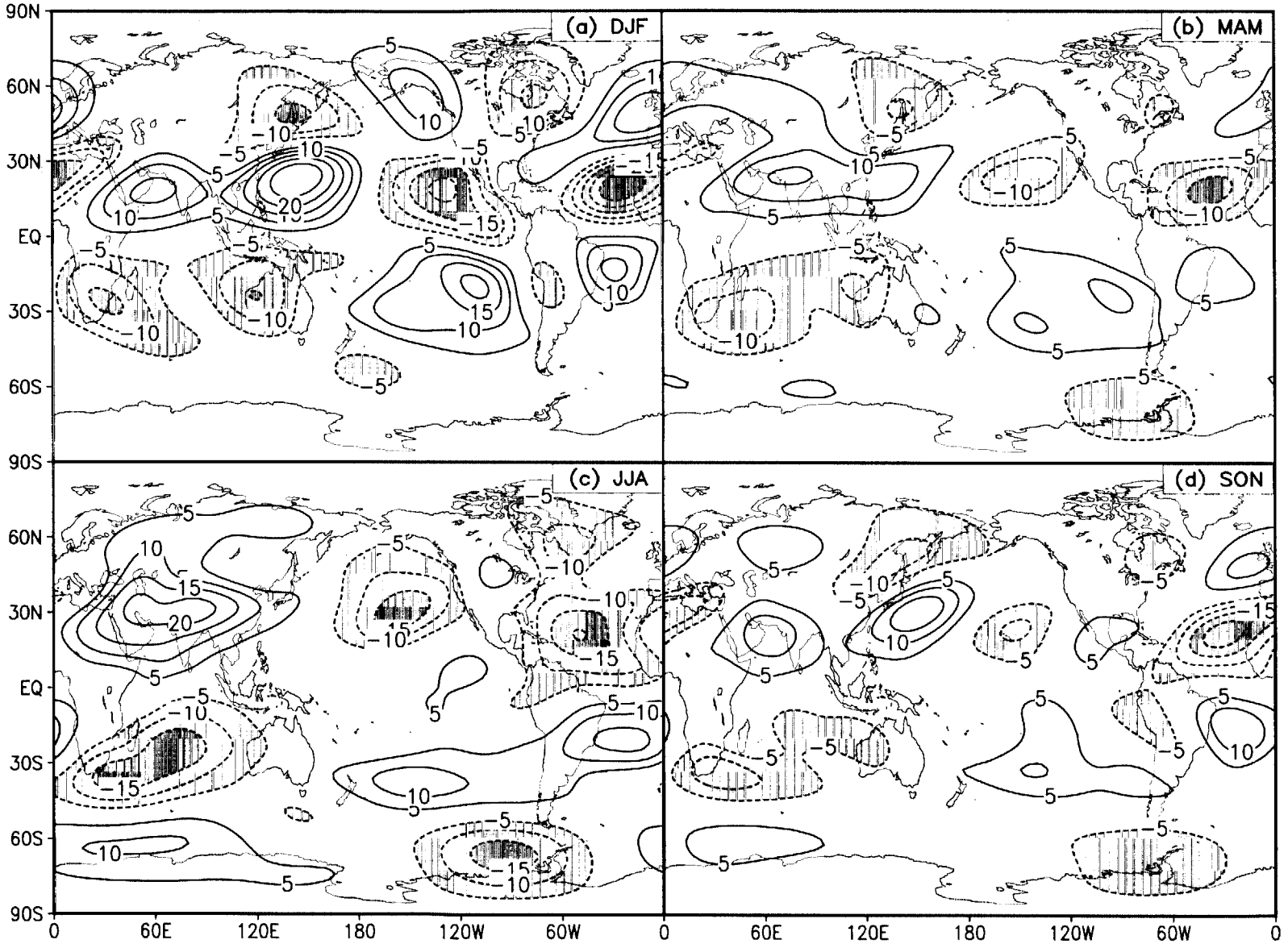

Figure 24: Seasonal means of 200 mb streamfunction for the model. The contour interval is 5×10^6 m^2 s^{-1}. Negative values are shaded.

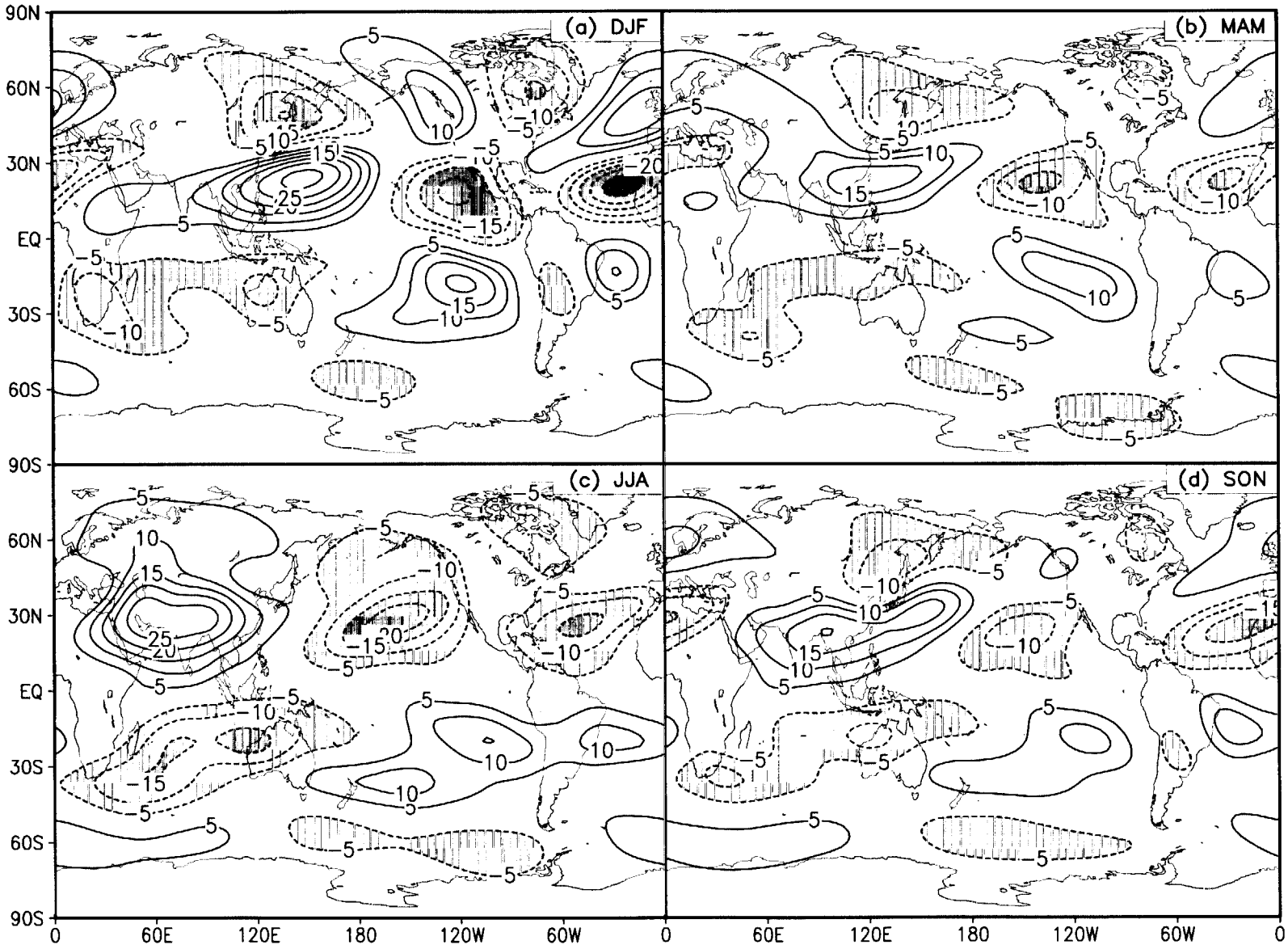

Figure 25: Seasonal means of 200 mb streamfuction for the reanalysis. The contour interval is 5×10^6 m^2 s^{-1}. Negative values are shaded.

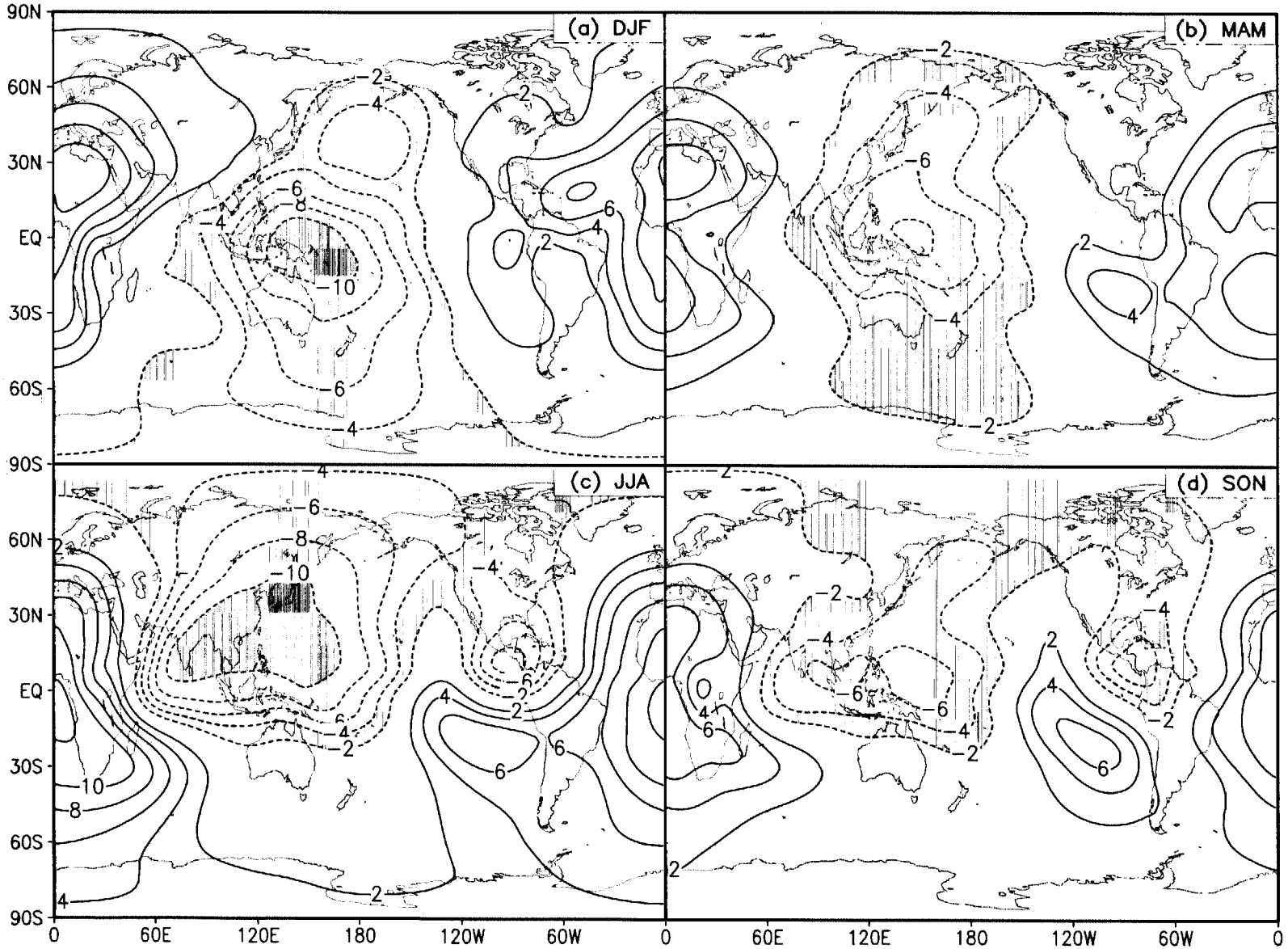

Figure 26: Seasonal means of 200 mb velocity potential for the model. The contour interval is 2×10^6 m^2 s^{-1}. Negative values are shaded.

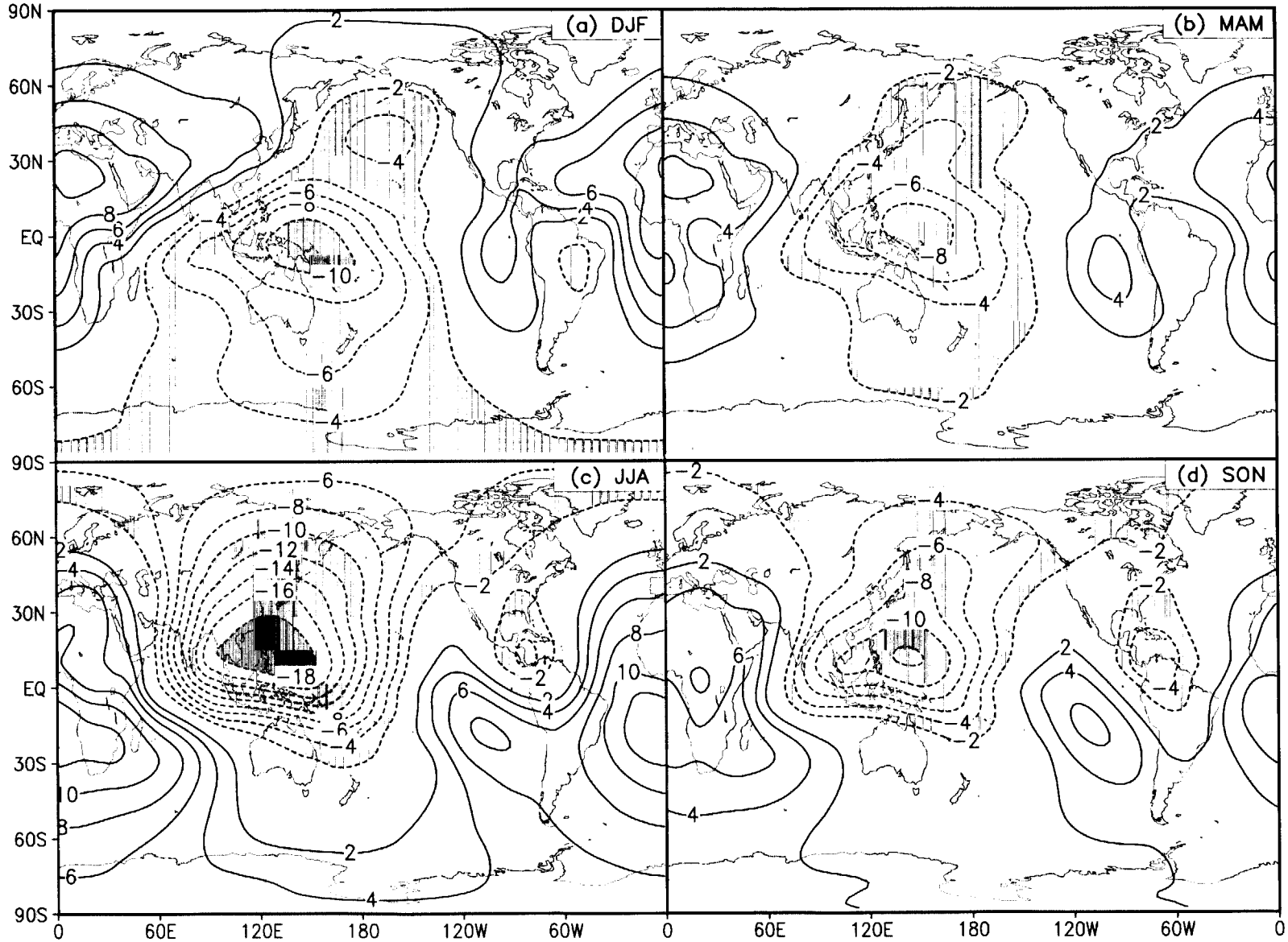

Figure 27: Seasonal means of 200 mb velocity potential for the reanalysis. The contour interval is 2×10^6 m^2 s^{-1}. Negative values are shaded.

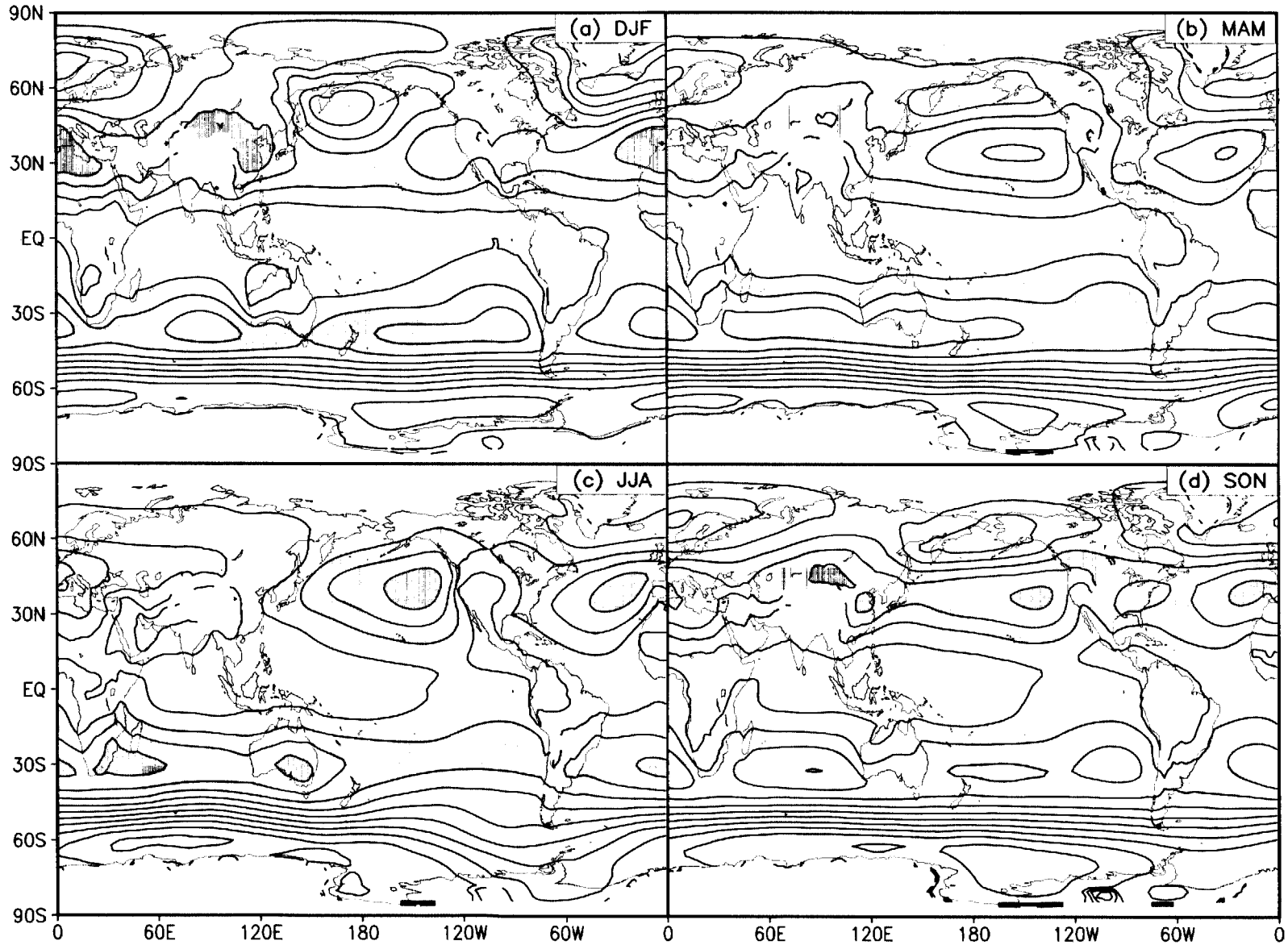

Figure 28: Seasonal means of sea level pressure for the model. The contour interval is 5 mb. Values larger than 1015 mb are shaded.

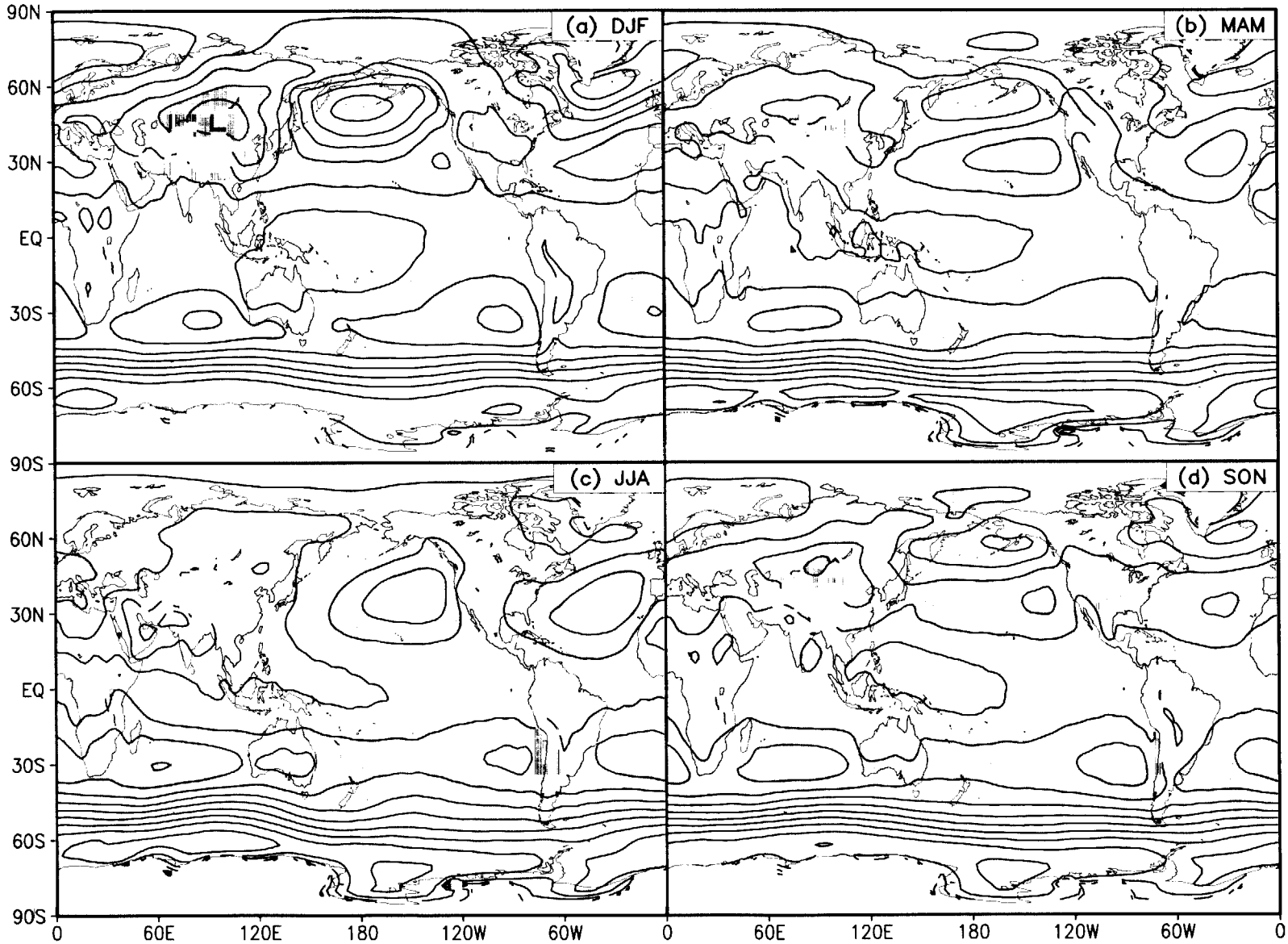

Figure 29: Seasonal means of sea level pressure for the reanalysis. The contour interval is 5 mb. Values larger than 1015 mb are shaded.

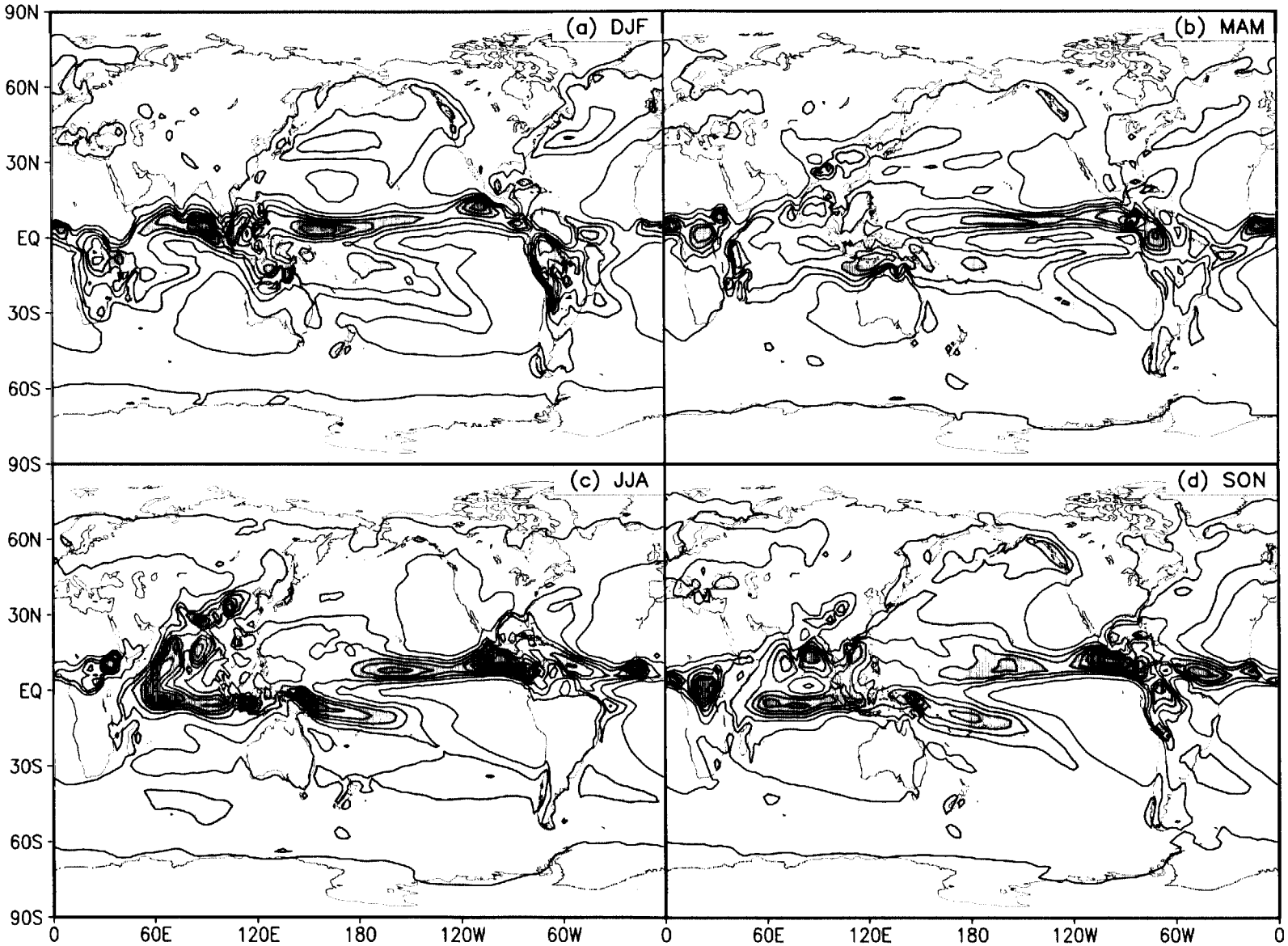

Figure 30: Seasonal means of precipitation for the model during 1980–1995. The contour interval is 2 mm day^{-1}. Values larger than 4 mm day^{-1} have light shading. Values larger than 8 mm day^{-1} have dark shading.

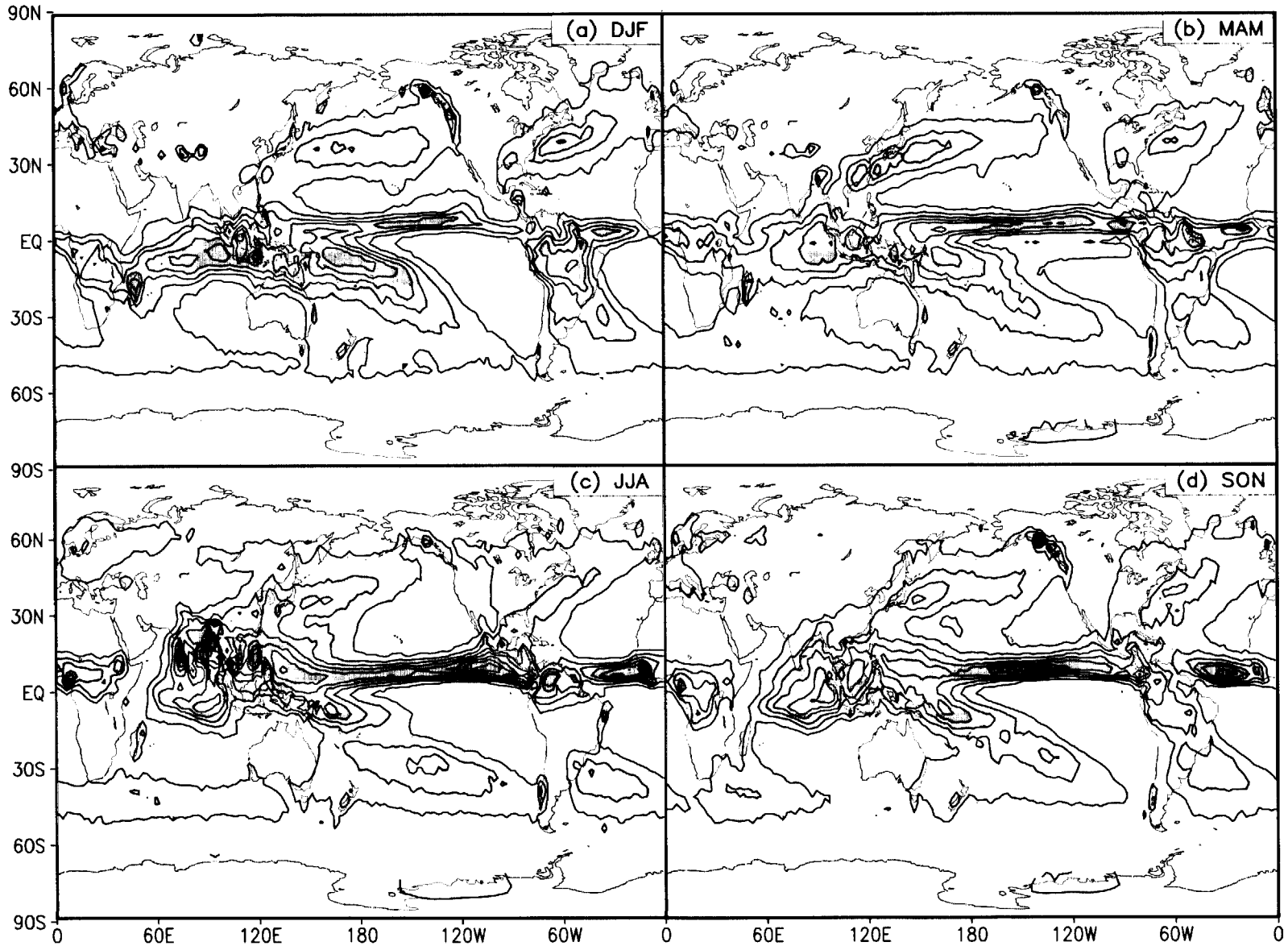

Figure 31: Seasonal means of precipitation for Xie-Arkin data during 1980–1995. The contour interval is 2 mm day^{-1}. Values larger than 4 mm day^{-1} have light shading. Values larger than 8 mm day^{-1} have dark shading.

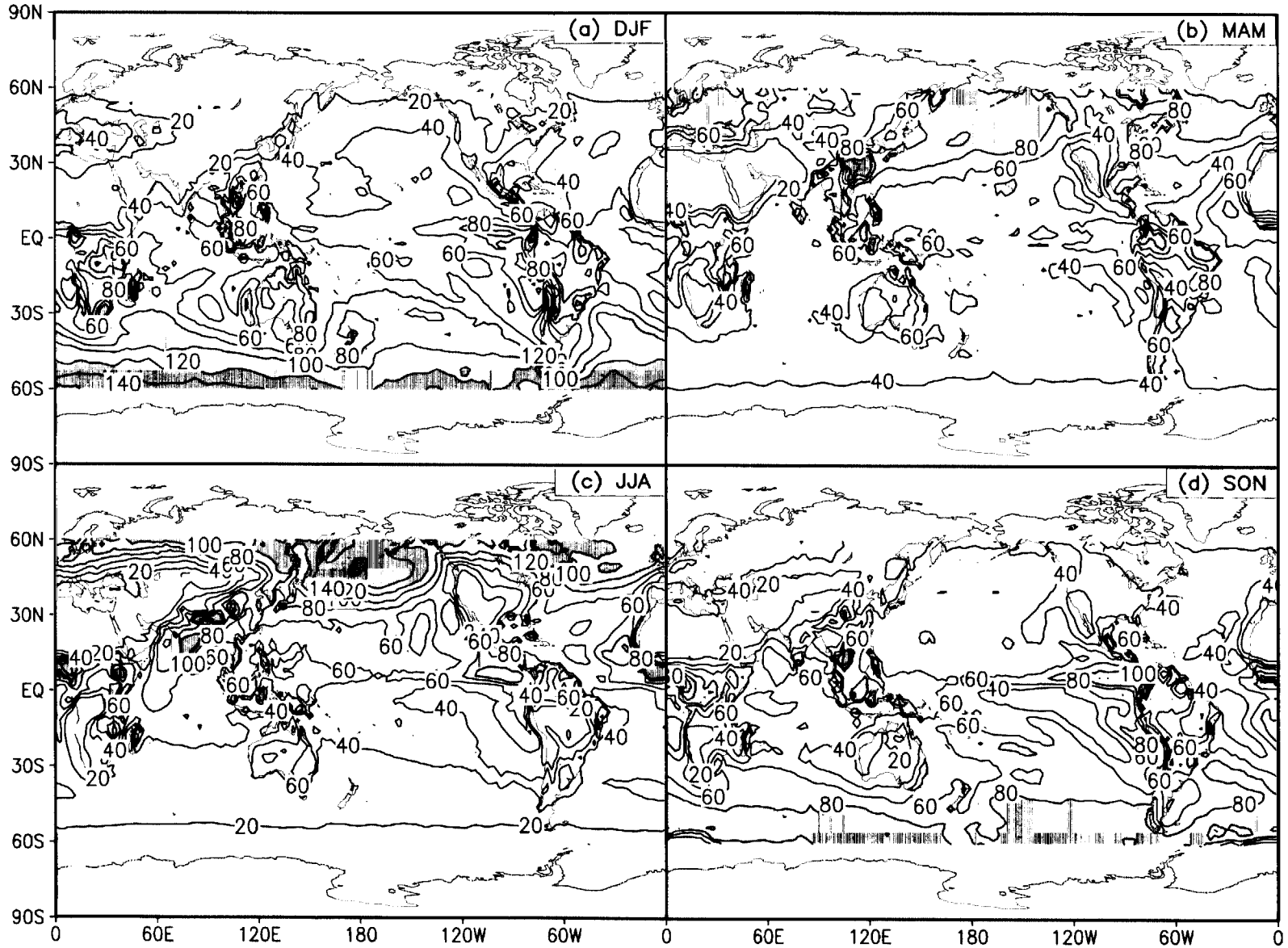

Figure 32: Seasonal means of shortwave cloud radiative forcing for the model during 1985–1991. The contour interval is 20 W m^{-2}. Values larger than 80 W m^{-2} are shaded.

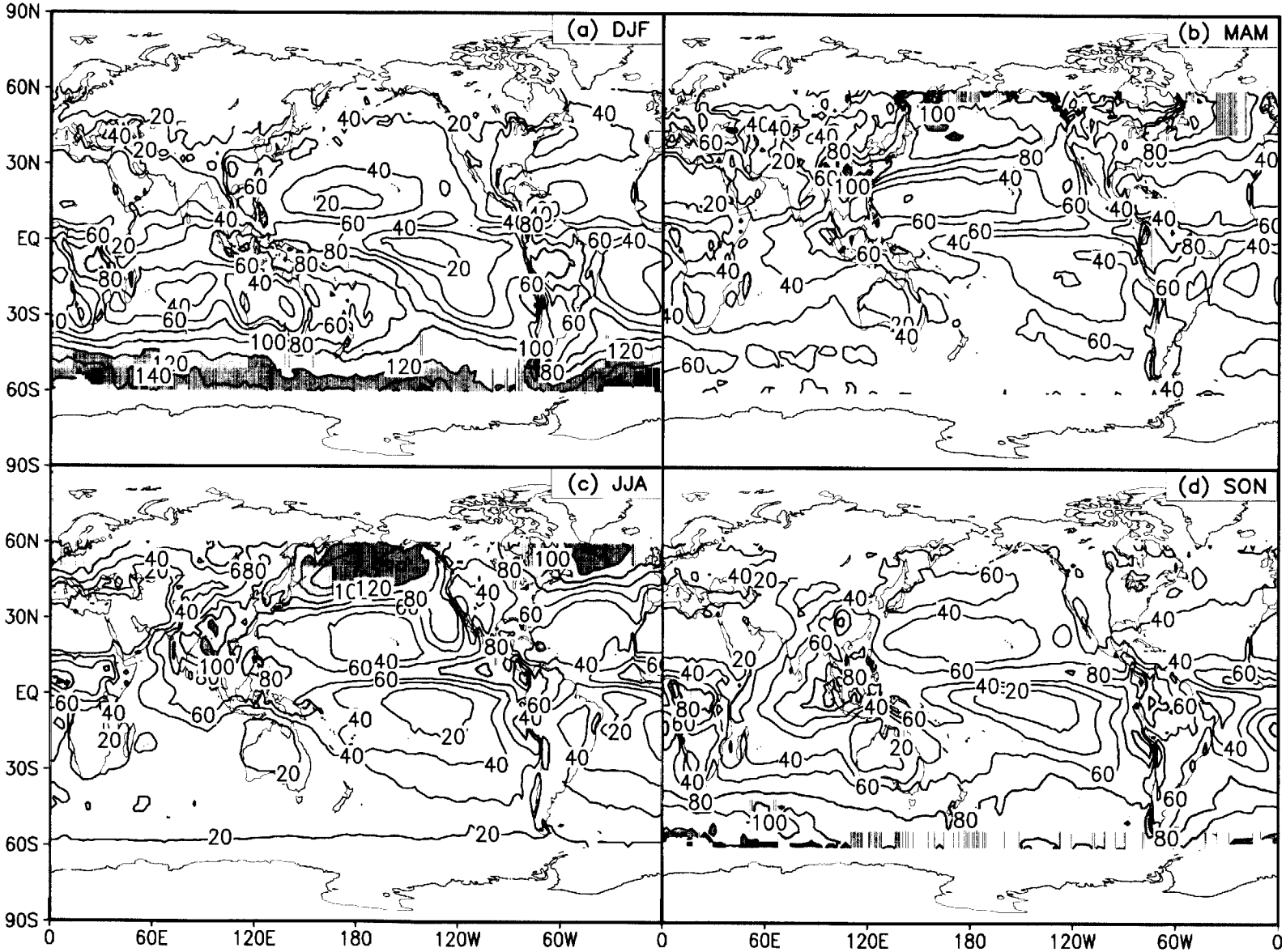

Figure 33: Seasonal means of shortwave cloud radiative forcing for ERBS data during 1981–1991. The contour interval is 20 W m^{-2}. Values larger than 80 W m^{-2} are shaded.

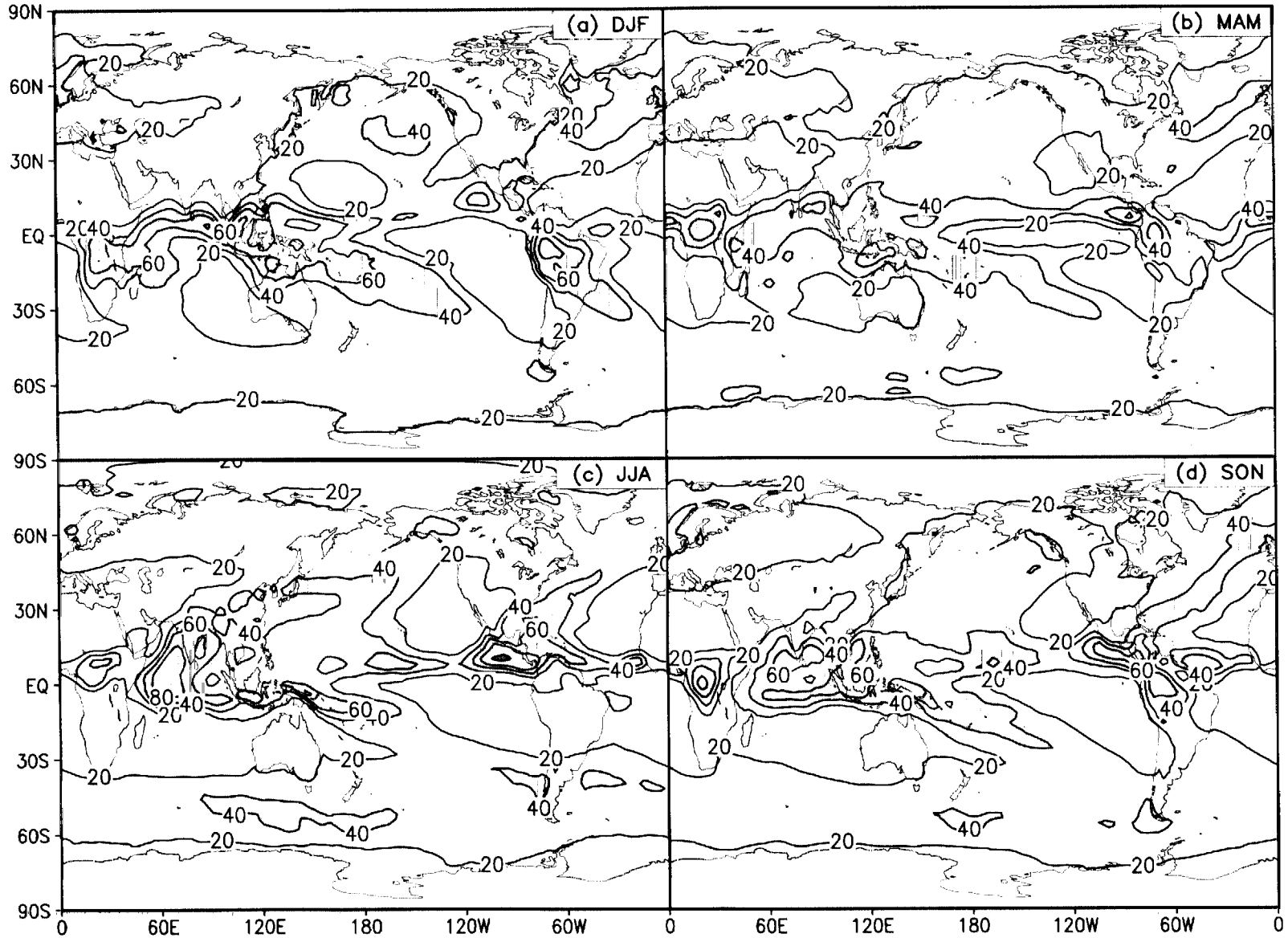

Figure 34: Seasonal means of longwave cloud radiative forcing for the model during 1985–1991. The contour interval is 20 W m^{-2}. Values larger than 40 W m^{-2} are shaded.

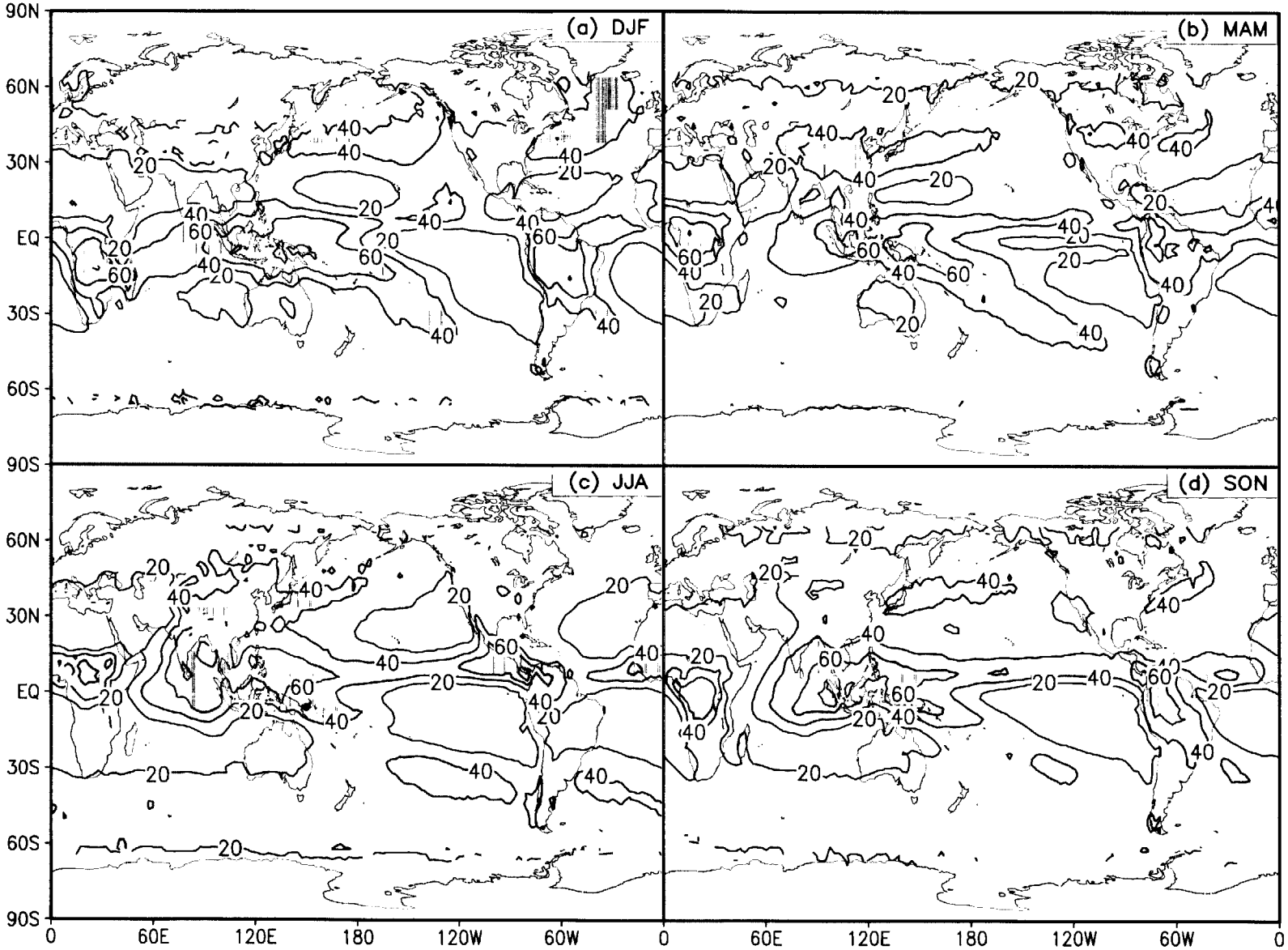

Figure 35: Seasonal means of longwave cloud radiative forcing for ERBS data during 1985–1991. The contour interval is 20 W m $^{-2}$. Values larger than 40 W m^{-2} are shaded.

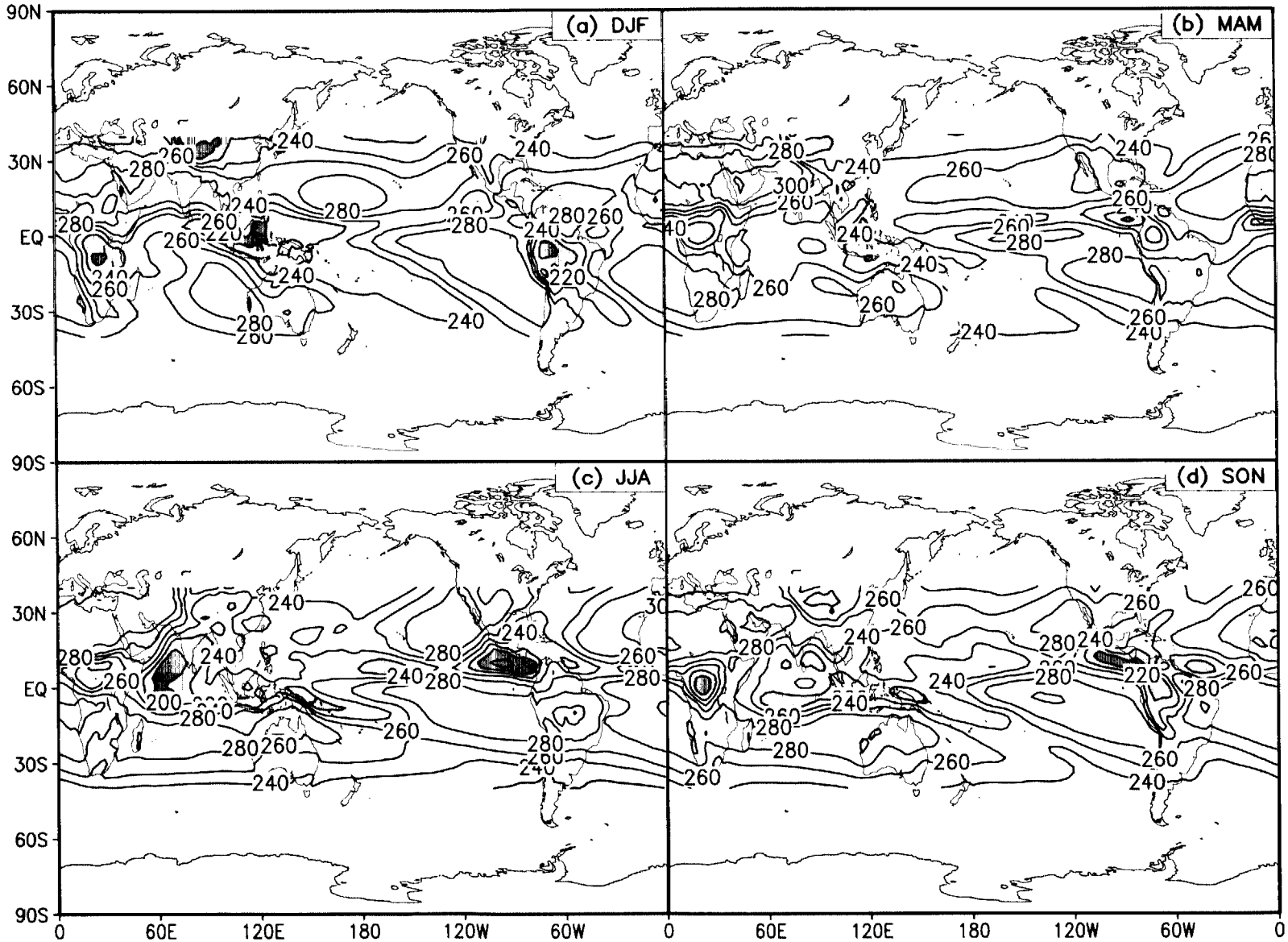

Figure 36: Seasonal means of outgoing longwave radiation for the model during 1980–1995. The contour interval is 20 W m^{-2}. Values less than 220 W m^{-2} are shaded.

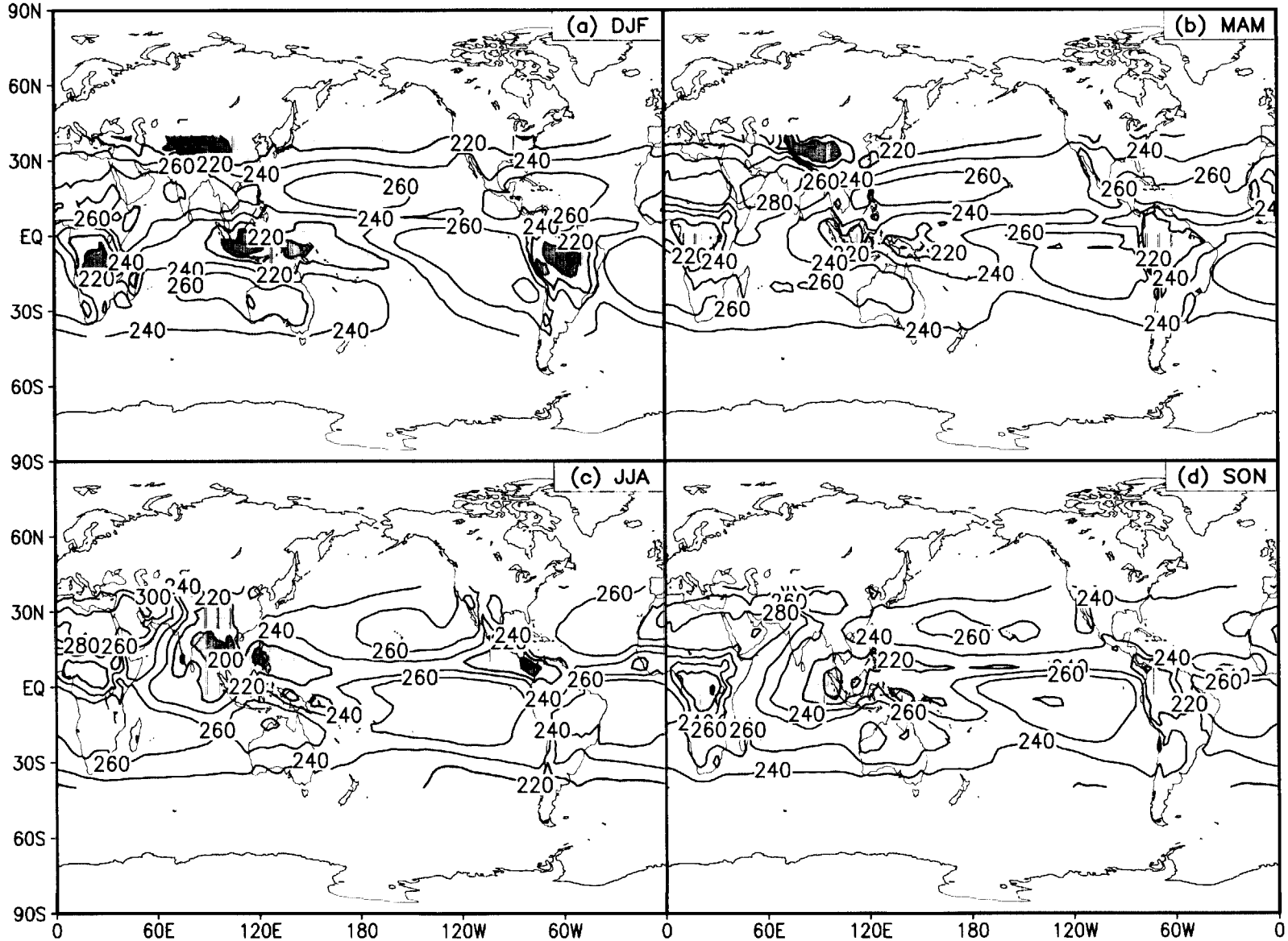

Figure 37: Seasonal means of outgoing longwave radiation for NOAA data during 1980–1995. The contour interval is 20 W m^{-2}. Values less than 220 W m^{-2} are shaded.

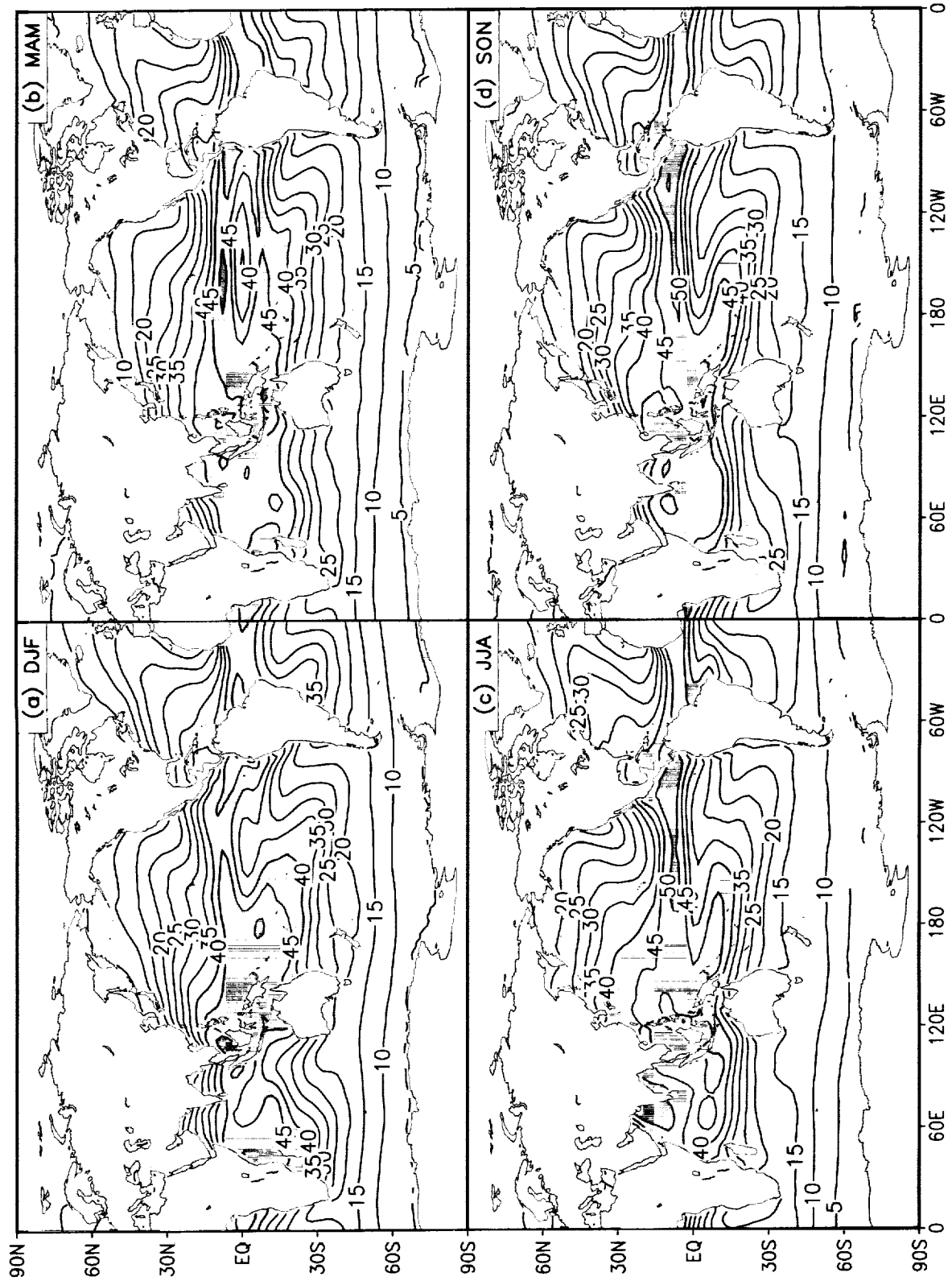

Figure 38: Seasonal means of total precipitable water for the model during Jul 1987–Jan 1992. The contour interval is 5 kg m^{-2}. Values larger than 40 kg m^{-2} are shaded.

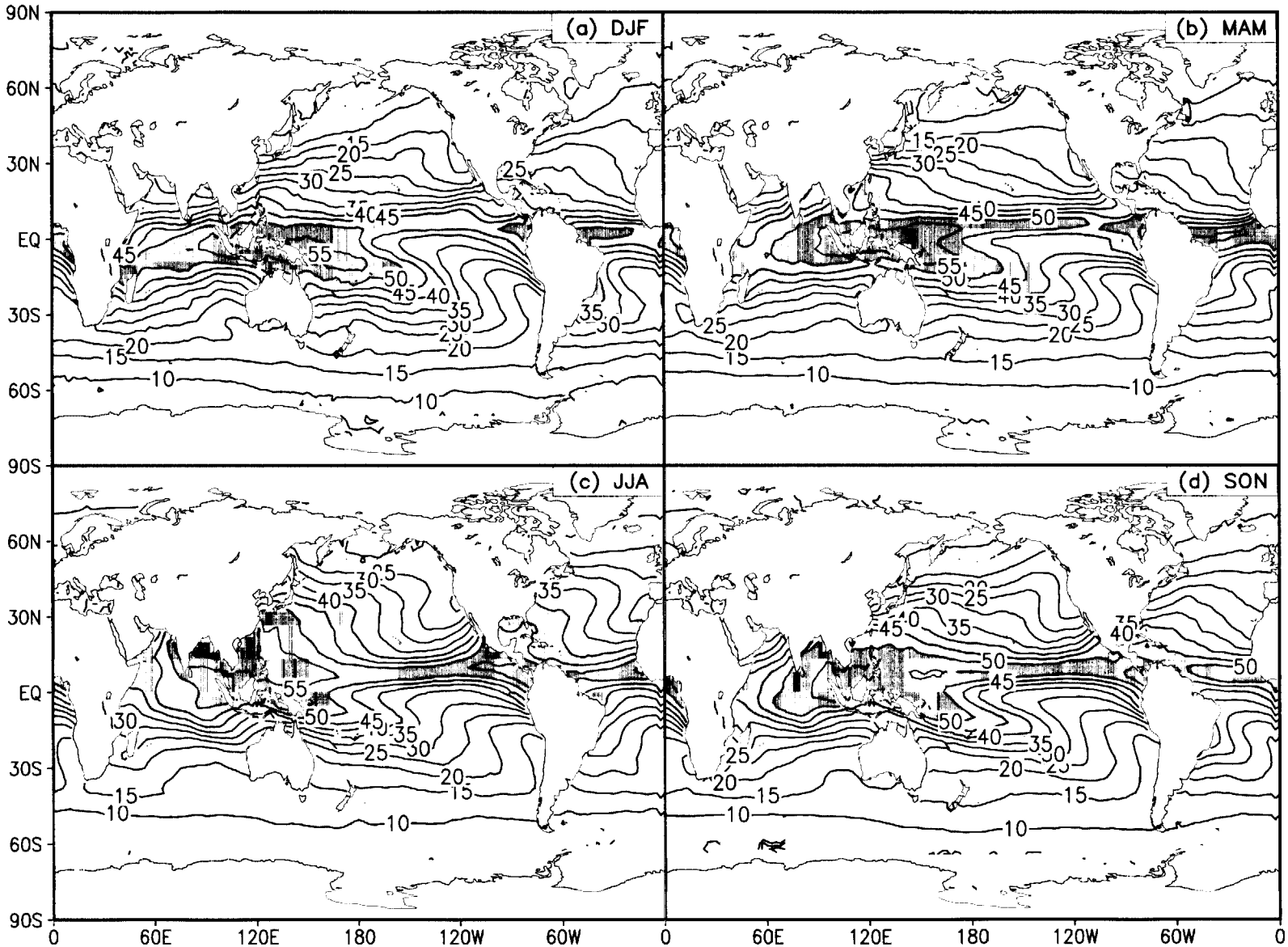

Figure 39: Seasonal means of total precipitable water for SSM/I data during Jul 1987–Jan 1992. The contour interval is 5 kg m^{-2}. Values larger than 40 kg m^{-2} are shaded.

INTERANNUAL VARIABILITY OF SEASONAL MEANS

50mb zonal wind

200mb zonal wind

850mb zonal wind

300mb height

200mb stream function

200mb velocity potential

Sea level pressure

Precipitation

Figure 40: Standard deviation of 50 mb u-wind for the model. The contour interval is 1 m s^{-1}. Values larger than 4 m s^{-1} are shaded.

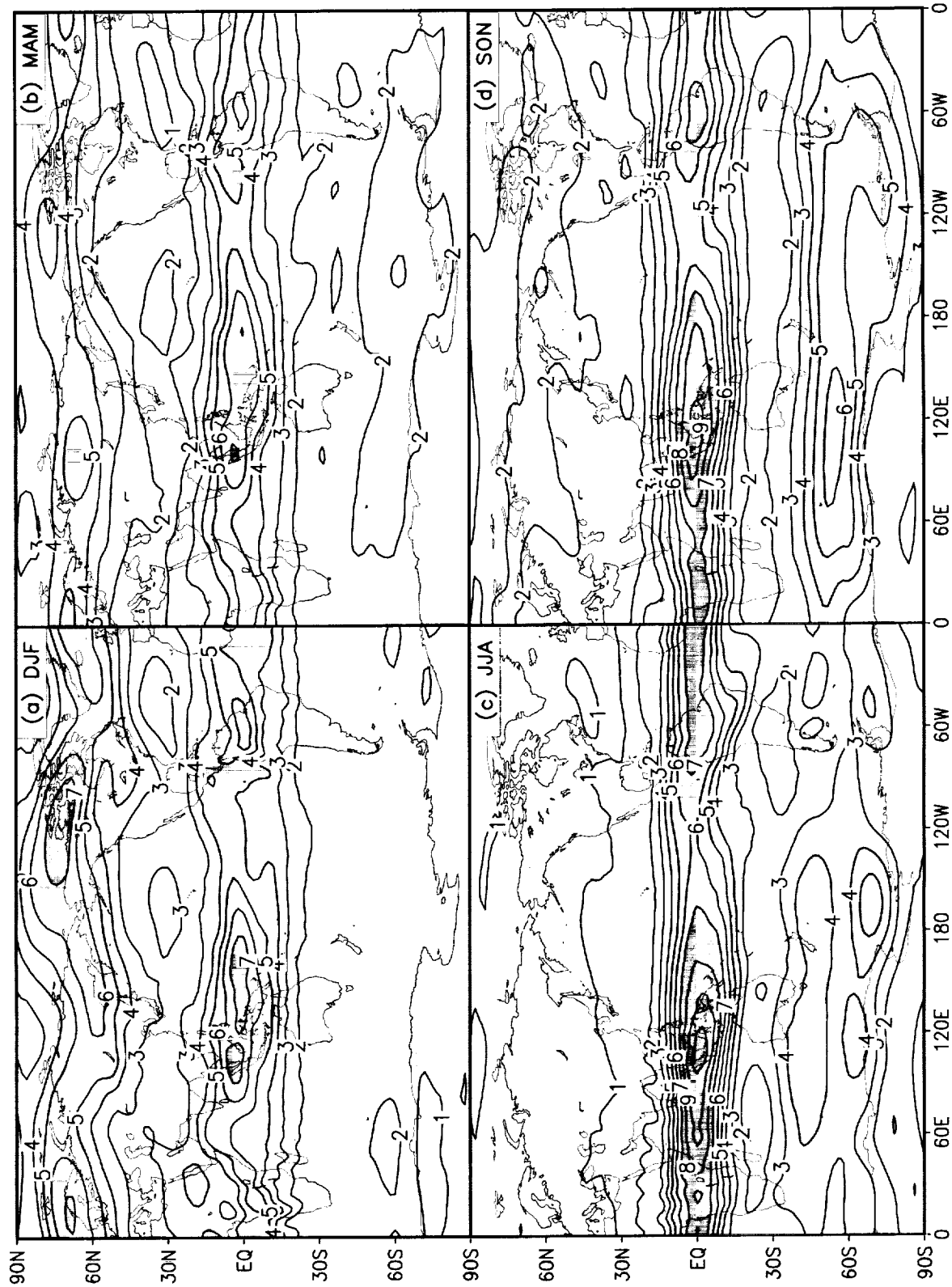

Figure 41: Standard deviation of 50 mb u-wind for the reanalysis. The contour interval is 1 m s^{-1}. Values larger than 4 m s^{-1} are shaded.

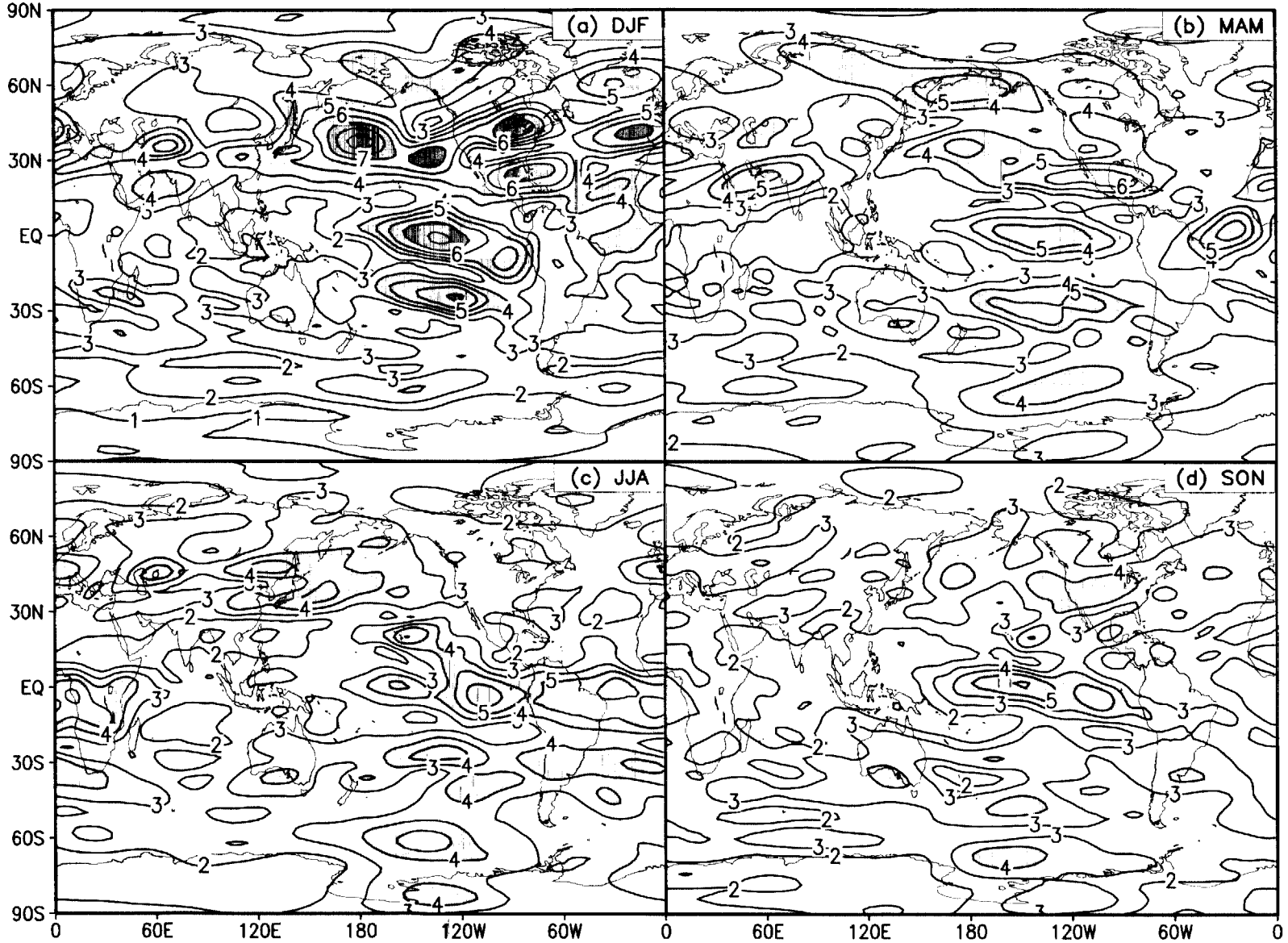

Figure 42: Standard deviation of 200 mb u-wind for the model. The contour interval is 1 m s^{-1}. Values larger than 4 m s^{-1} are shaded.

Figure 43: Standard deviation of 200 mb u-wind for the reanalysis. The contour interval is 1 m s^{-1}. Values larger than 4 m s^{-1} are shaded.

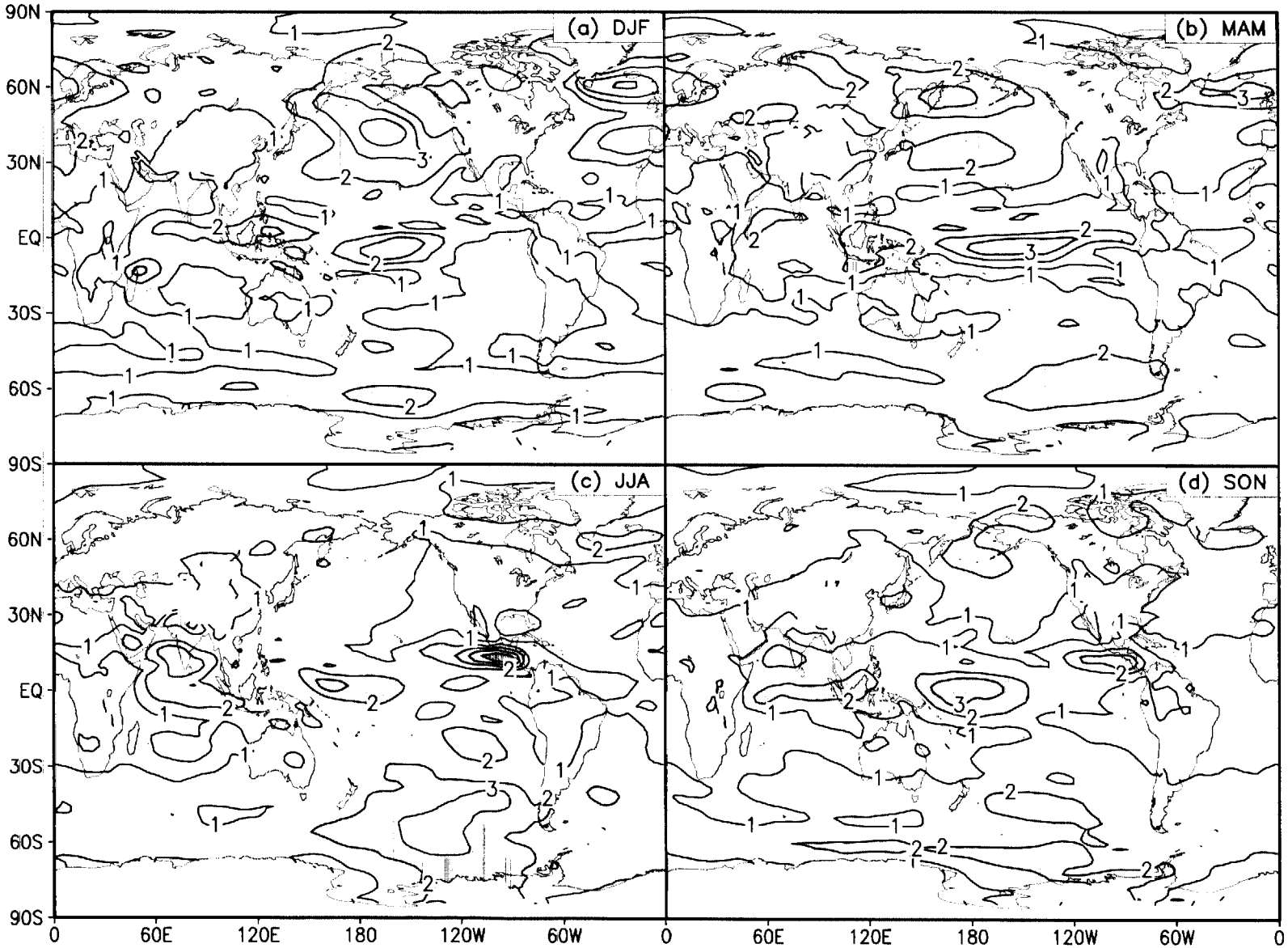

Figure 44: Standard deviation of 850 mb u-wind for the model. The contour interval is 1 m s^{-1}. Values larger than 2 m s^{-1} are shaded.

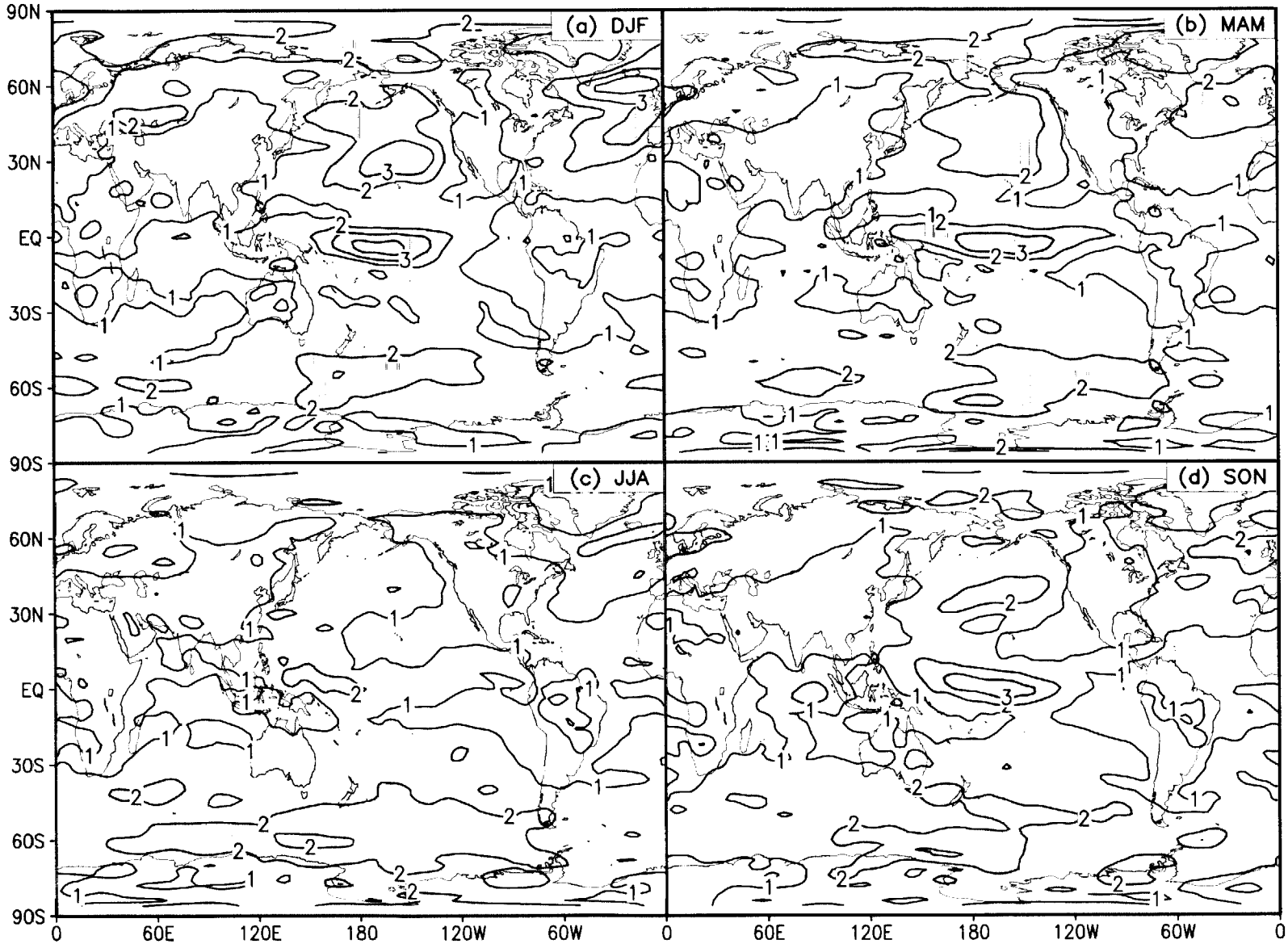

Figure 45: Standard deviation of 850 mb u-wind for the reanalysis. The contour interval is 1 m s^{-1}. Values larger than 2 m s^{-1} are shaded.

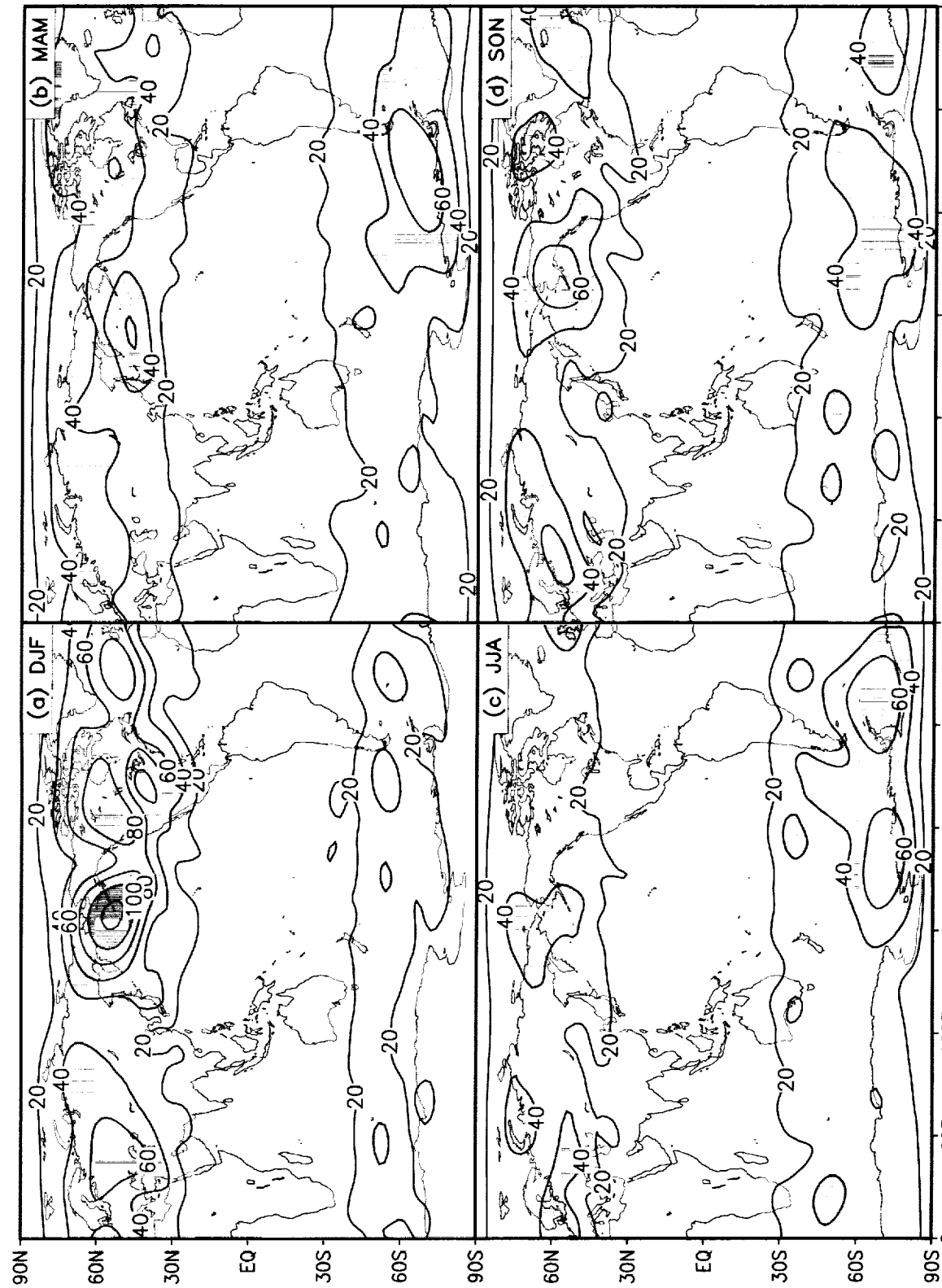

Figure 46: Standard deviation of 300 mb height for the model. The contour interval is 20 m. Values larger than 40 m are shaded.

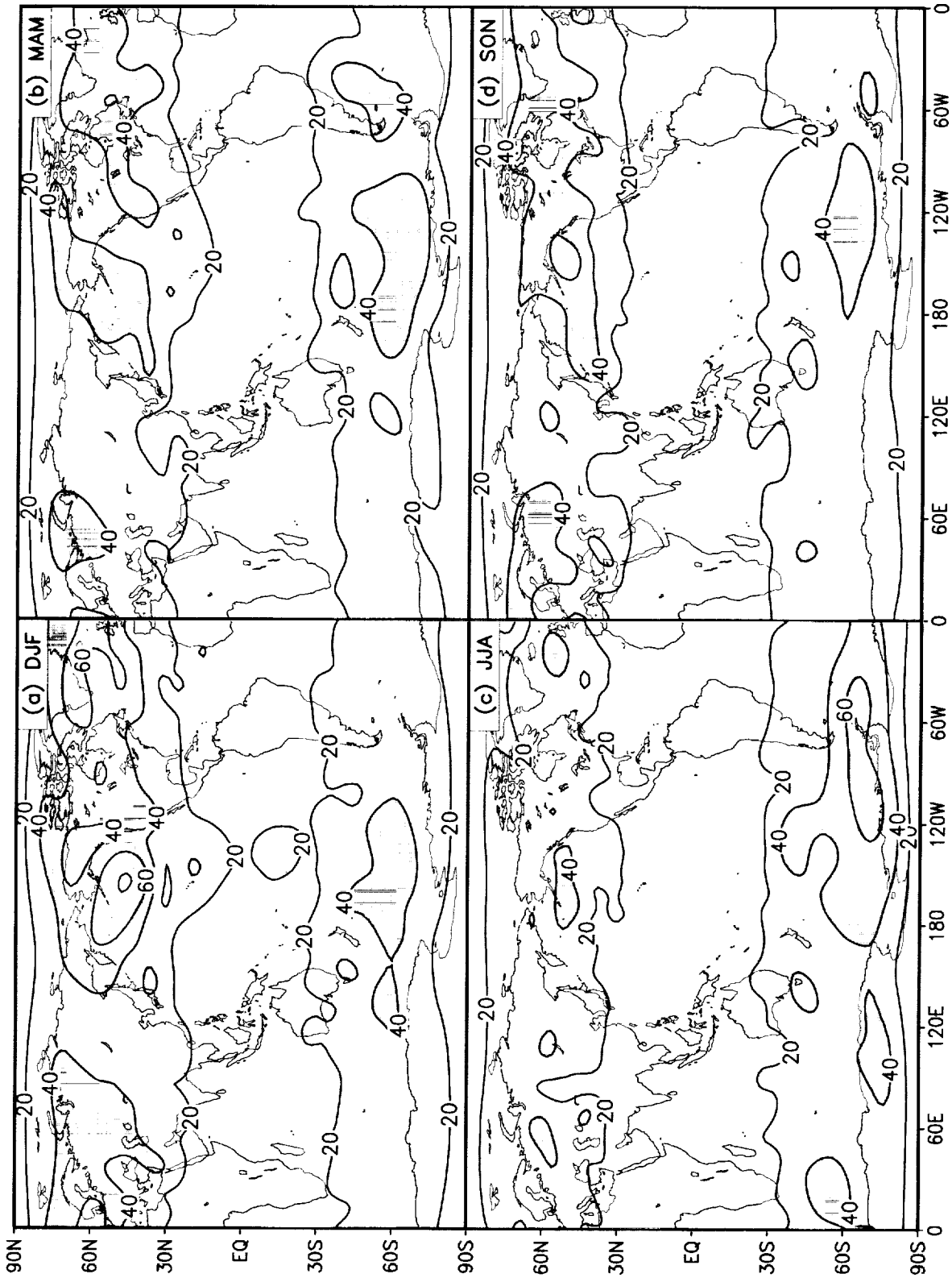

Figure 47: Standard deviation of 300 mb height for the reanalysis. The contour interval is 20 m. Values larger than 40 m are shaded.

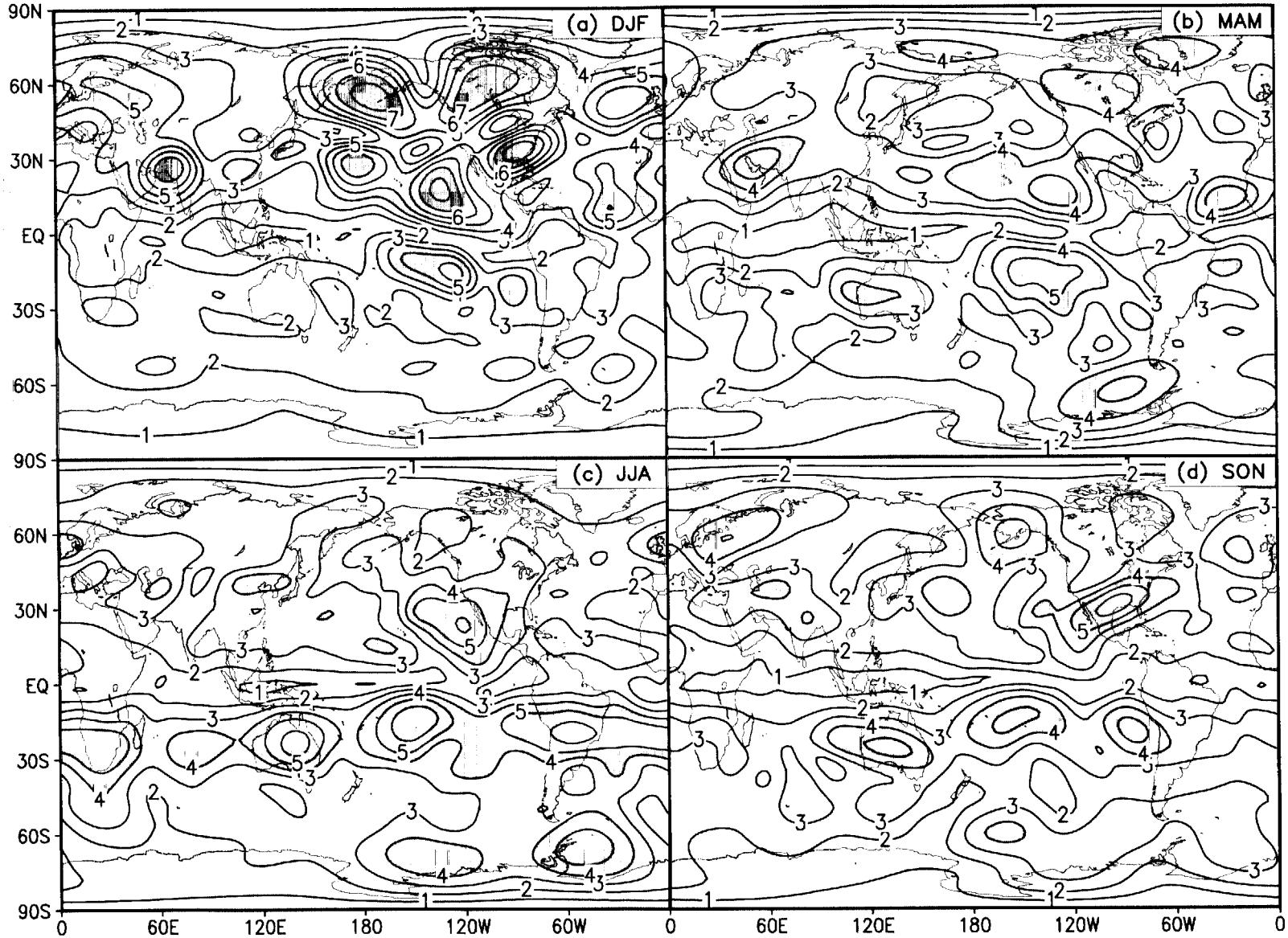

Figure 48: Standard deviation of 200 mb streamfunction from the model. The contour interval is 1×10^6 m^2 s^{-1}. Values larger than 4×10^6 m^2 s^{-1} are shaded.

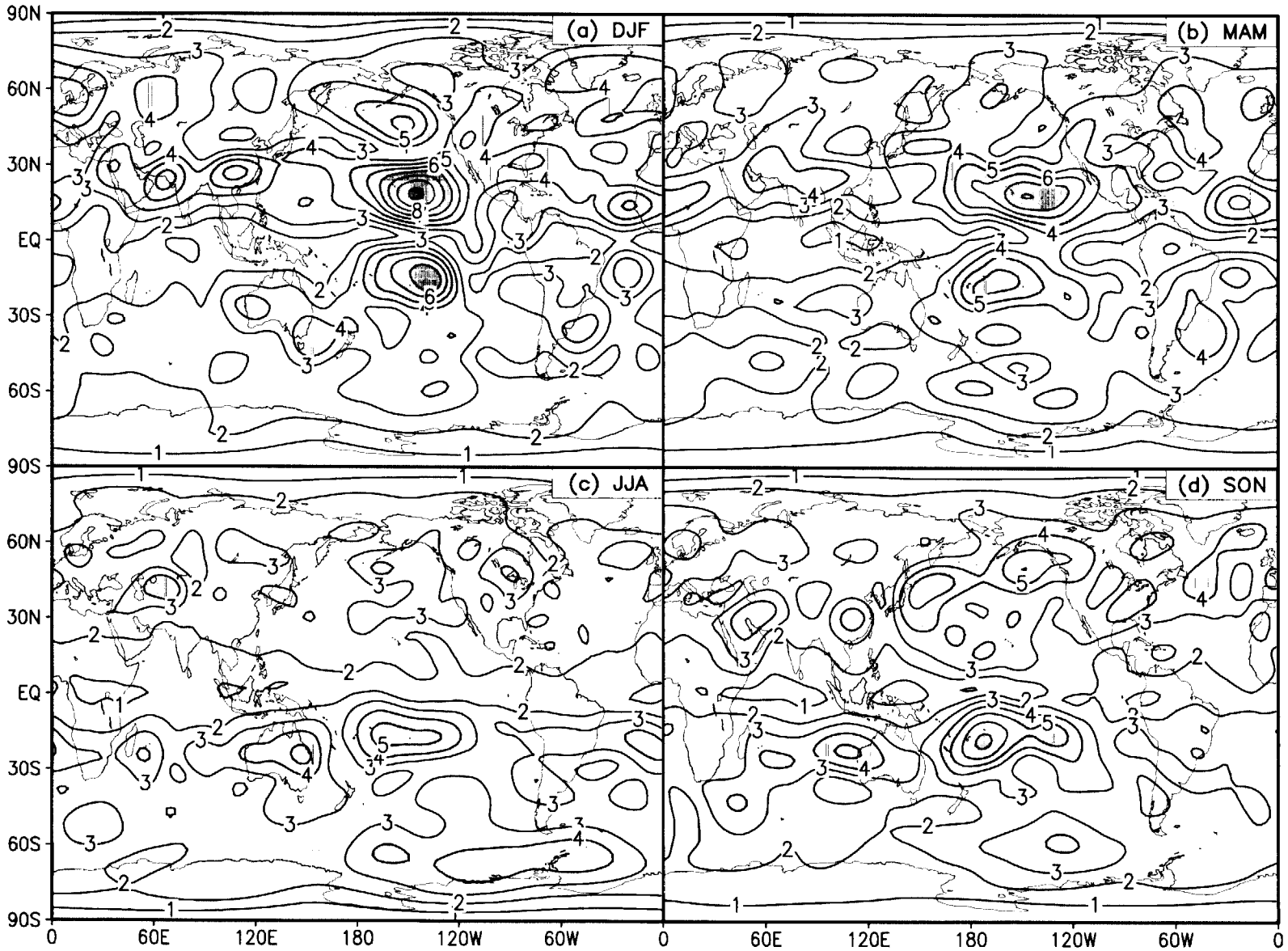

Figure 49: Standard deviation of 200 mb streamfunction for the reanalysis. The contour interval is 1×10^6 m^2 s^{-1}. Values larger than 4×10^6 m^2 s^{-1} are shaded.

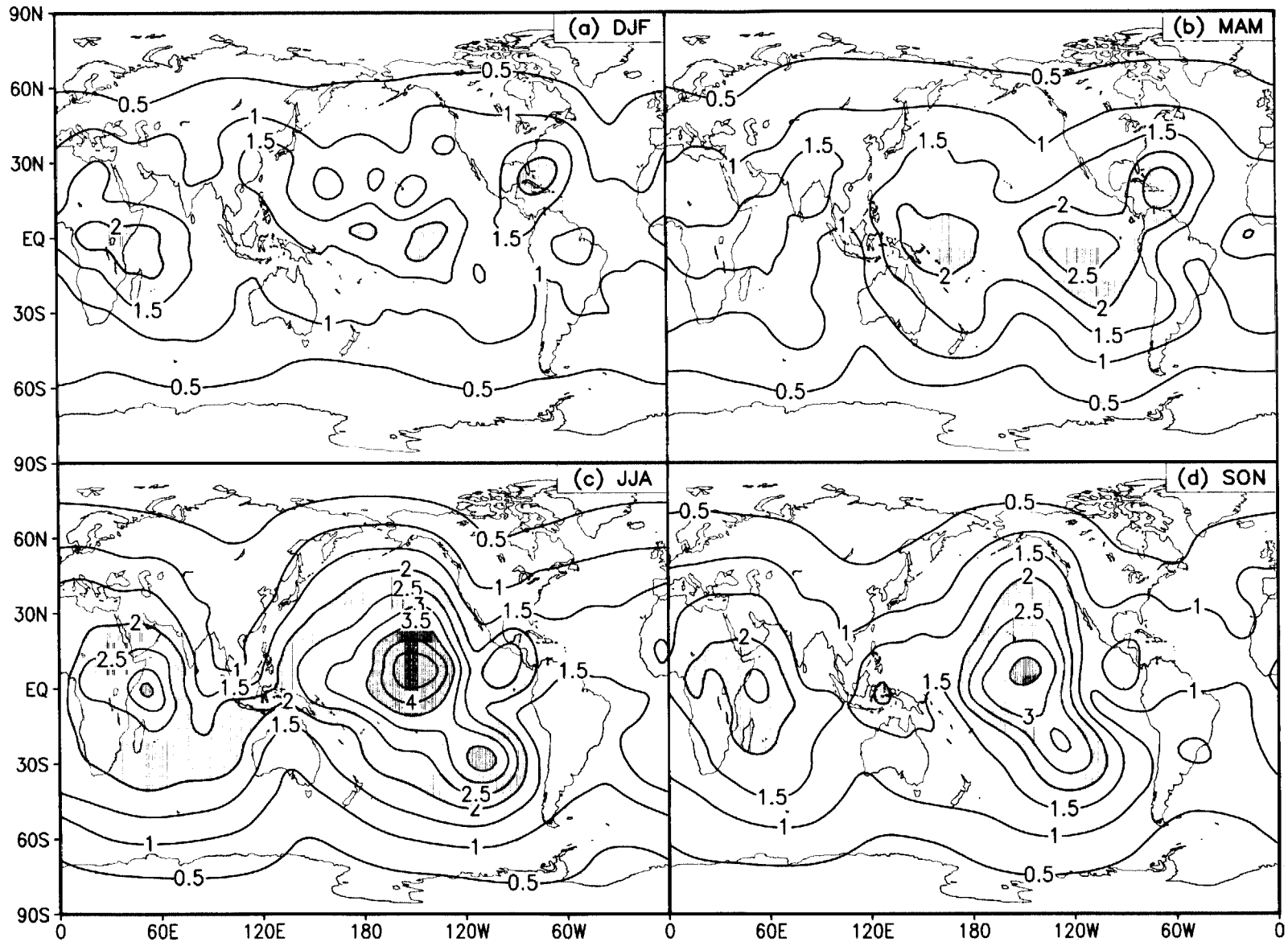

Figure 50: Standard deviation of 200 mb velocity potential for the model. The contour interval is 0.5×10^6 m^2 s^{-1}. Values larger than 2×10^6 m^2 s^{-1} are shaded.

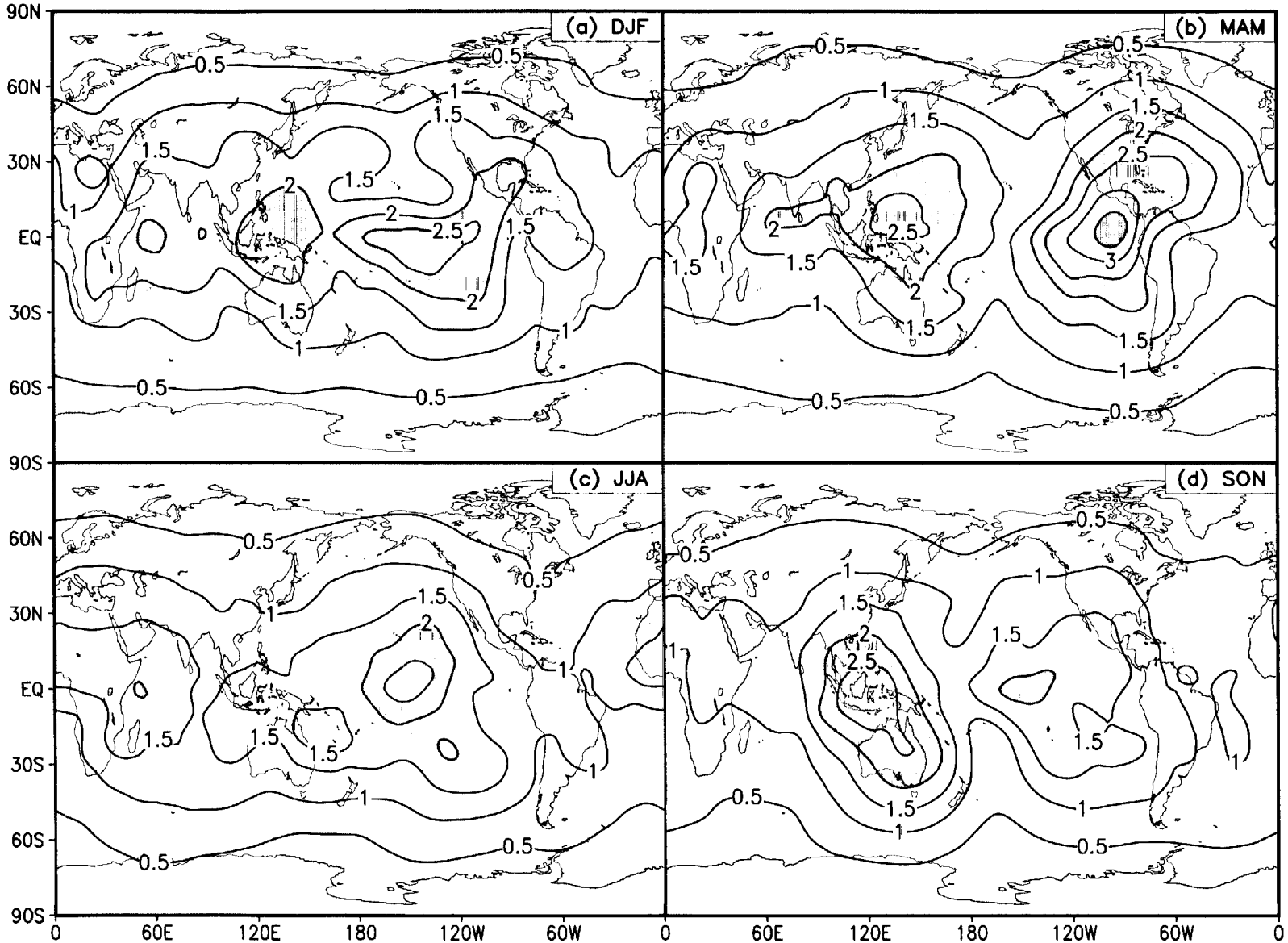

Figure 51: Standard deviation of 200 mb velocity potential for the reanalysis. The contour interval is 0.5×10^6 m^2 s^{-1}. Values larger than 2×10^6 m^2 s^{-1} are shaded.

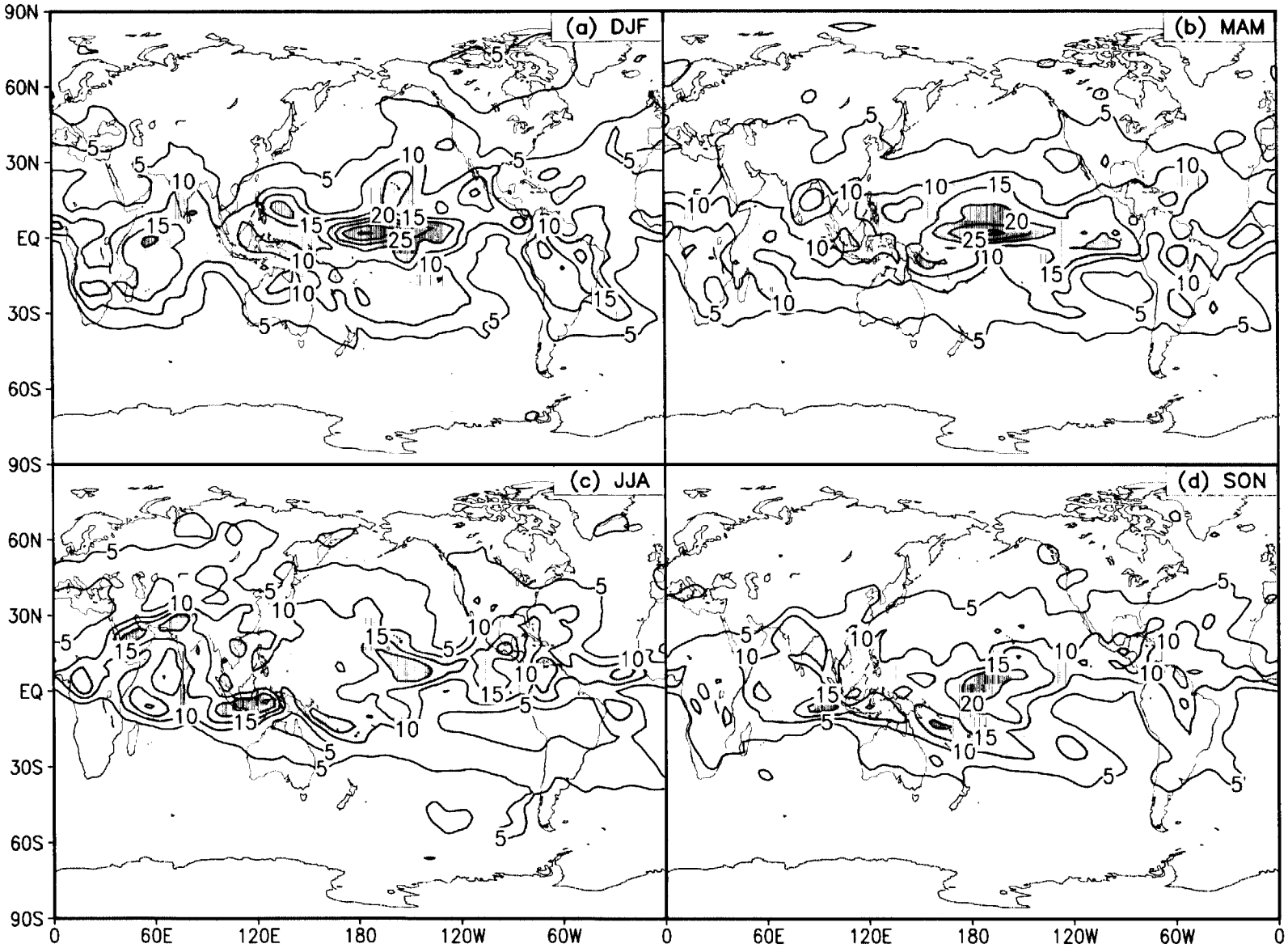

Figure 52: Standard deviation of outgoing longwave radiation for the model. The contour interval is 5 W m^{-2}. Values larger than 10 W m^{-2} are shaded.

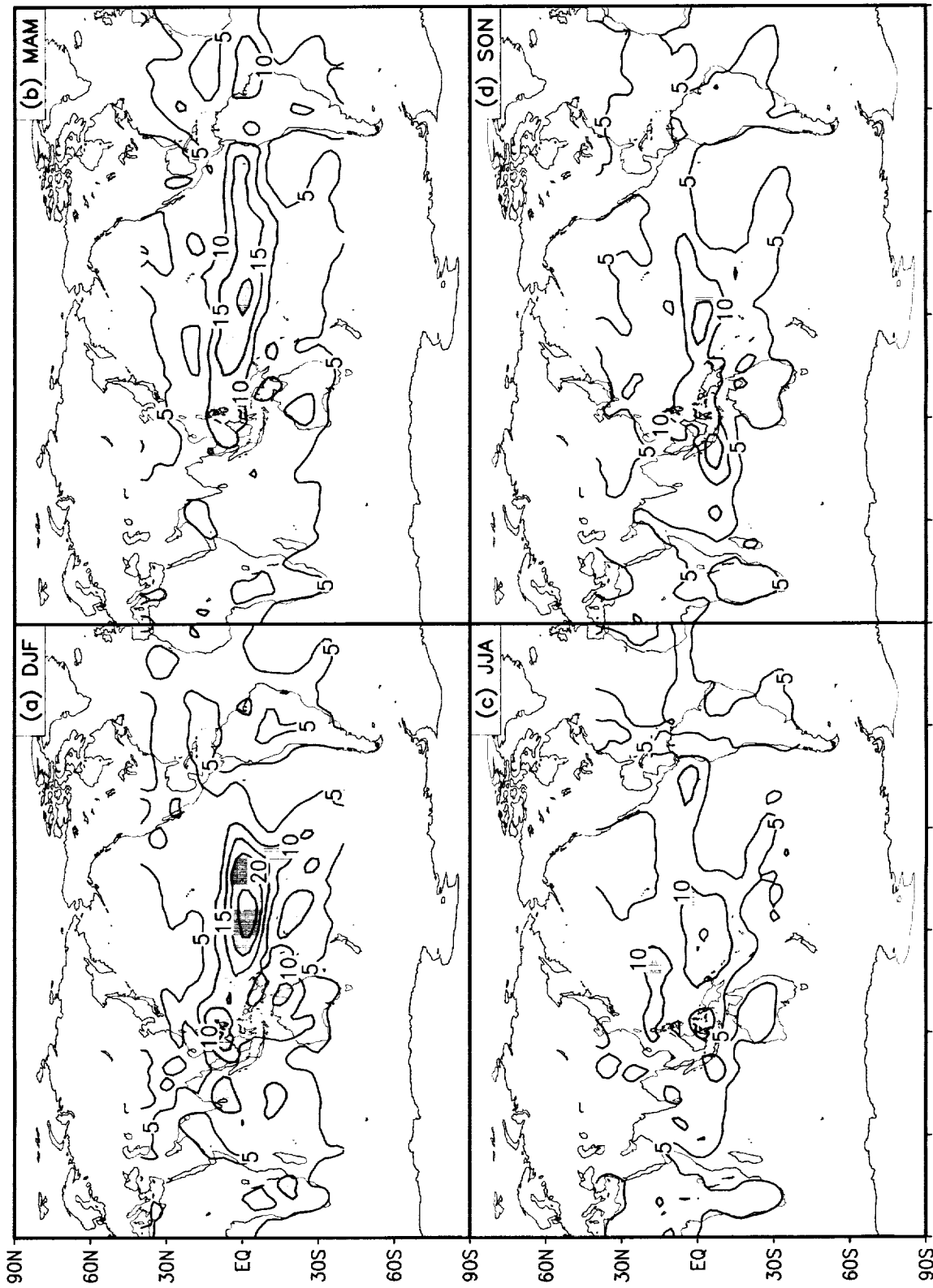

Figure 53: Standard deviation of outgoing longwave radiation for the reanalysis. during 1979–1995. The contour interval is 5 W m^{-2}. Values larger than 10 W m^{-2} are shaded.

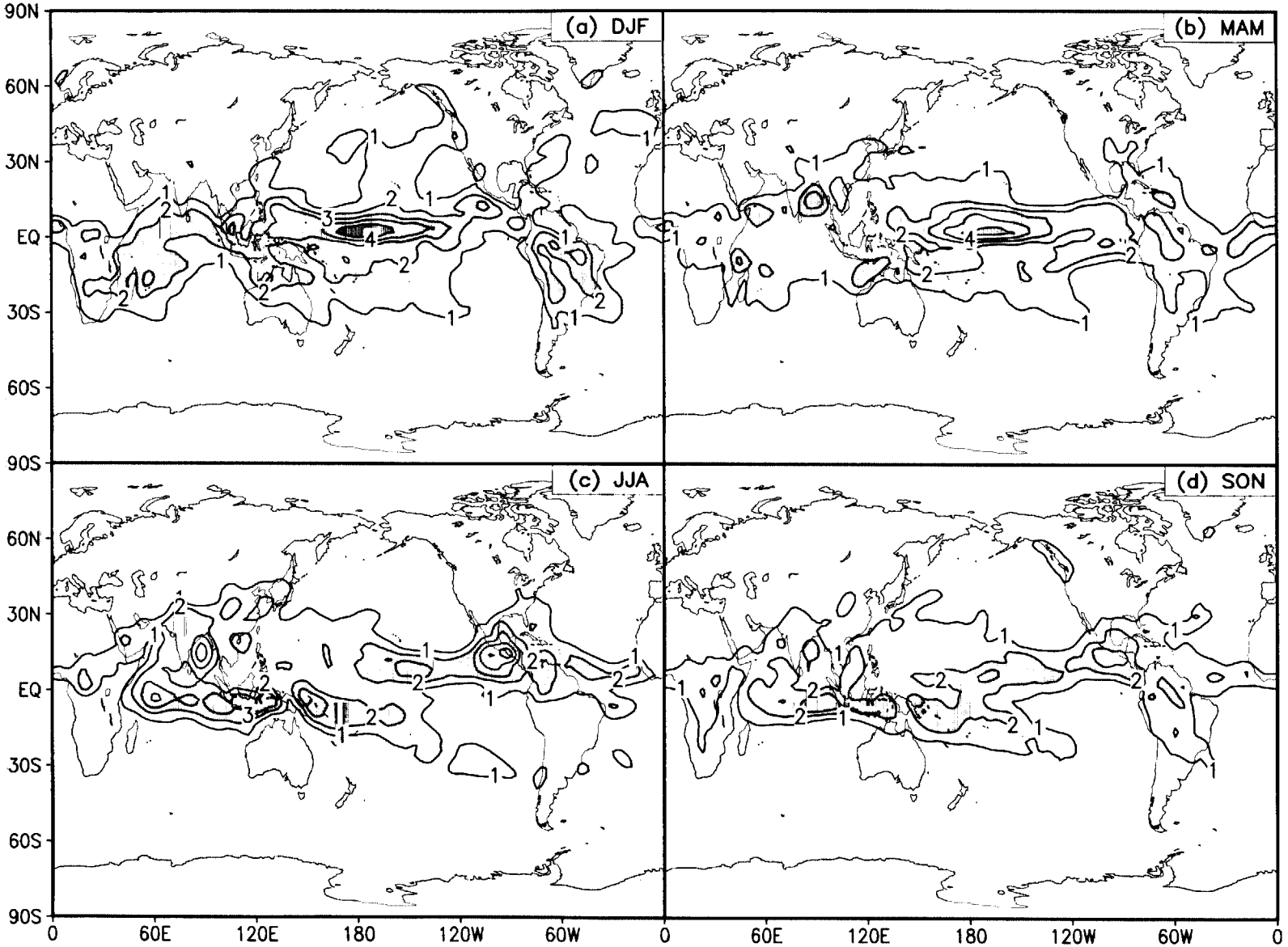

Figure 54: Standard deviation of precipitation for the model during 1980–1995. The contour interval are 1 mm day^{-1}. Values larger than 2 mm day^{-1} are shaded.

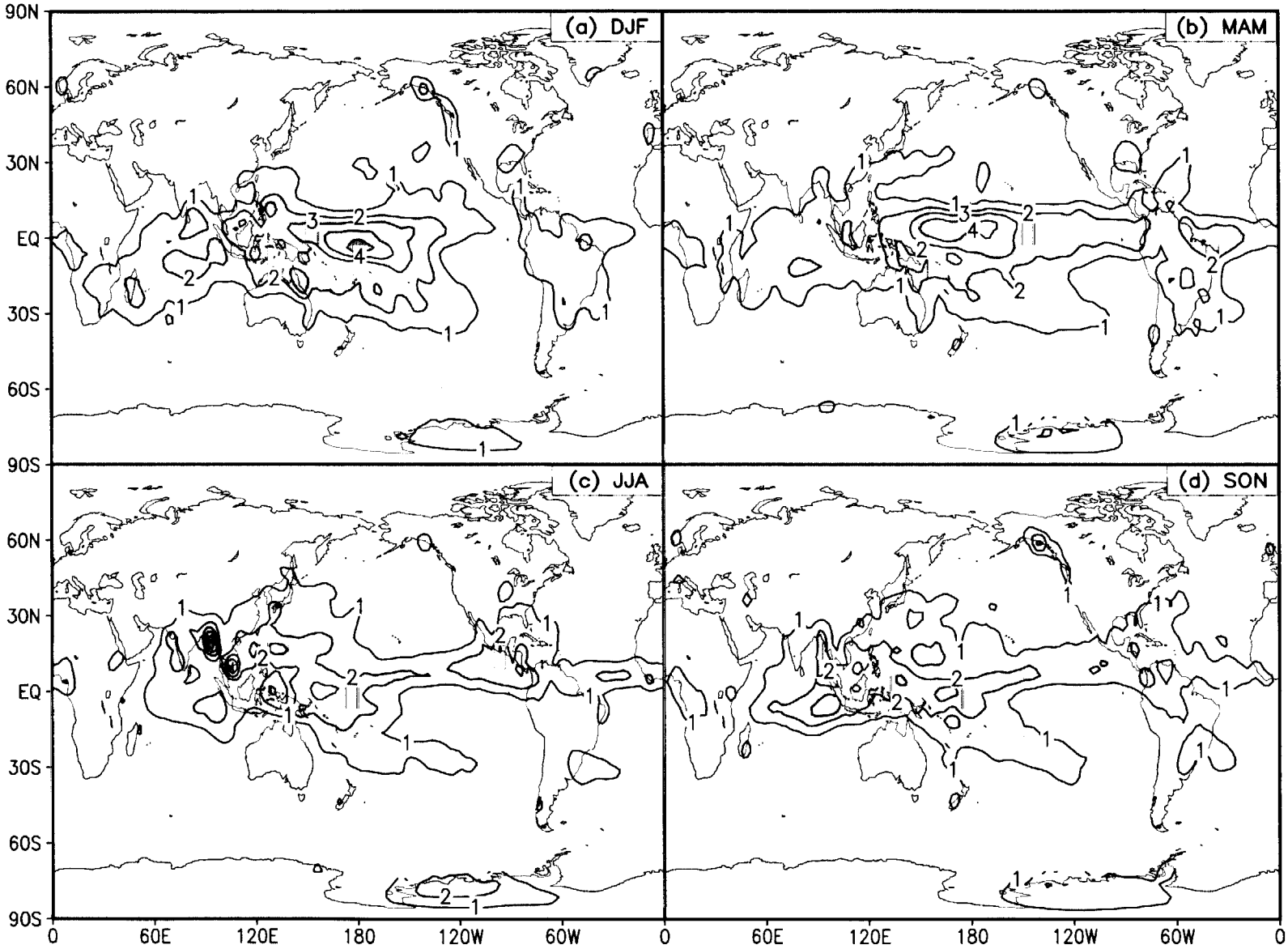

Figure 55: Standard deviation of precipitation for Xie-Arkin data during 1980–1995. The contour interval are 1 mm day^{-1}. Values larger than 2 mm day^{-1} are shaded.

Figure 56: Standard deviation of sea level pressure for the model. The contour interval is 1 mb. Values larger than 4 mb are shaded.

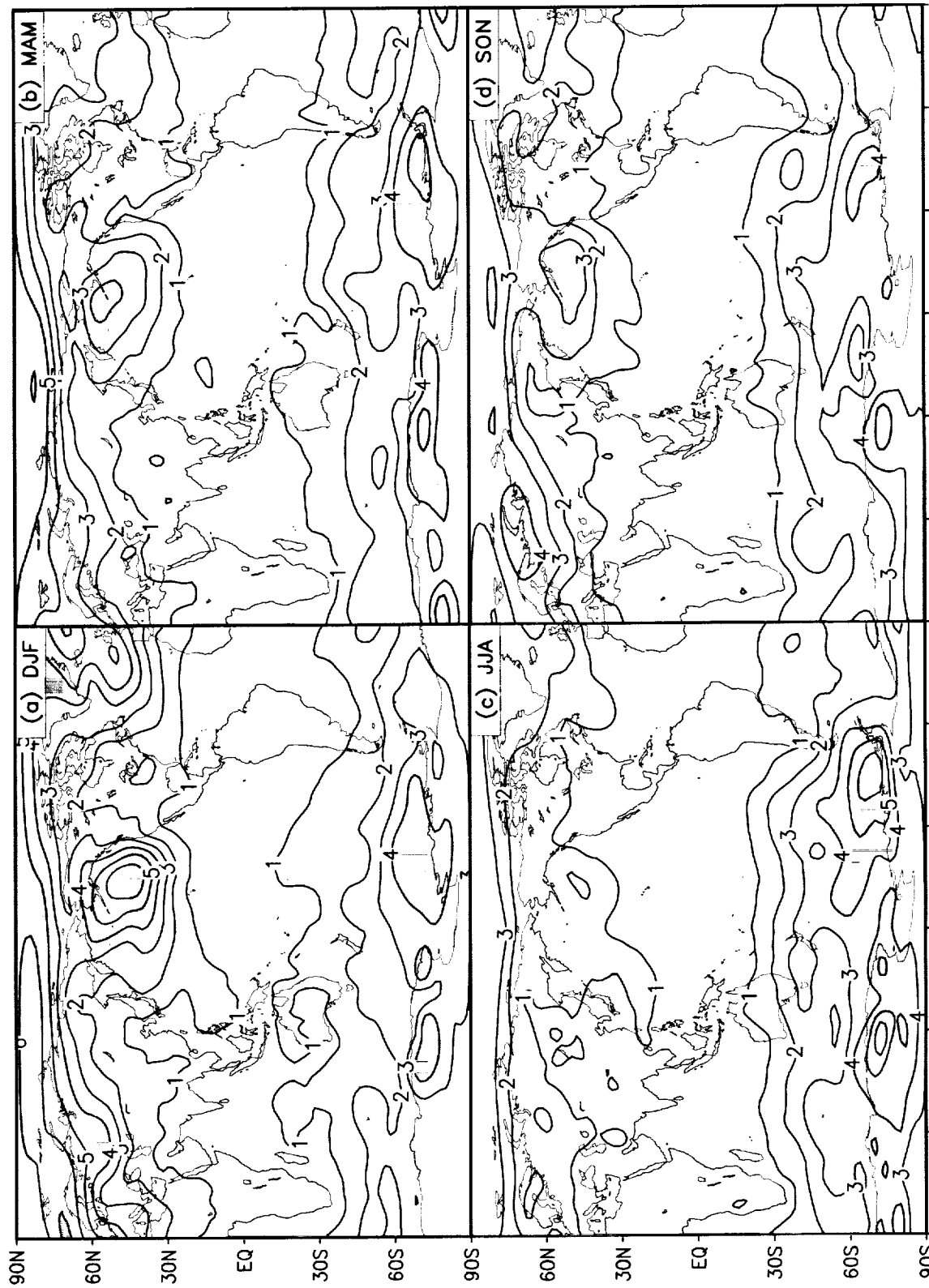

Figure 57: Standard deviation of sea level pressure for the reanalysis. The contour interval is 1 mb. Values larger than 4 mb are shaded.

ZONAL MEAN INTRA-MONTHLY VARIABILITY

Height field

Kinetic energy

u'v'

v'T'

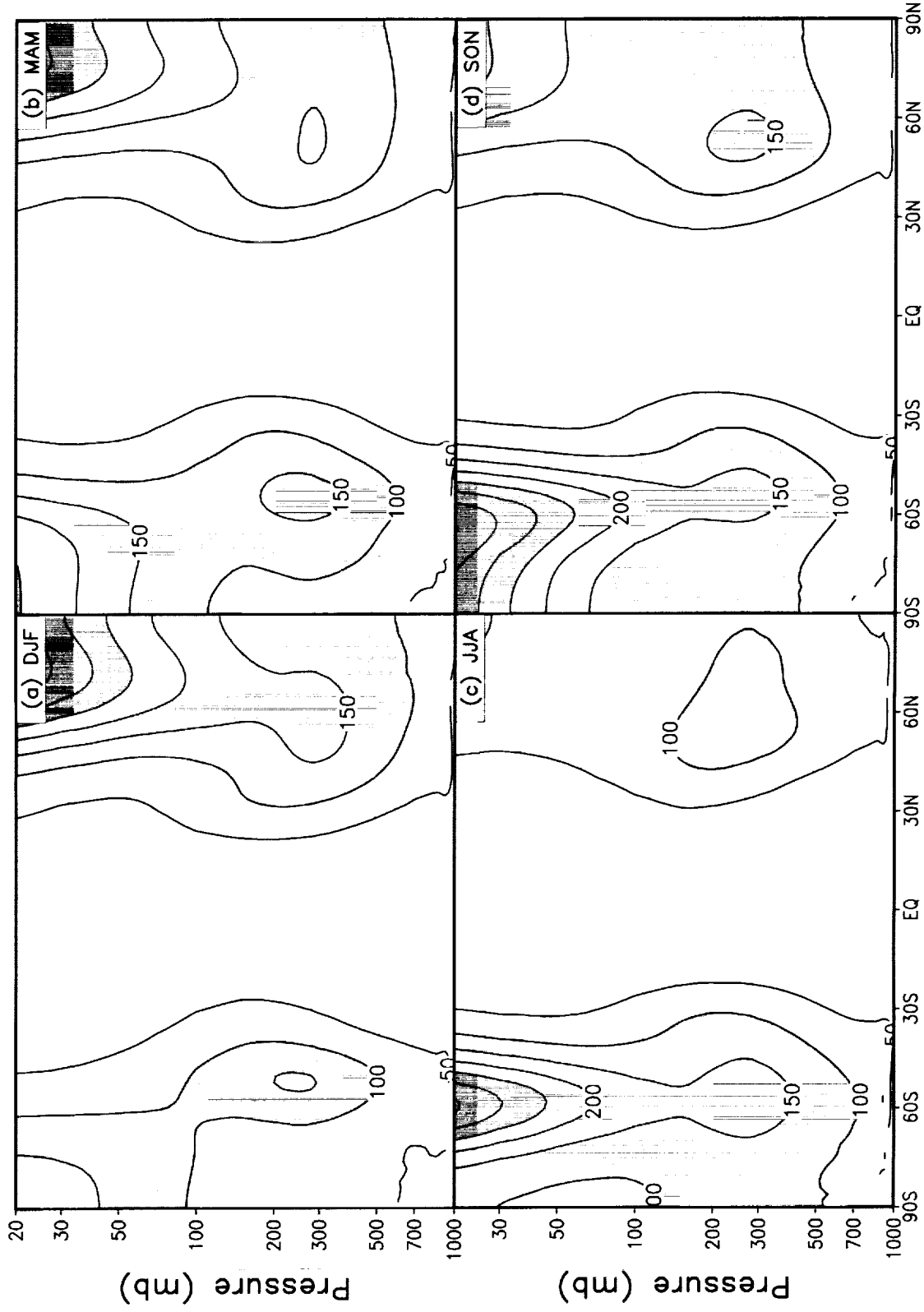

Figure 58: $\sqrt{[z'z']}$ for the model. The contour interval is 50 m. Values larger than 100 m are shaded.

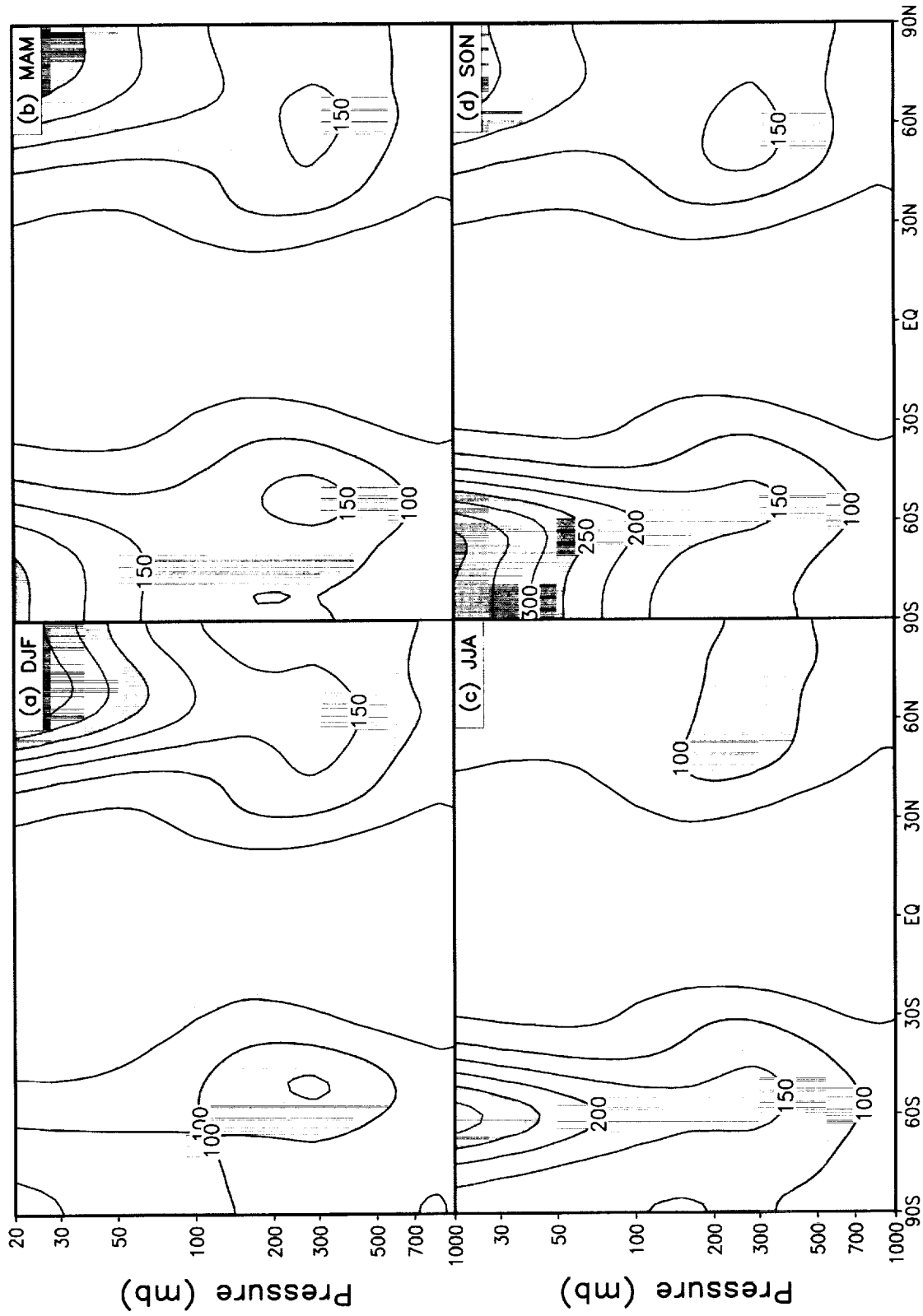

Figure 59: $\sqrt{[z'z']}$ for the reanalysis. The contour interval is 50 m. Values larger than 100 m are shaded.

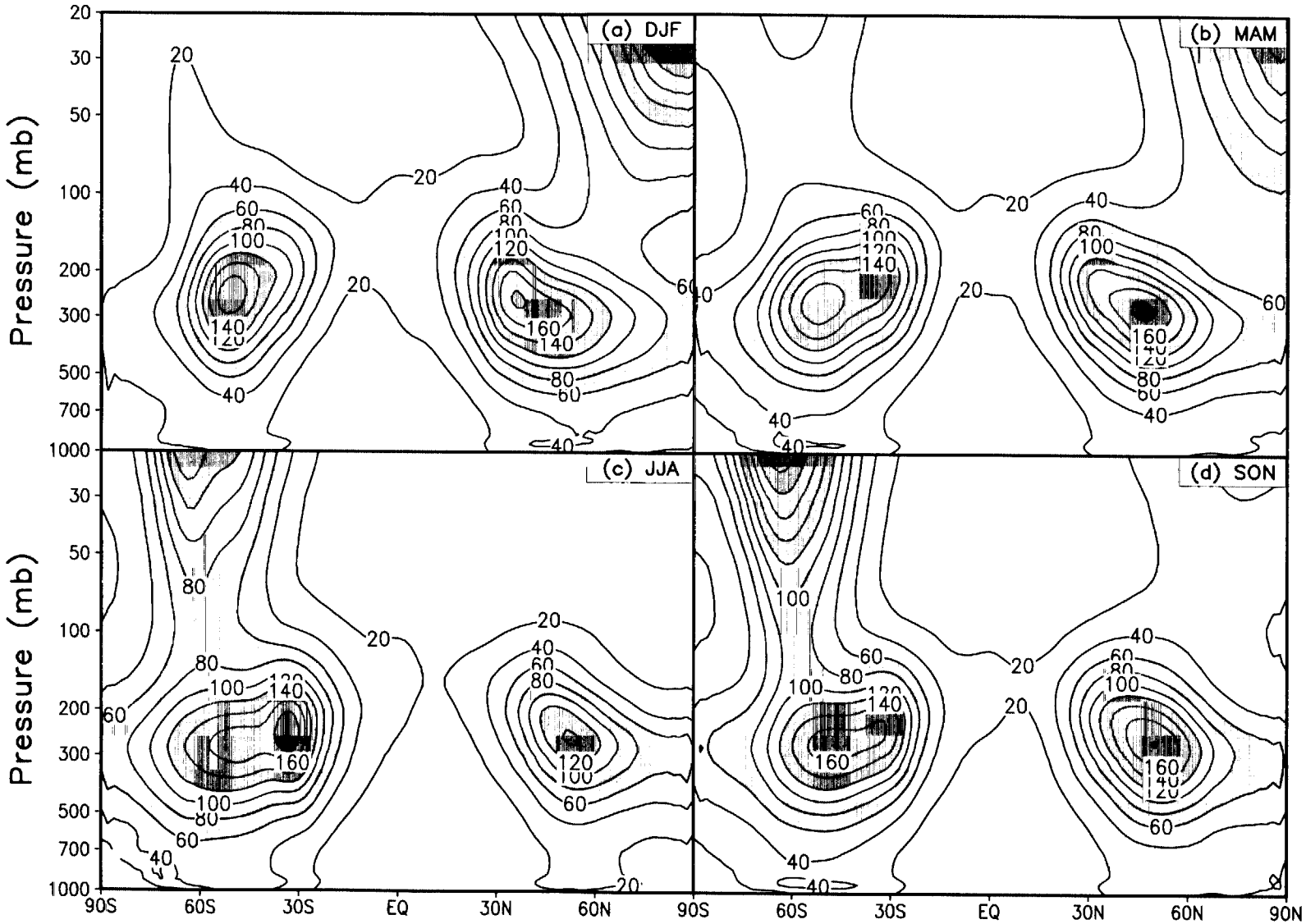

Figure 60: Zonal mean $[\overline{(u'u' + v'v')/2}]$ for the model. The contour interval is 20 $m^2\ s^{-2}$. Values larger than 60 $m^2\ s^{-2}$ are shaded.

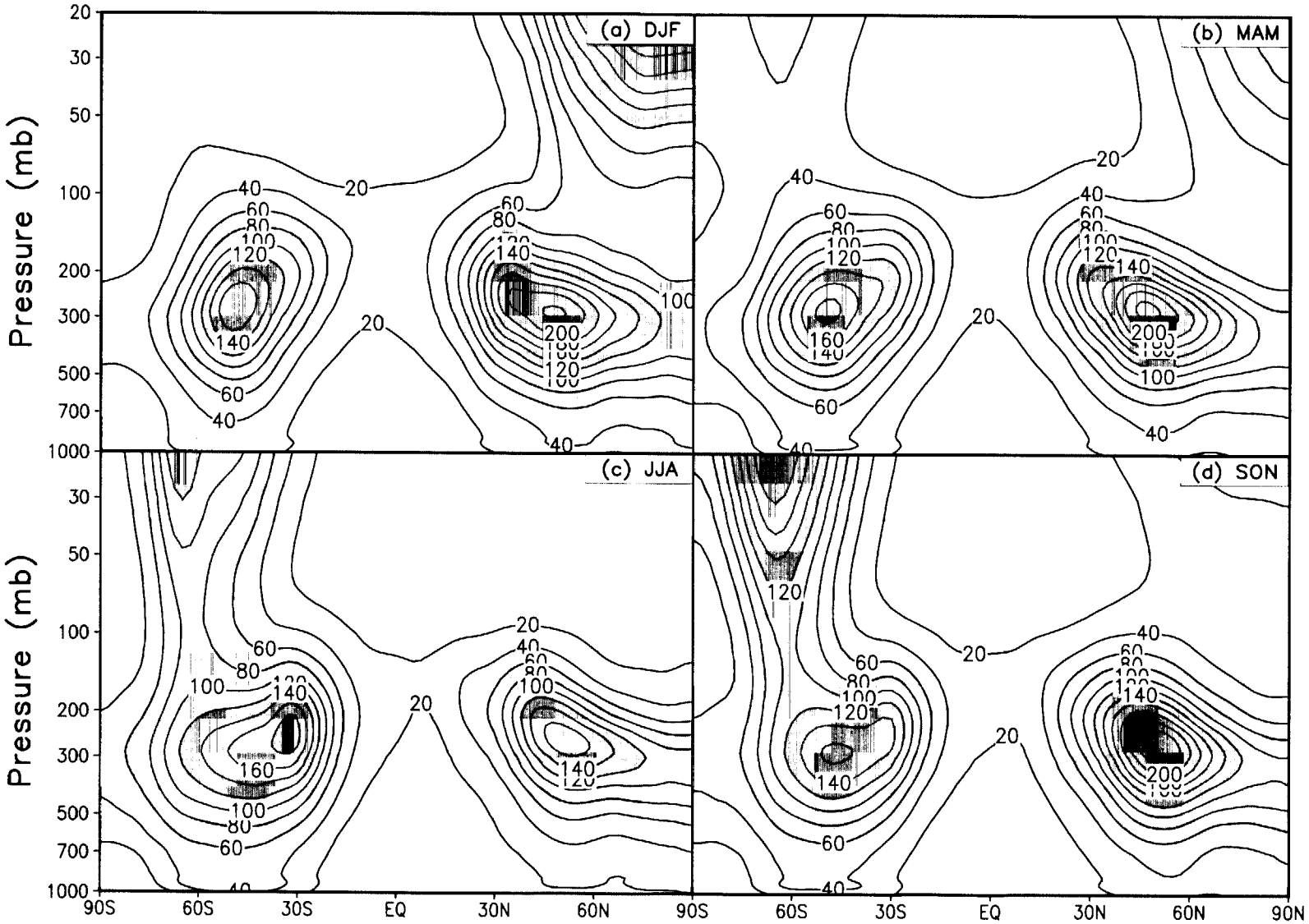

Figure 61: Zonal mean $[\overline{(u'u' + v'v')/2}]$ for the reanalysis. The contour interval is 20 m^2 s^{-2}. Values larger than 60 m^2 s^{-2} are shaded.

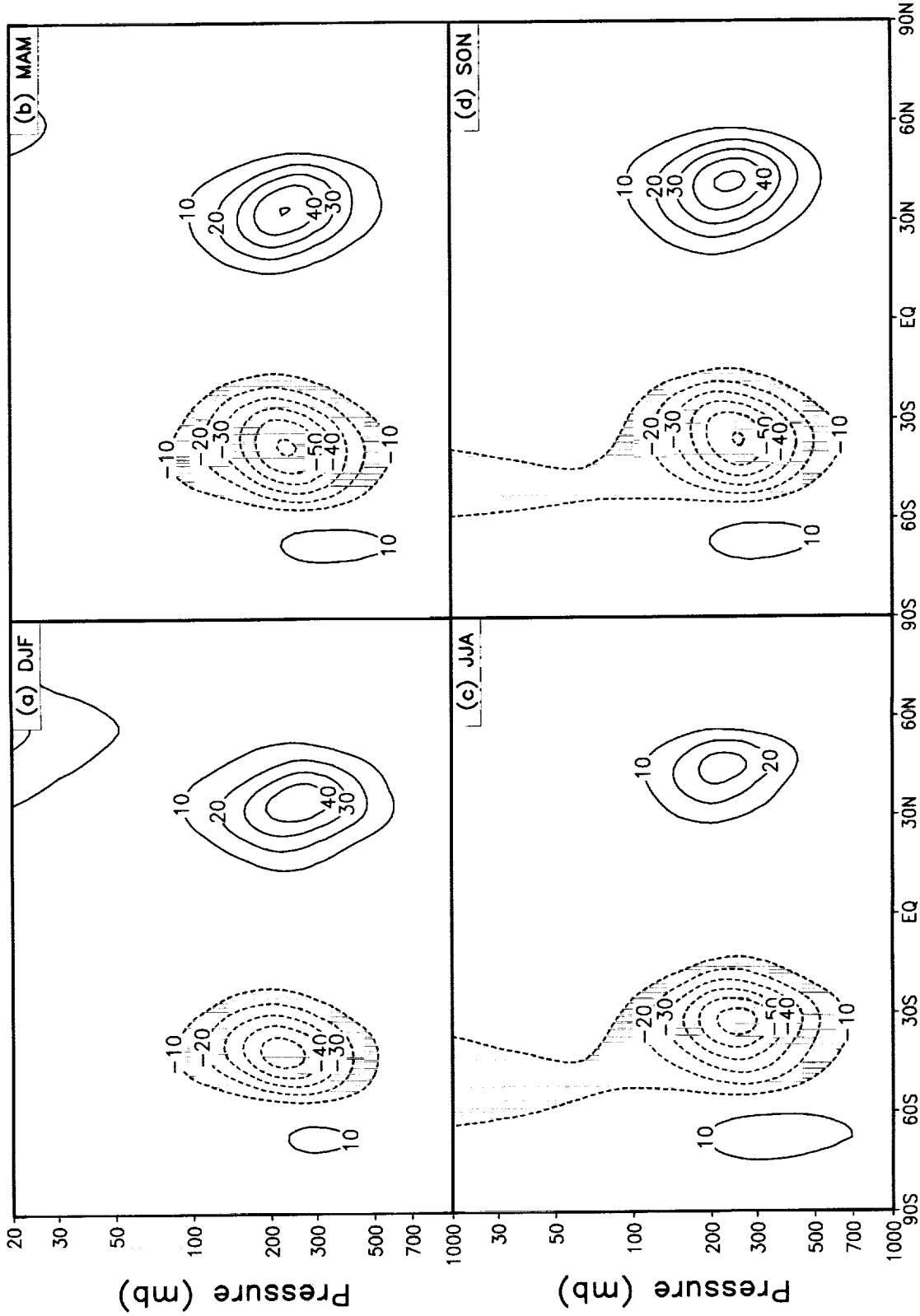

Figure 62: Zonal mean $[\overline{u'v'}]$ for the model. The contour interval is 10 m^2 s^{-2}. Negative values are shaded.

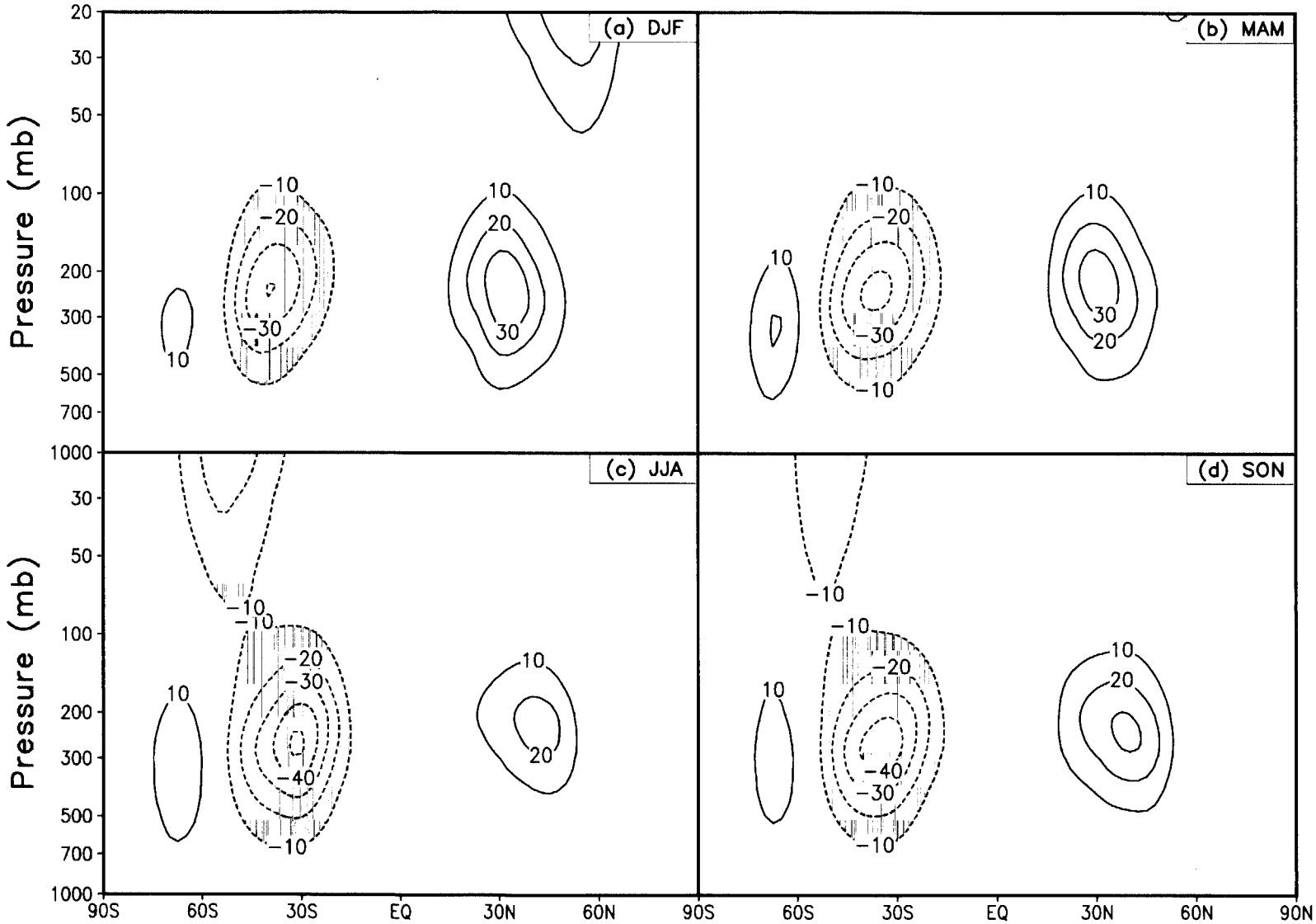

Figure 63: Zonal mean $[\overline{u'v'}]$ for the reanalysis. The contour interval is 10 m^2 s^{-2}. Negative values are shaded.

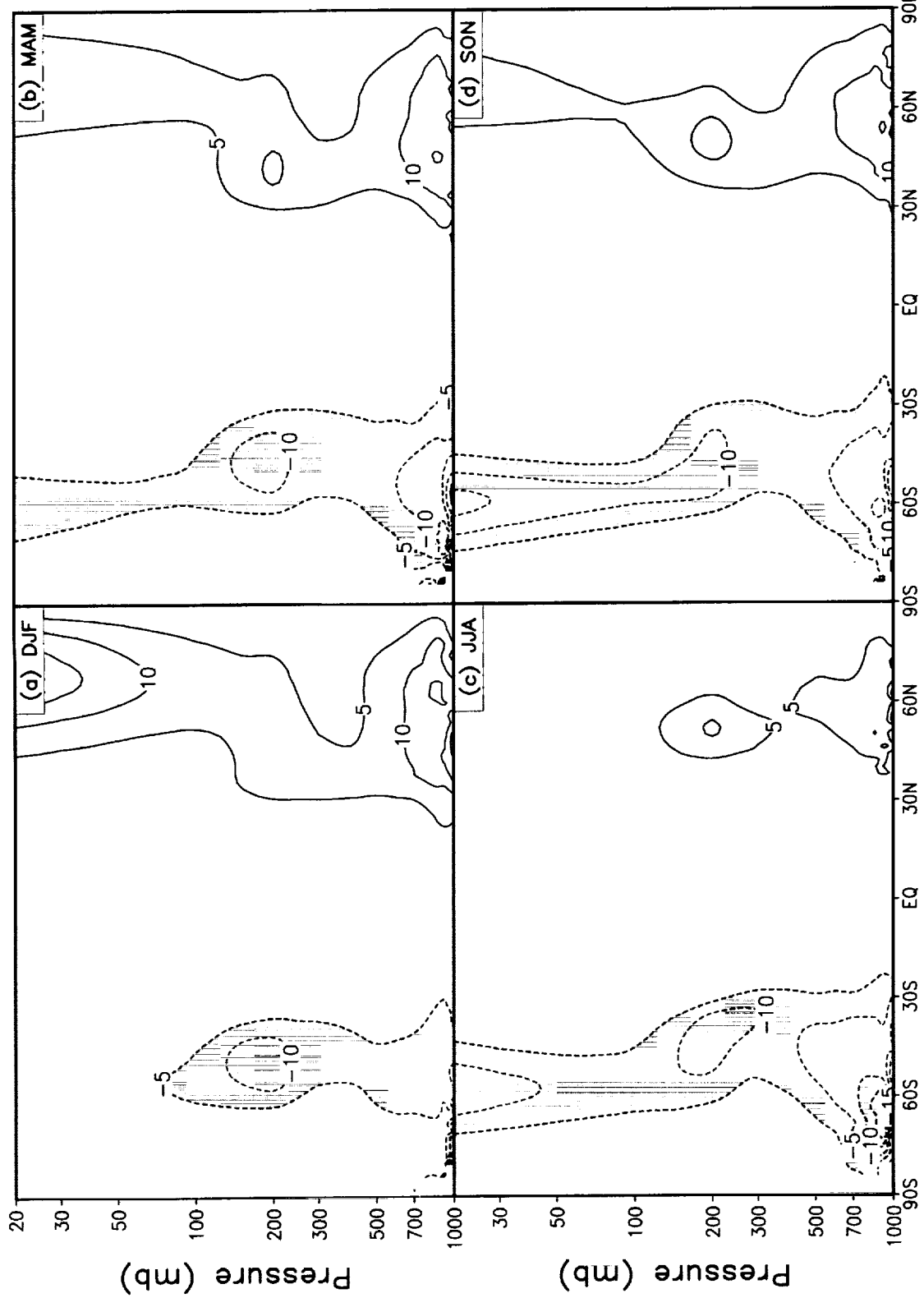

Figure 64: Zonal mean $[\overline{v't'}]$ for the model. The contour interval is 5 m s^{-1} K. Negative values are shaded.

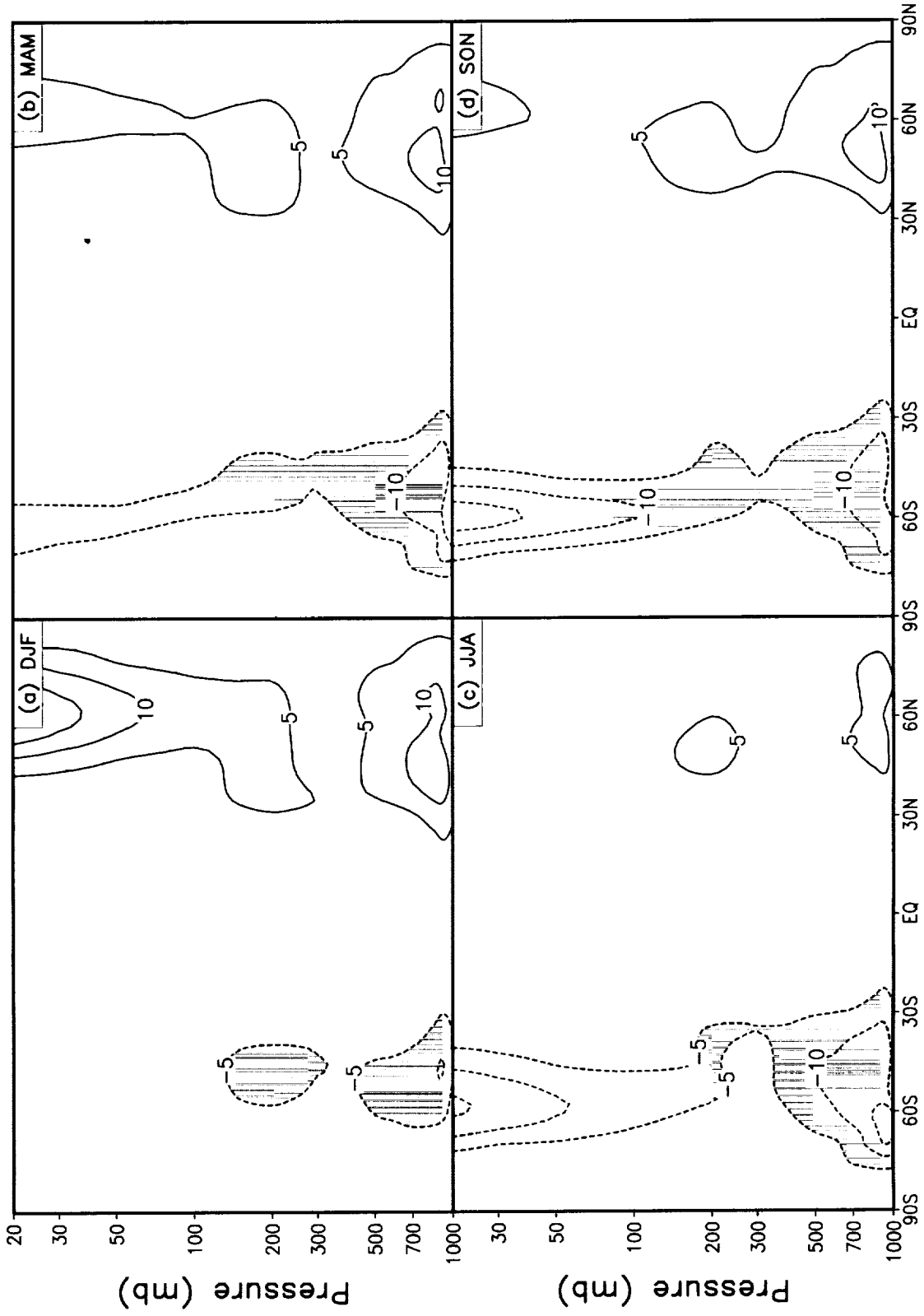

Figure 65: Zonal mean $[\overline{v't'}]$ for the reanalysis. The contour interval is 5 m s^{-1} K. Negative values are shaded.

GLOBAL MAPS OF INTRA-MONTHLY VARIABILITY

300mb height

200mb kinetic energy

200mb u'v'

850mb v'T'

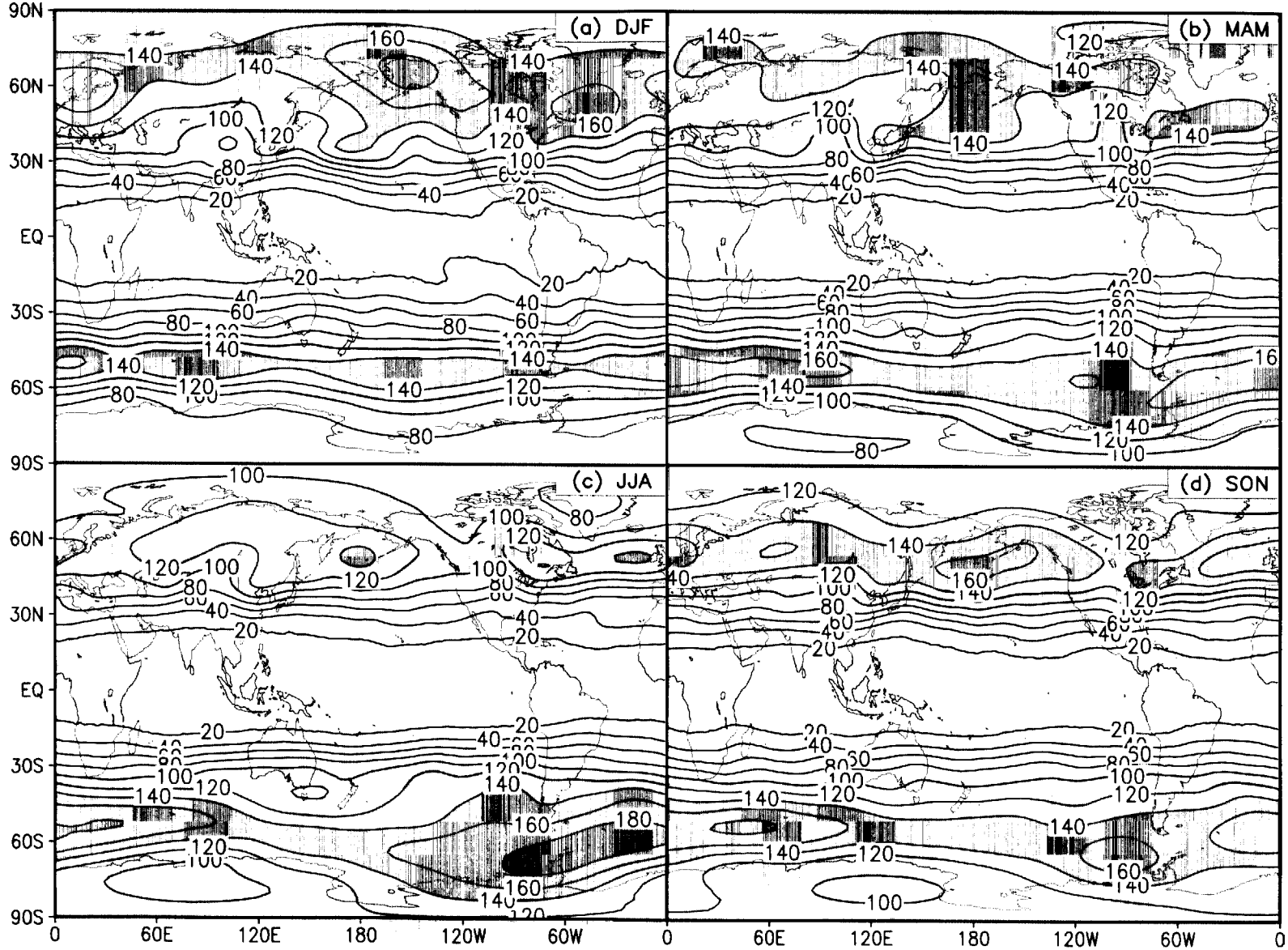

Figure 66: $\sqrt{\overline{z'z'}}$ at 300 mb for the model. The contour interval is 20 m. Values larger than 100 m are shaded.

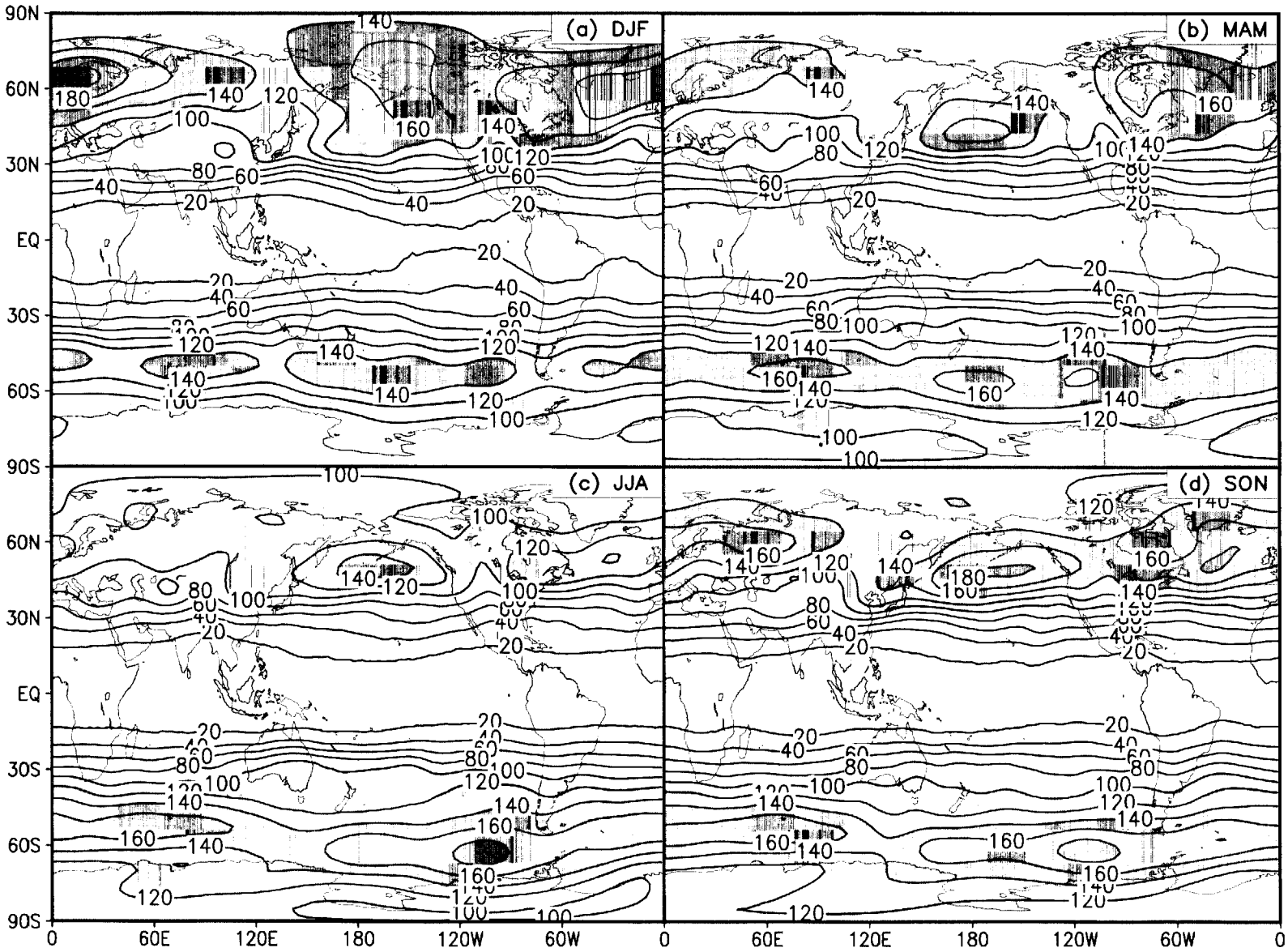

Figure 67: $\sqrt{\overline{z'z'}}$ at 300 mb for the reanalysis. The contour interval is 20 m. Values larger than 100 m are shaded.

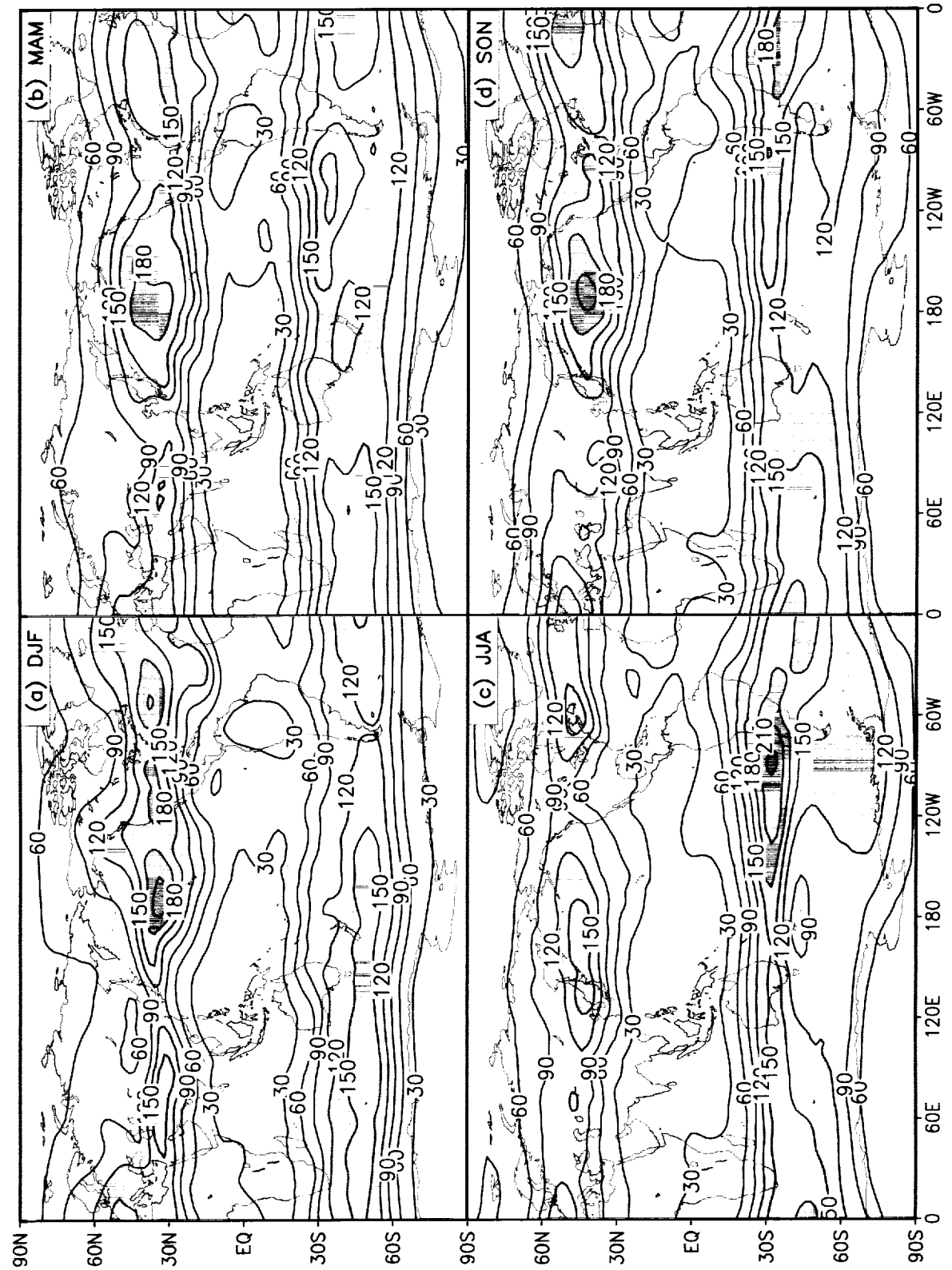

Figure 68: $\overline{(u'u' + v'v')}/2$ at 200 mb for the model. The contour interval is 30 $m^2\ s^{-2}$. Values larger than 120 $m^2\ s^{-2}$ are shaded.

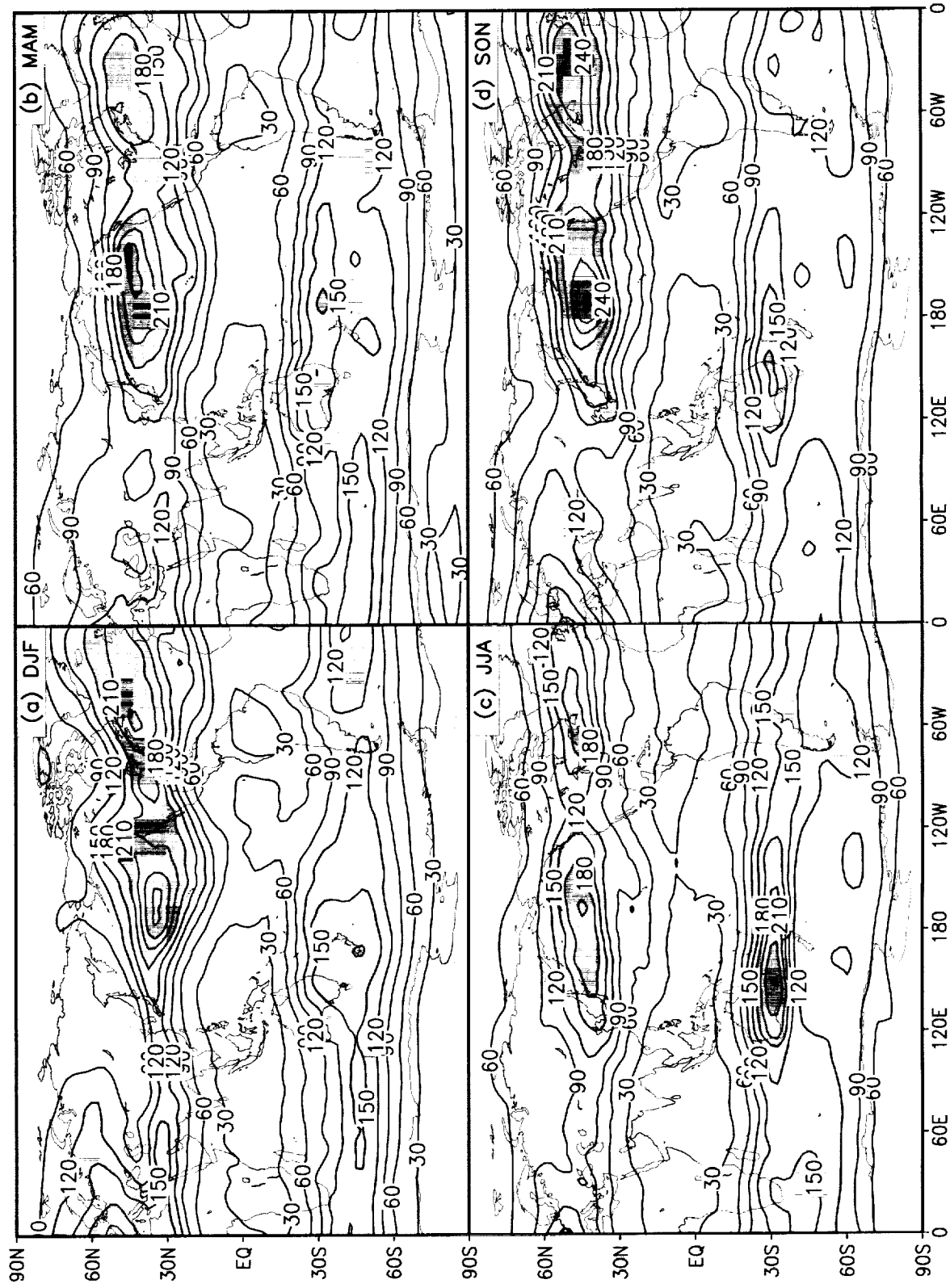

Figure 69: $\overline{(u'u' + v'v')}/2$ at 200 mb for the reanalysis. The contour interval is 30 $m^2\ s^{-2}$. Values larger than 120 $m^2\ s^{-2}$ are shaded.

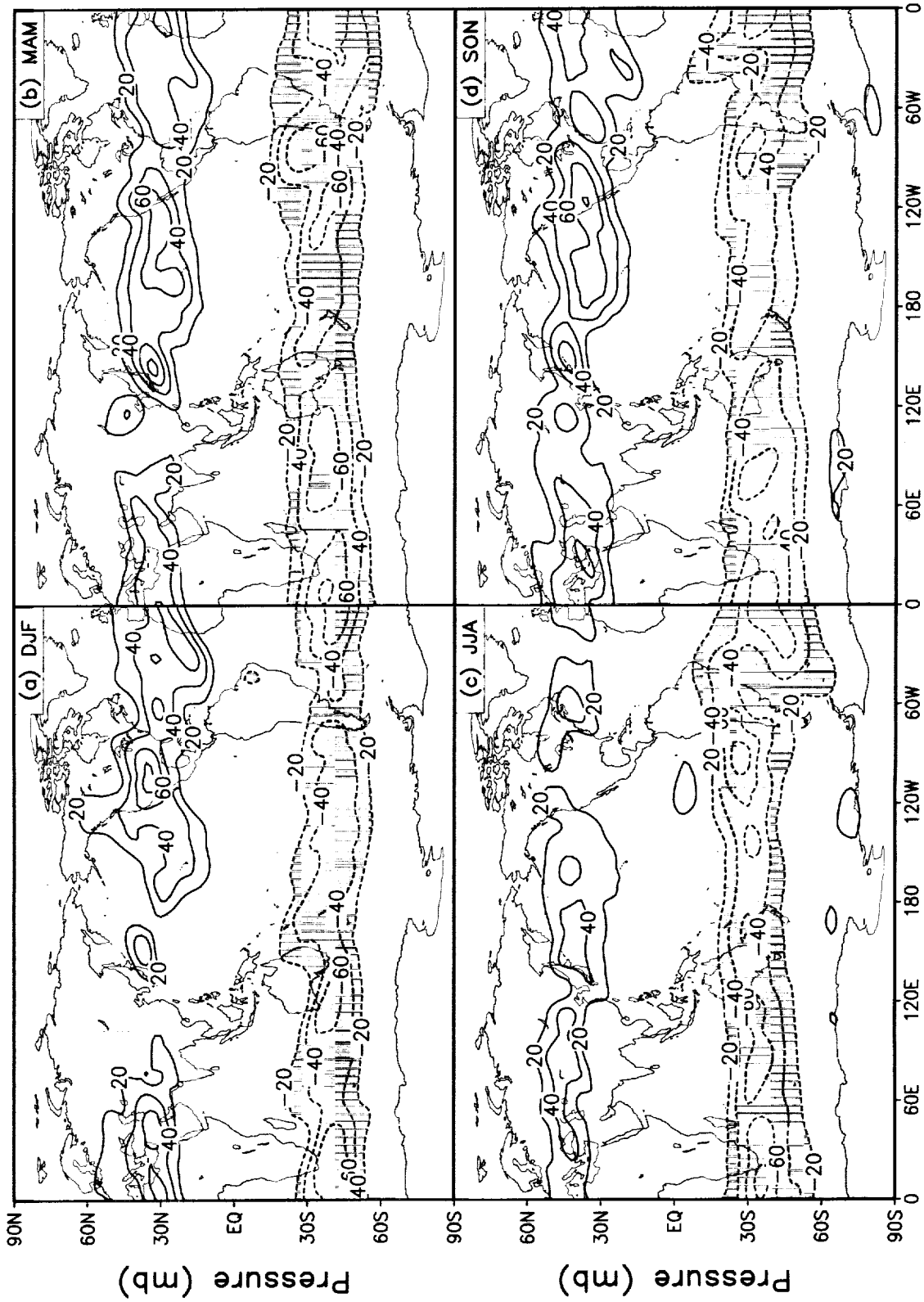

Figure 70: $\overline{u'v'}$ at 200 mb for the model. The contour interval is 20 $m^2\ s^{-2}$. Negative values are shaded.

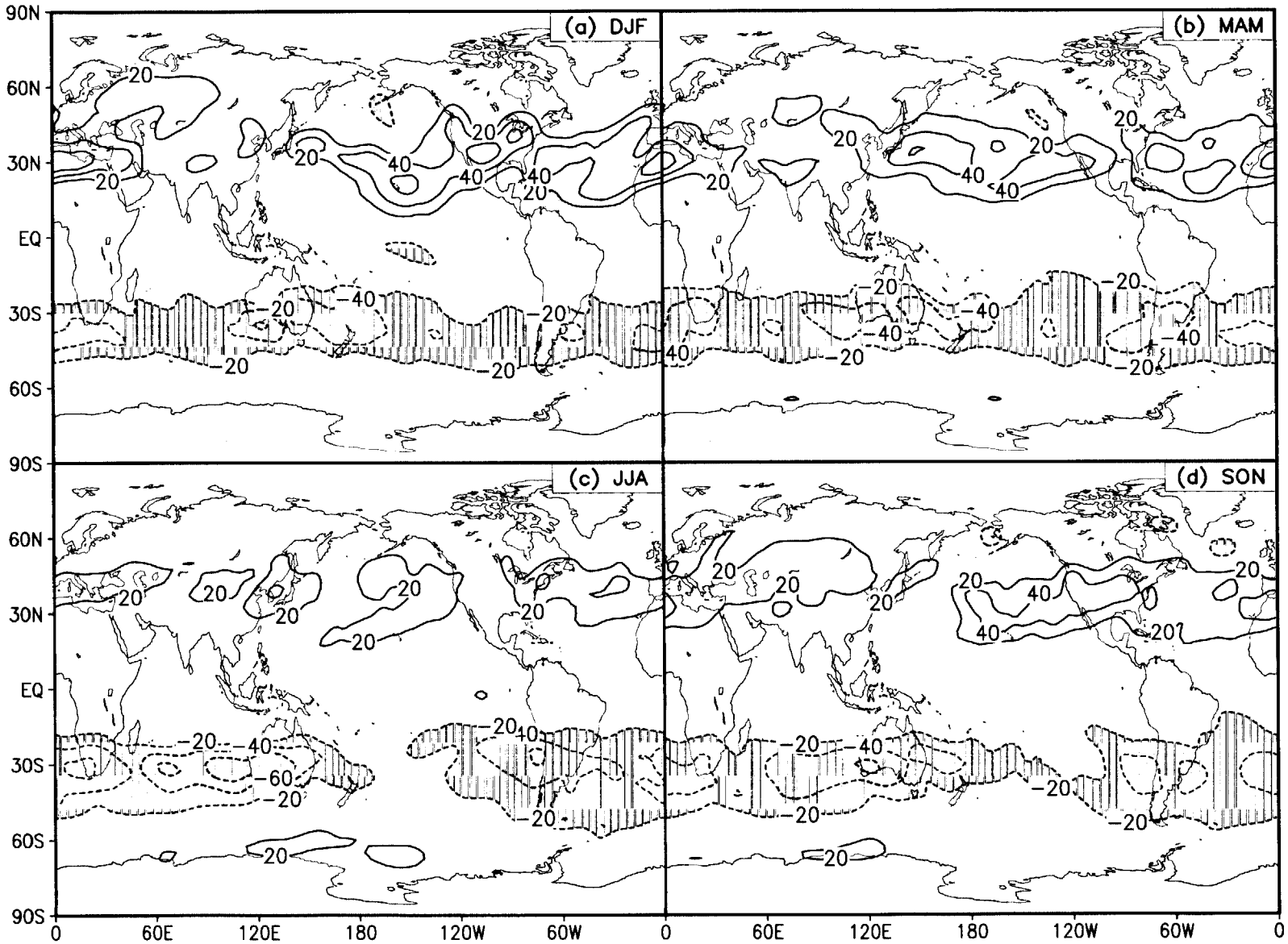

Figure 71: $\overline{u'v'}$ at 200 mb for the reanalysis. The contour interval is 20 $m^2\ s^{-2}$. Negative values are shaded.

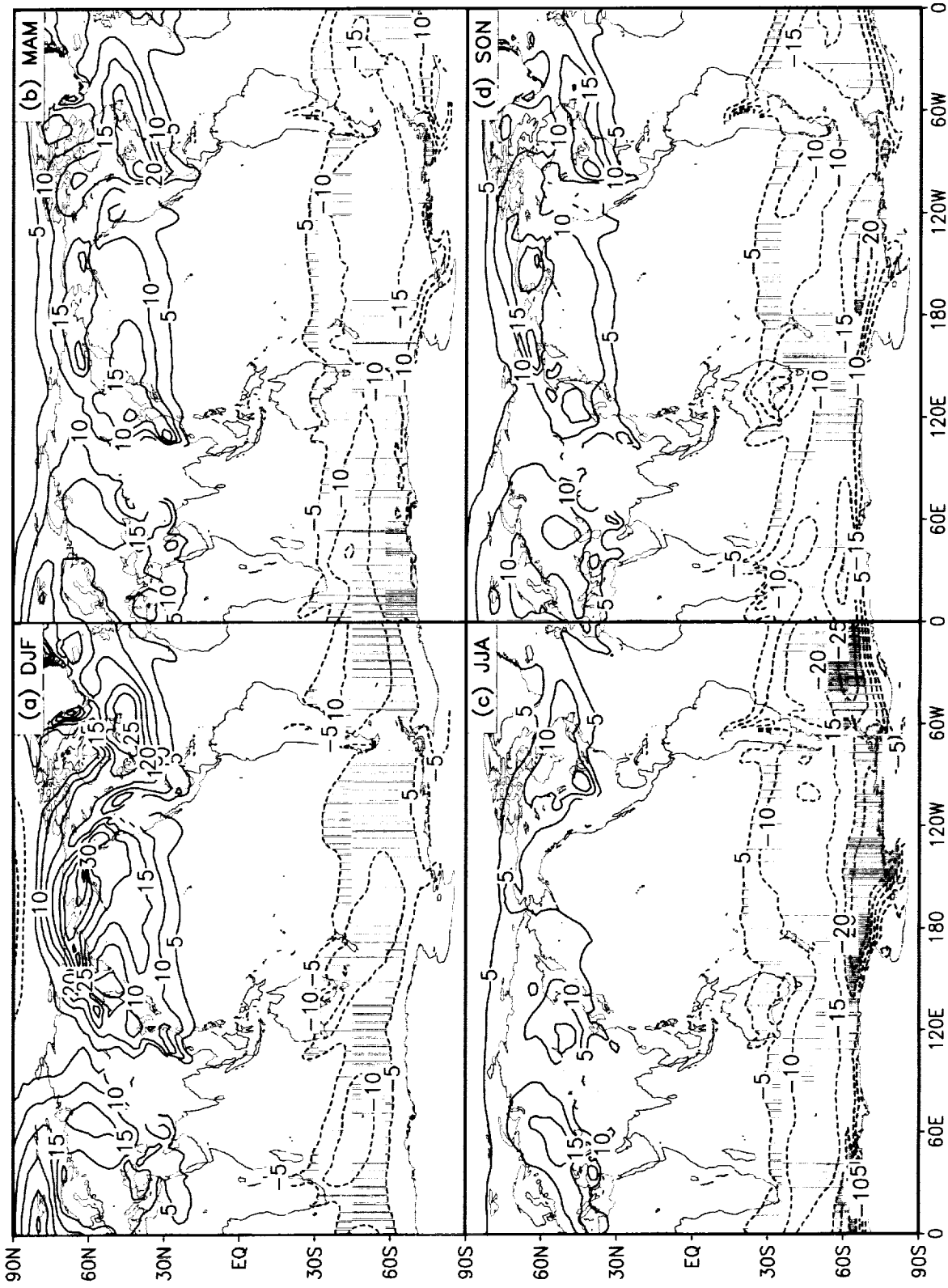

Figure 72: $\overline{v't'}$ at 850 mb for the model. The contour interval is 5 m s^{-1} K. Negative values are shaded.

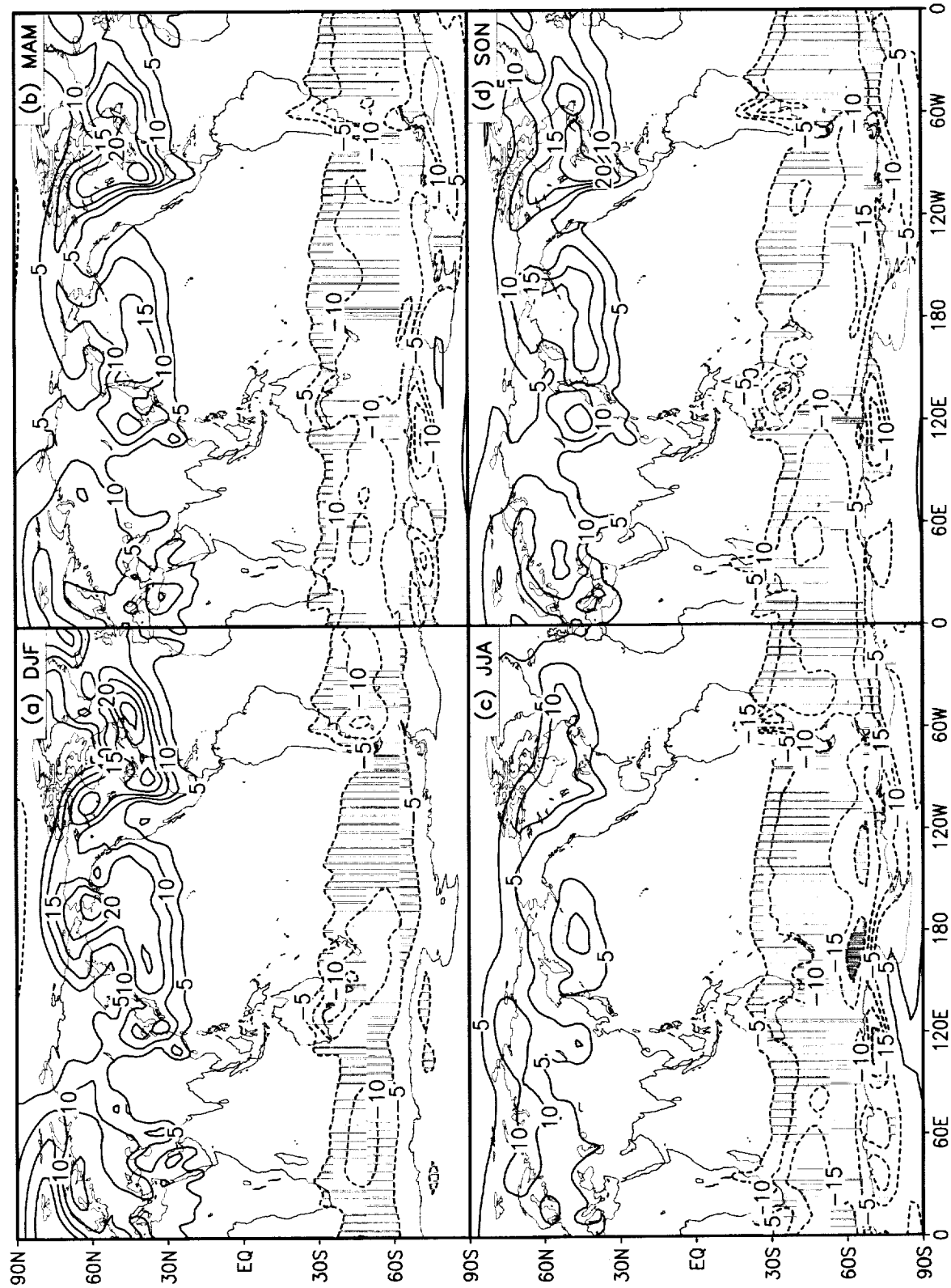

Figure 73: $\overline{v'\theta'}$ at 850 mb for the reanalysis. The contour interval is 5 m s^{-1} K. Negative values are shaded.

FILTERED INTRA-MONTHLY VARIABILITY

2.5-6 days

300mb height

200mb kinetic energy

200mb u'v'

850mb v'T'

10-30 days

300mb height

200mb kinetic energy

200mb u'v'

850mb v'T'

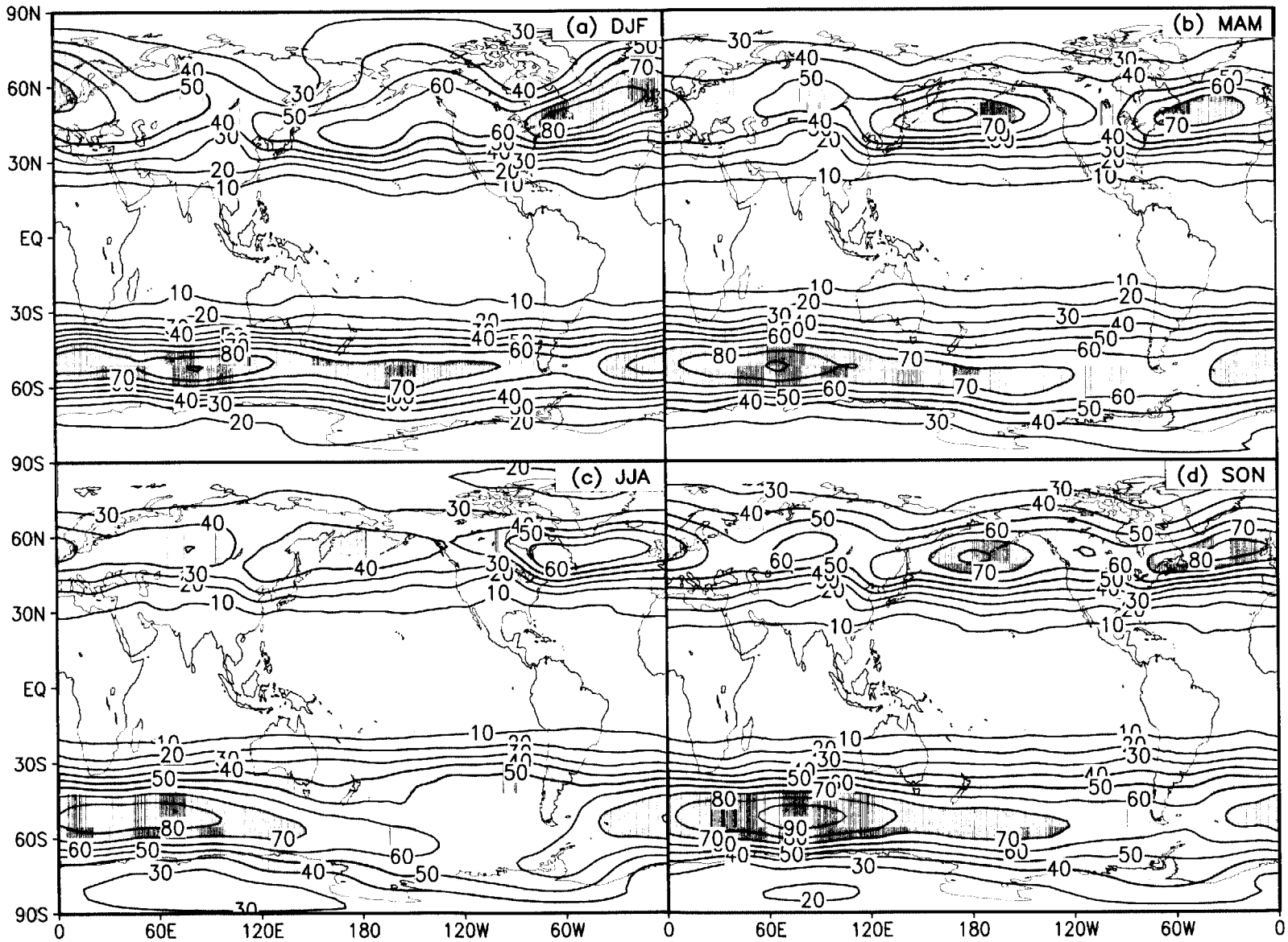

Figure 74: $\sqrt{z'z'}$ at 300 mb for the frequency ($2.5 < T < 6$ days) for the model. The contour interval is 10 m. Values larger than 40 m are shaded.

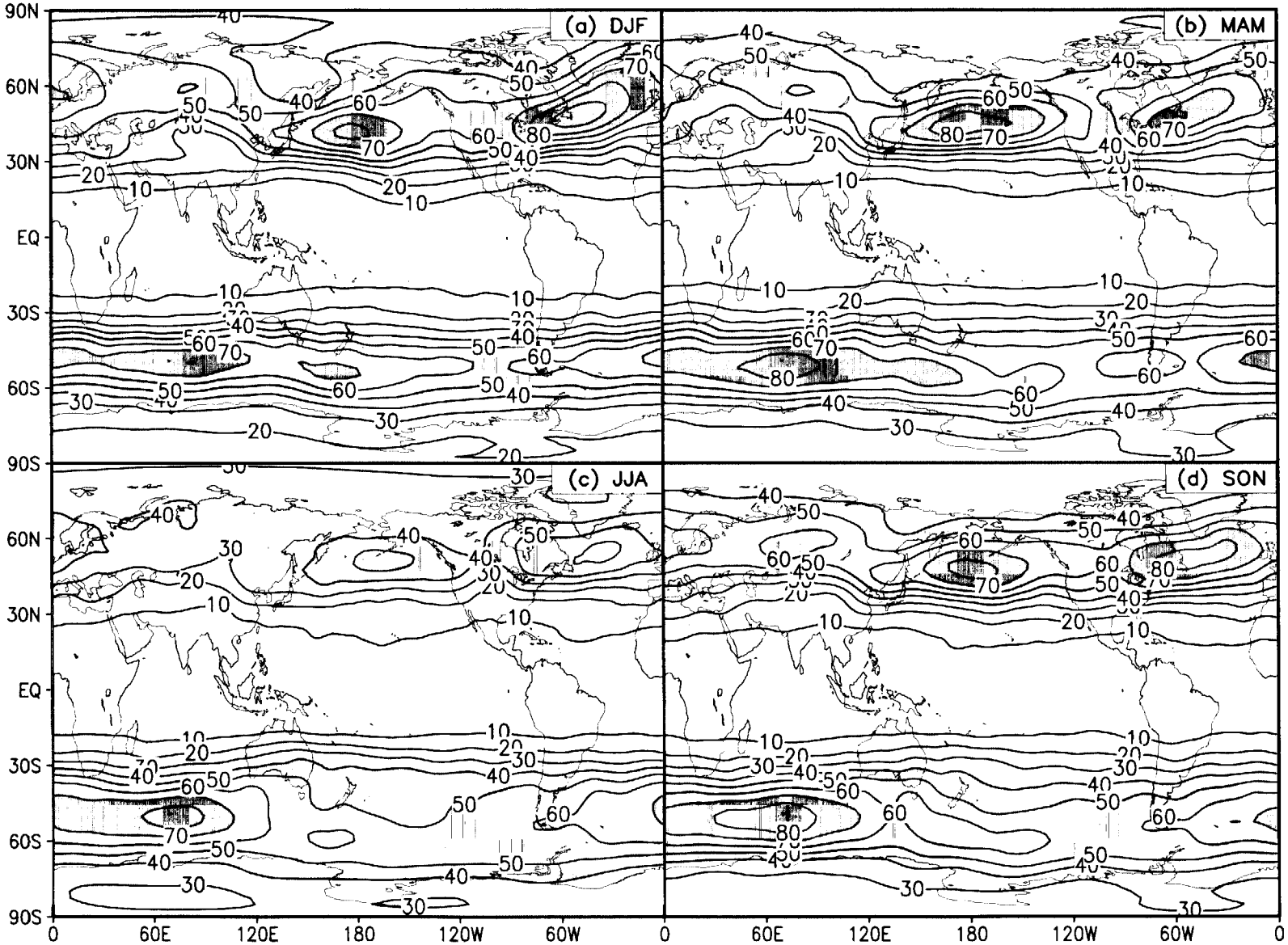

Figure 75: $\sqrt{\overline{z'z'}}$ at 300 mb for the frequency ($2.5 < T < 6$ days) for the reanalysis. The contour interval is 10 m. Values larger than 40 m are shaded.

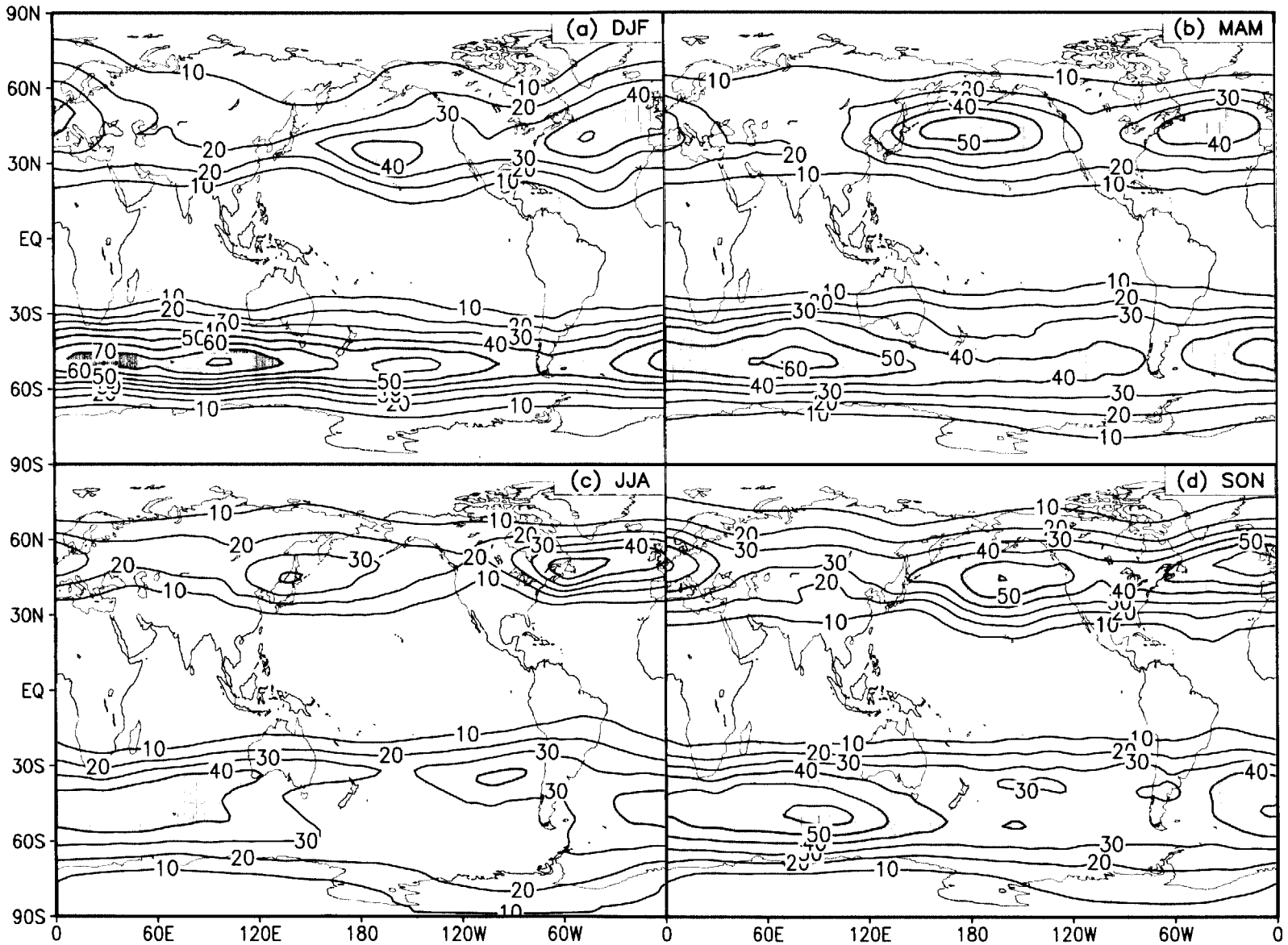

Figure 76: $\overline{(u'u' + v'v')/2}$ at 200 mb for the frequency ($2.5 < T < 6$ days) for the model. The contour interval is 10 m^2 s^{-2}. Values larger than 40 m^2 s^{-2} are shaded.

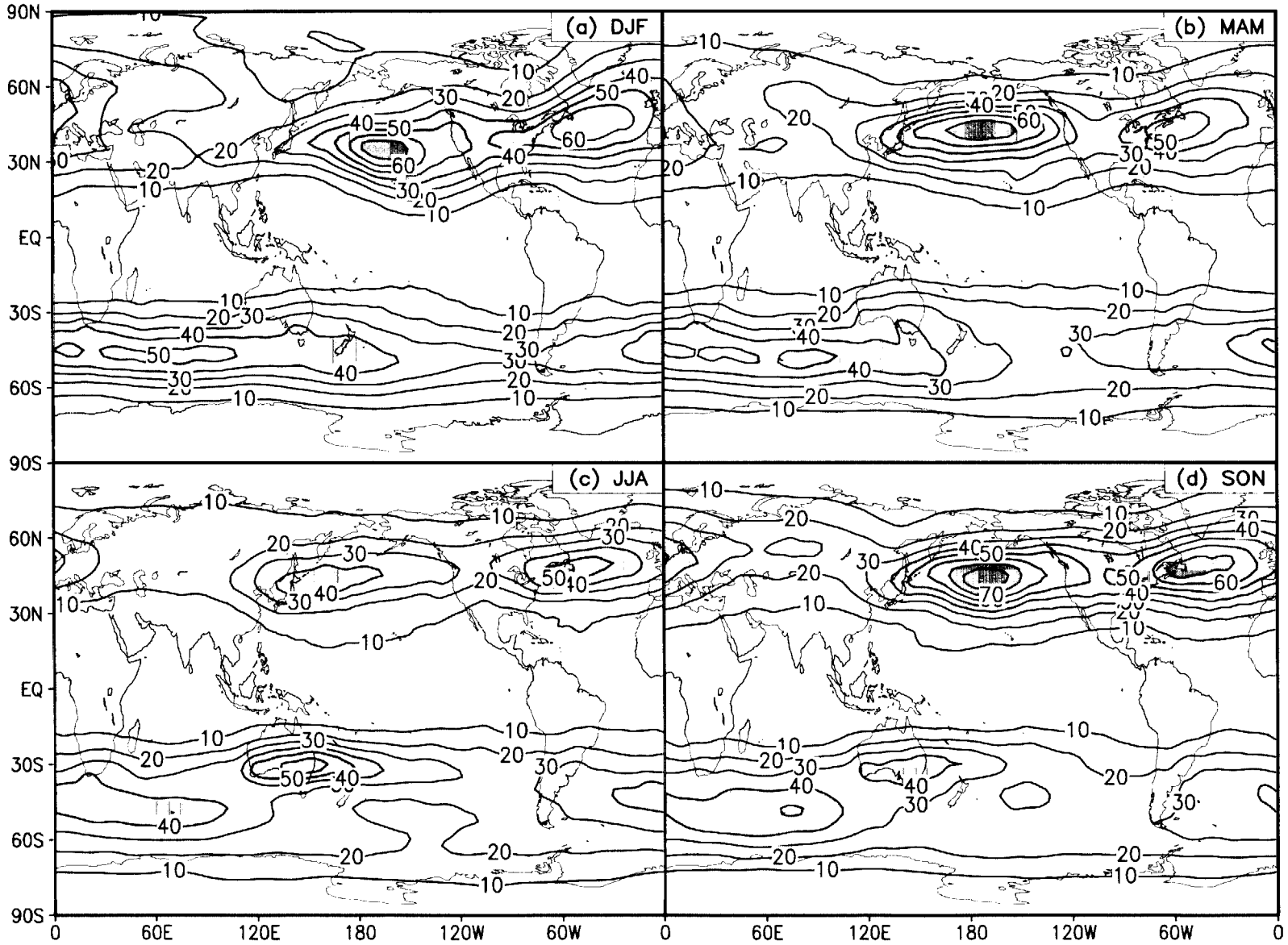

Figure 77: $\overline{(u'u' + v'v')/2}$ at 200 mb for the frequency ($2.5 < T < 6$ days) for the reanalysis. The contour interval is 10 $m^2\ s^{-2}$. Values larger than 40 $m^2\ s^{-2}$ are shaded.

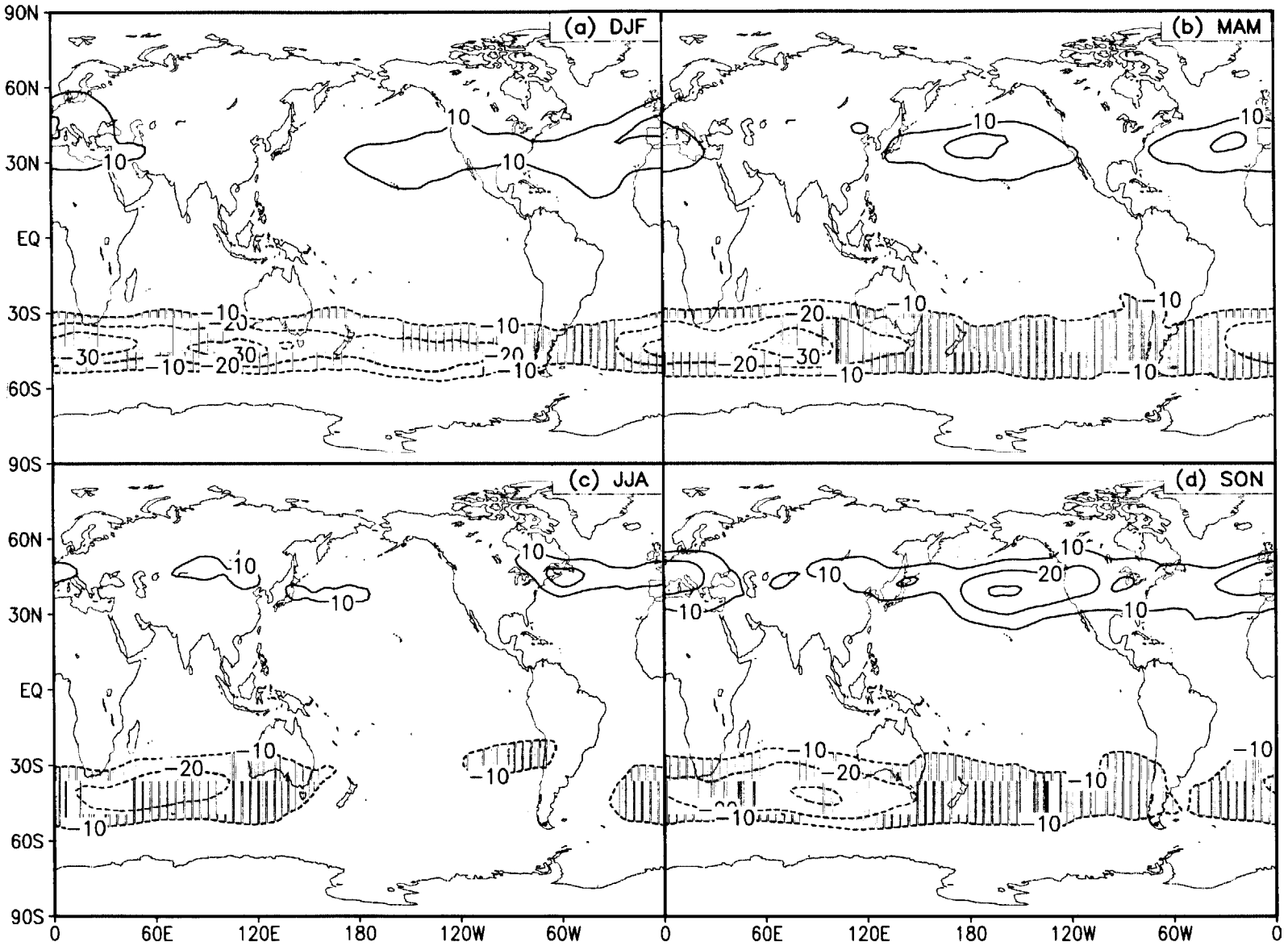

Figure 78: $\overline{u'v'}$ at 200 mb for the frequency ($2.5 < T < 6$ days) for the model. The contour interval is 10 $m^2\ s^{-2}$. Negative values are shaded.

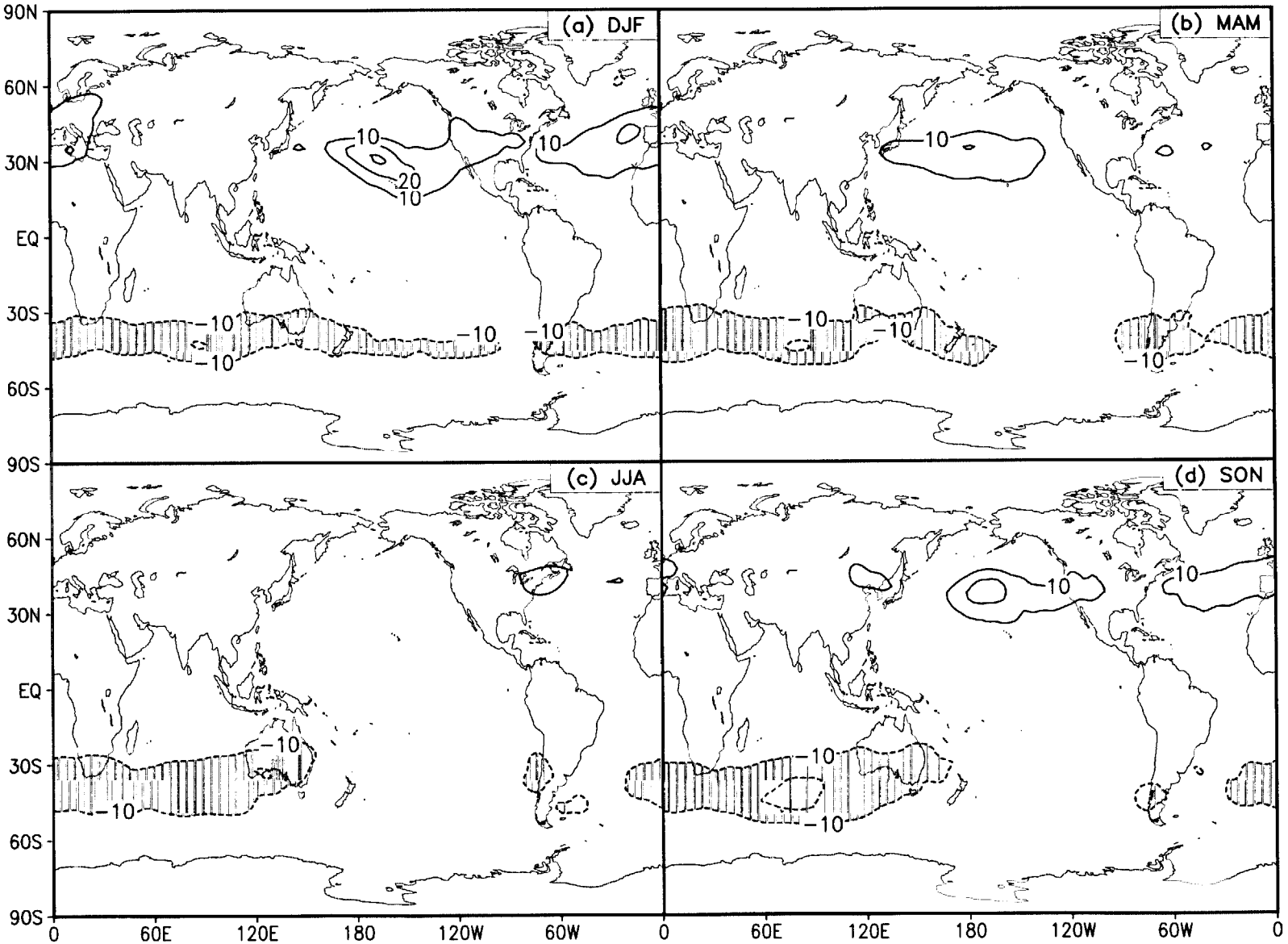

Figure 79: $\overline{u'v'}$ at 200 mb for the frequency ($2.5 < T < 6$ days) for the reanalysis. The contour interval is 10 $m^2\ s^{-2}$. Negative values are shaded.

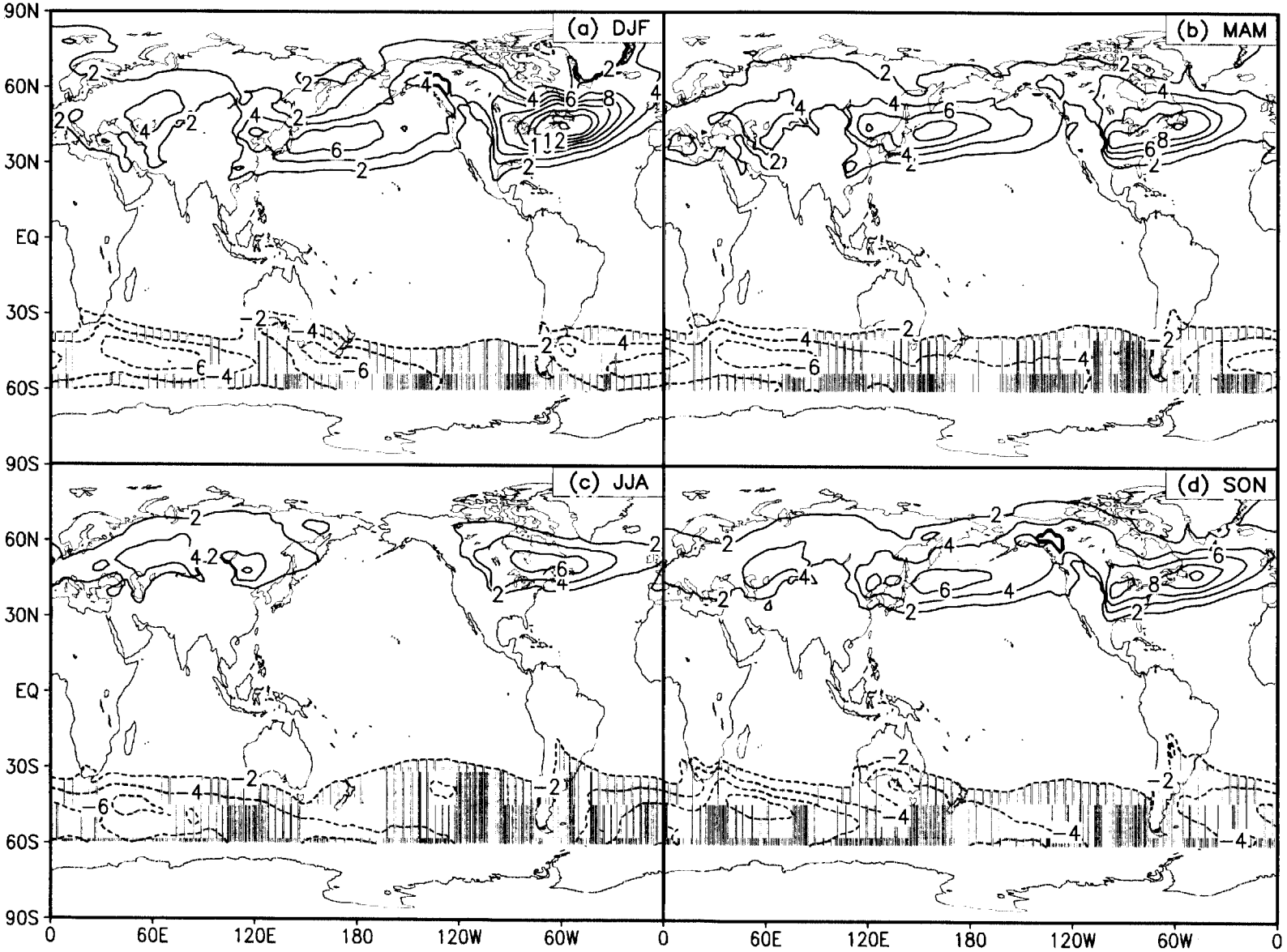

Figure 80: $\overline{v't'}$ at 850 mb for the frequency ($2.5 < T < 6$ days) for the model. The contour interval is 2 m s^{-1} K. Negative values are shaded.

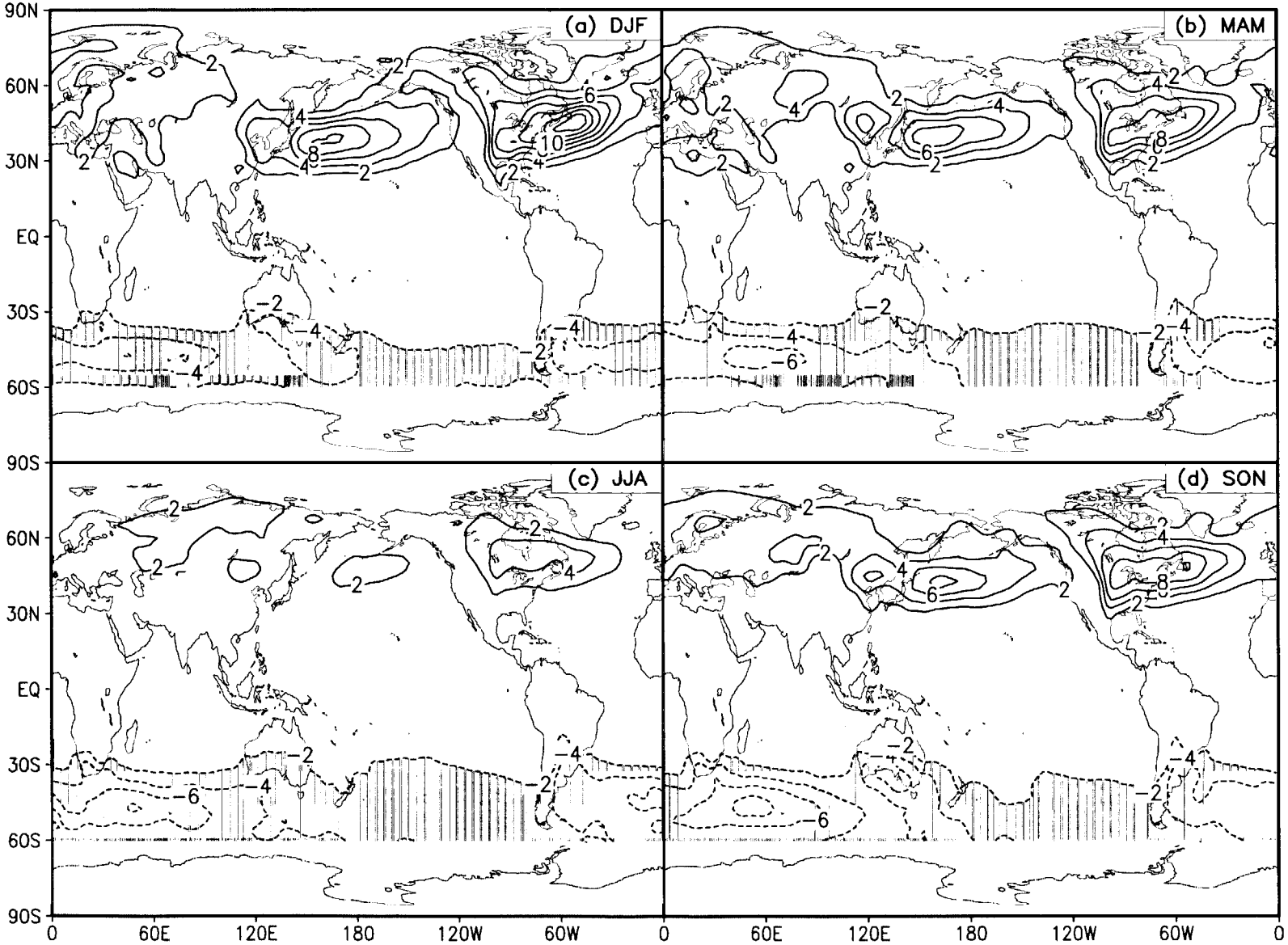

Figure 81: $\overline{v't'}$ at 850 mb for the frequency ($2.5 < T < 6$ days) for the reanalysis. The contour interval is 2 m s^{-1} K. Negative values are shaded.

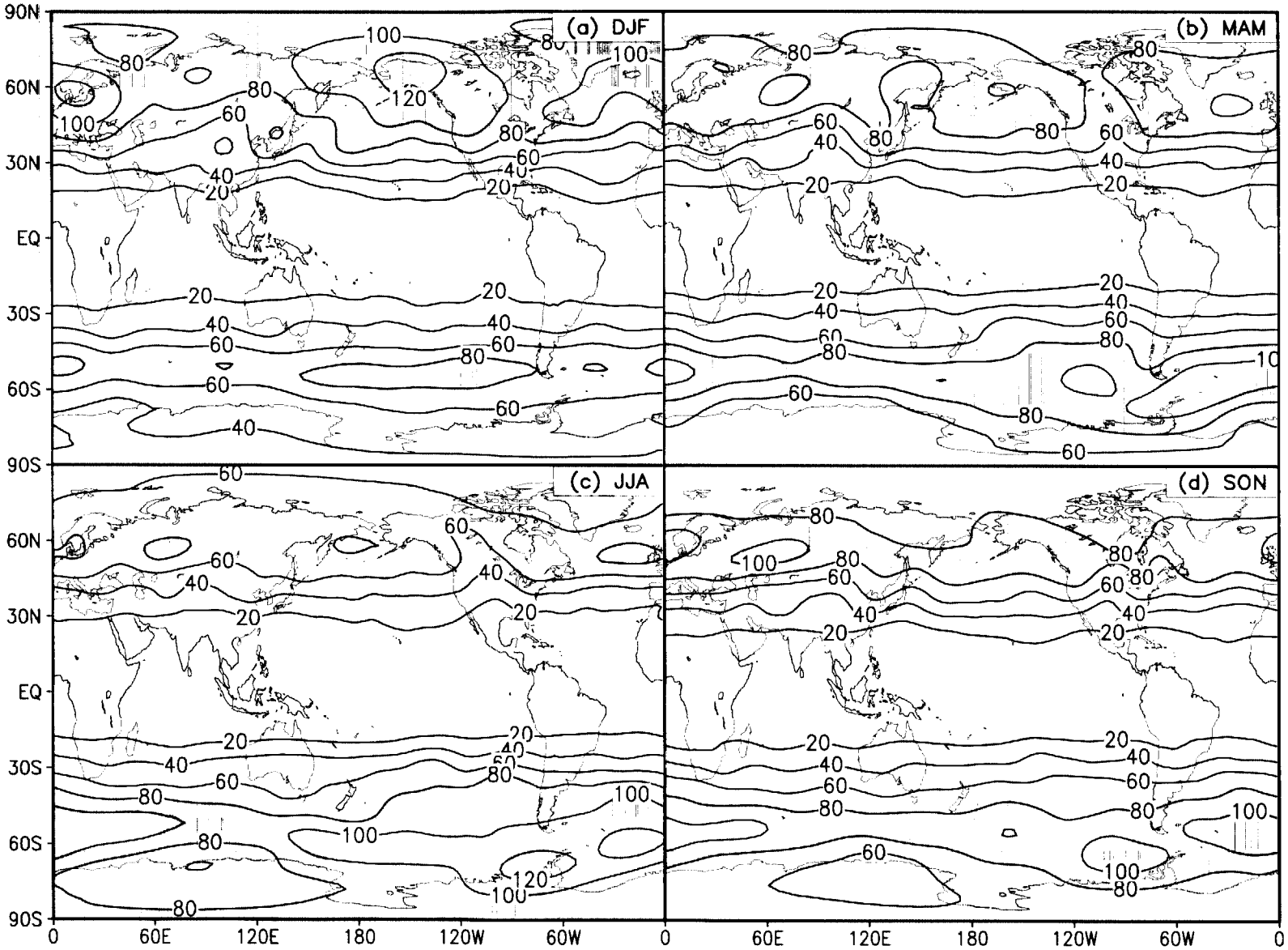

Figure 82: $\sqrt{z'z'}$ at 300 mb for the frequency ($10 < T < 30$ days) for the model. The contour interval is 20 m. Values larger than 80 m are shaded.

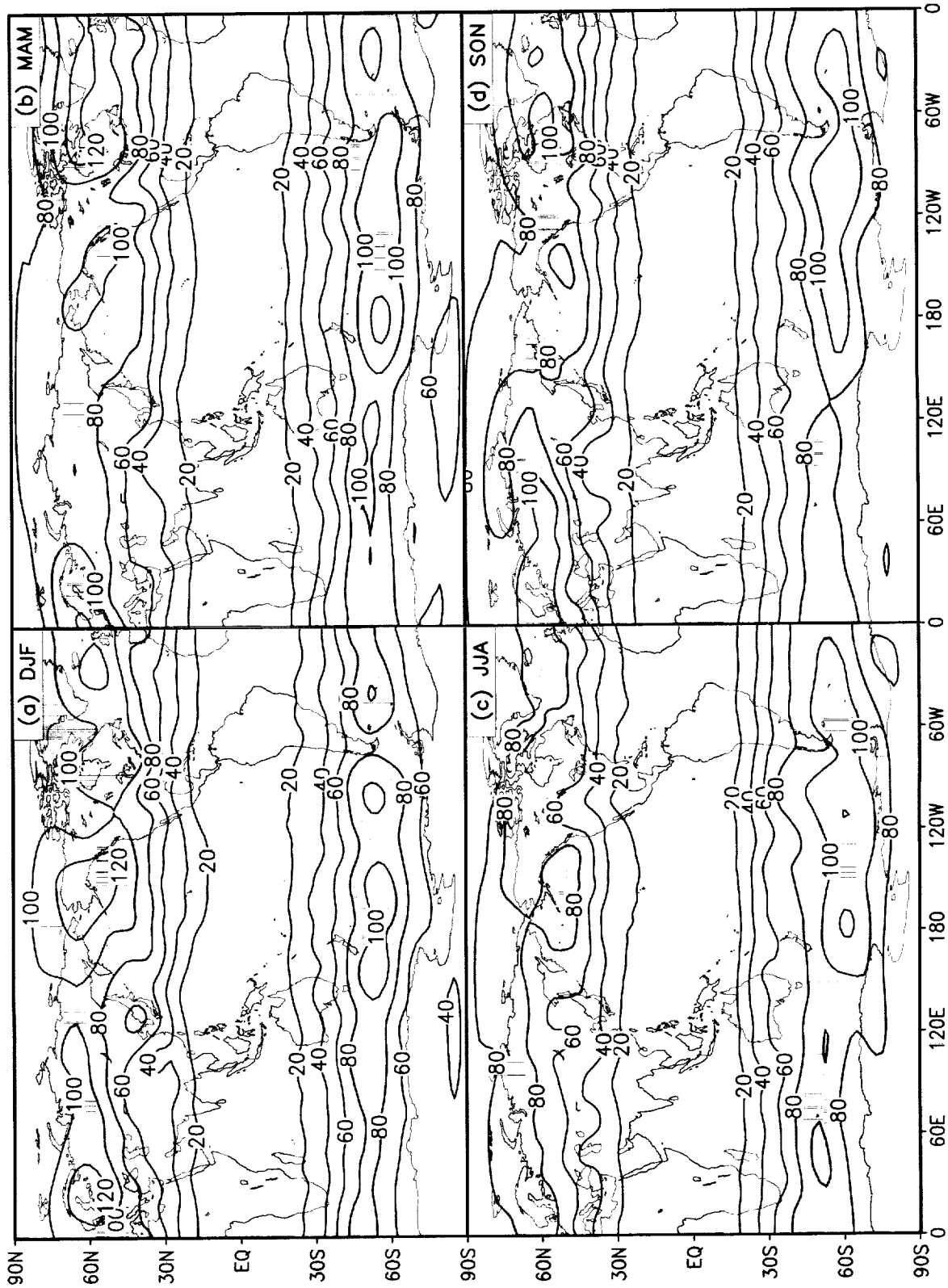

Figure 83: $\sqrt{\overline{z'z'}}$ at 300 mb for the frequency ($10 < T < 30$ days) for the reanalysis. The contour interval is 20 m. Values larger than 80 m are shaded.

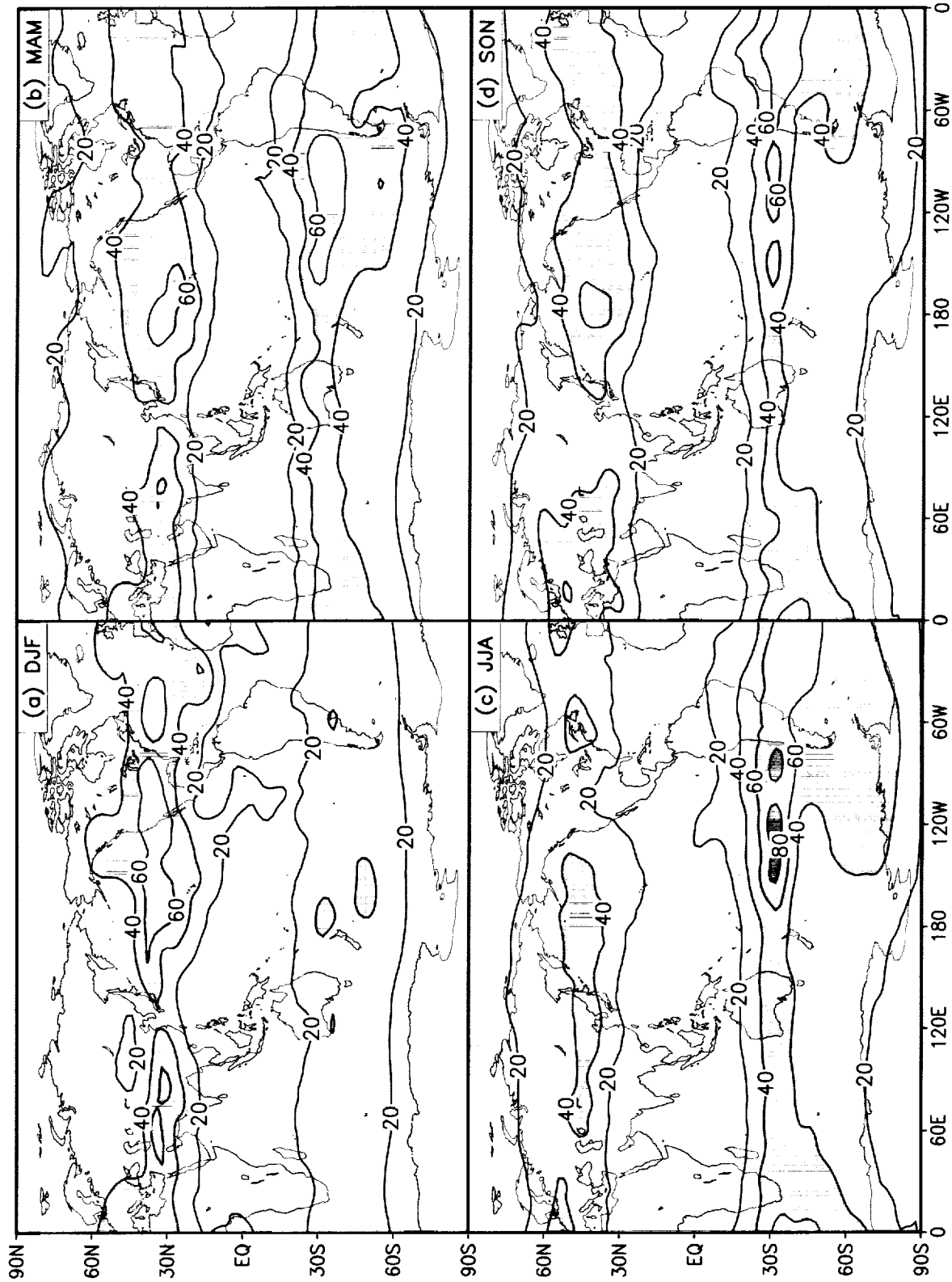

Figure 84: $\overline{(u'u' + v'v')}/2$ at 200 mb for the frequency ($10 < T < 30$ days) for the model. The contour interval is 20 m^2 s^{-2}. Values larger than 40 m^2 s^{-2} are shaded.

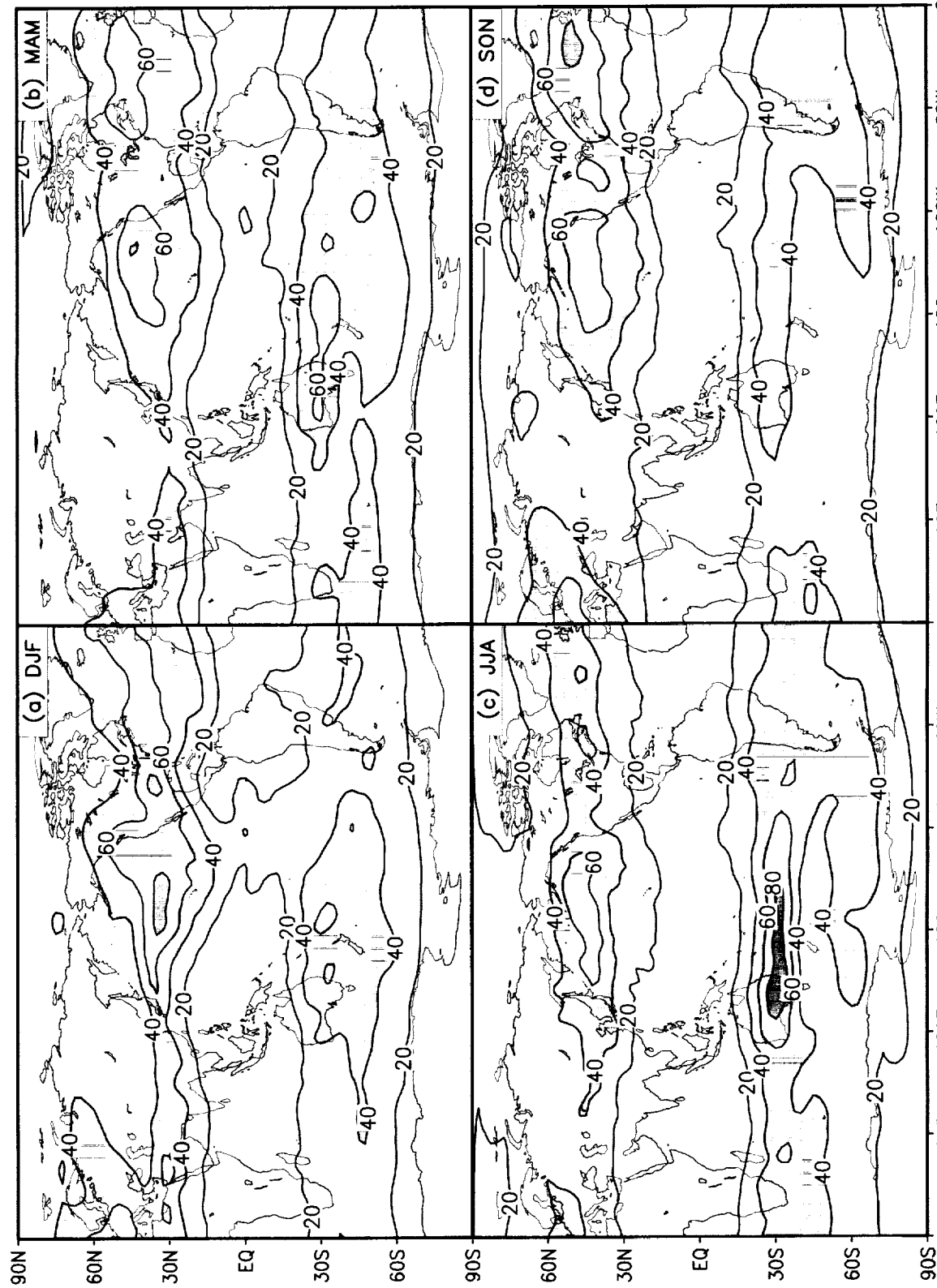

Figure 85: $\overline{(u'u' + v'v')/2}$ at 200 mb for the frequency ($10 < T < 30$ days) for the reanalysis. The contour interval is 20 $m^2\ s^{-2}$. Values larger than 40 $m^2\ s^{-2}$ are shaded.

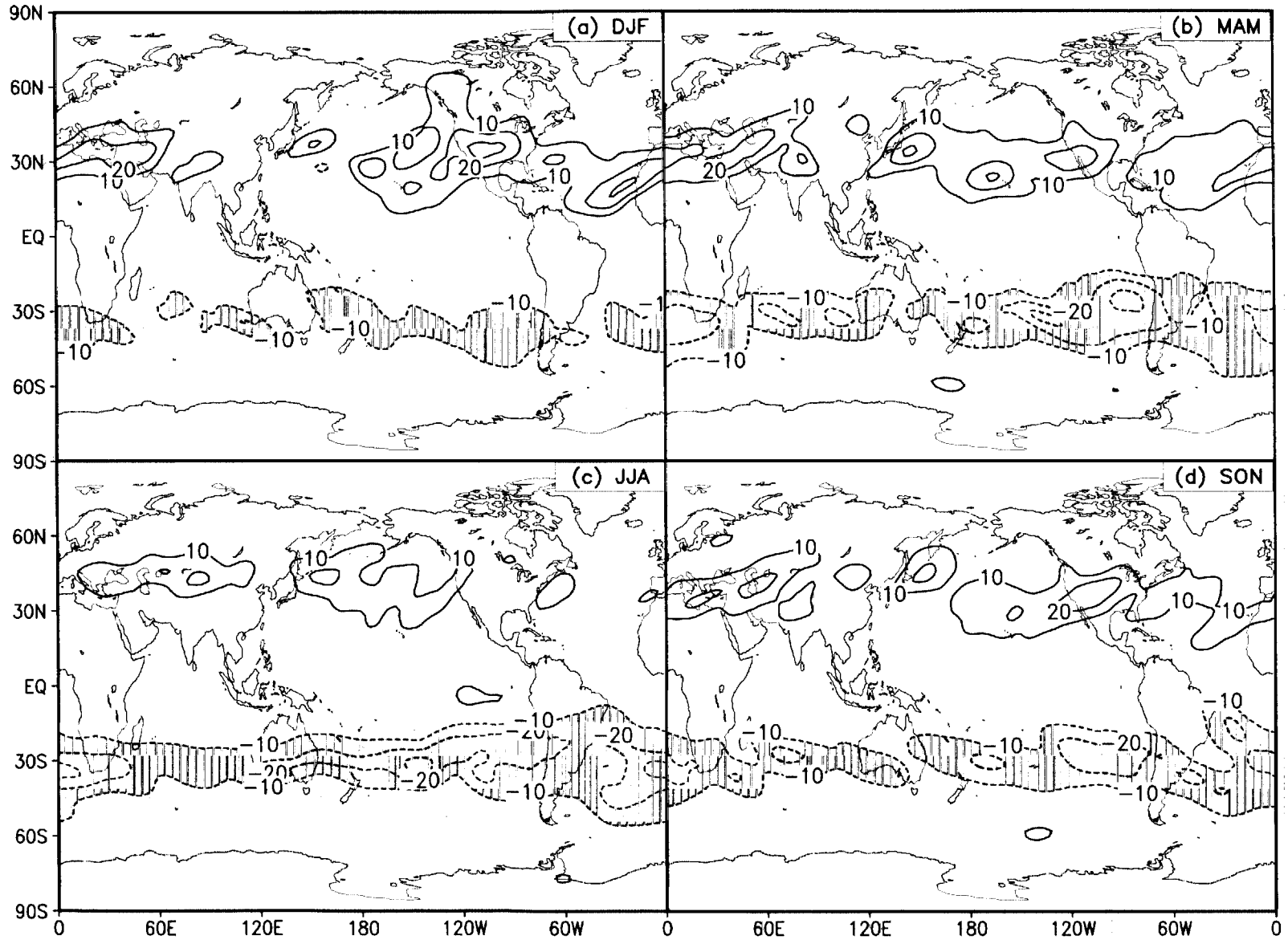

Figure 86: $\overline{u'v'}$ at 200 mb for the frequency ($10 < T < 30$ days) for the model. The contour interval is 10 m^2 s^{-2}. Negative values are shaded.

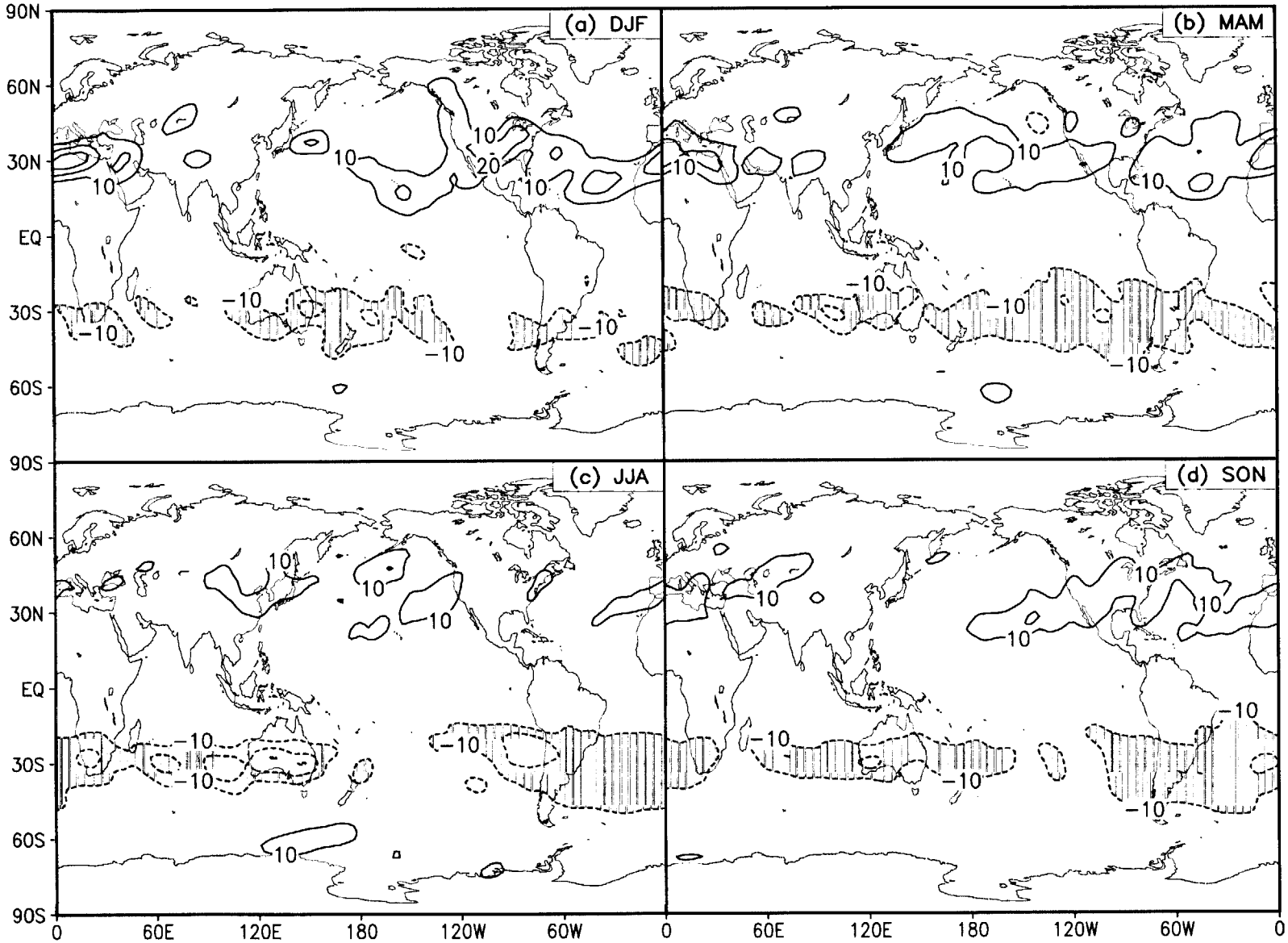

Figure 87: $\overline{u'v'}$ at 200 mb for the frequency ($10 < T < 30$ days) for the reanalysis. The contour interval is 10 $m^2\ s^{-2}$. Negative values are shaded.

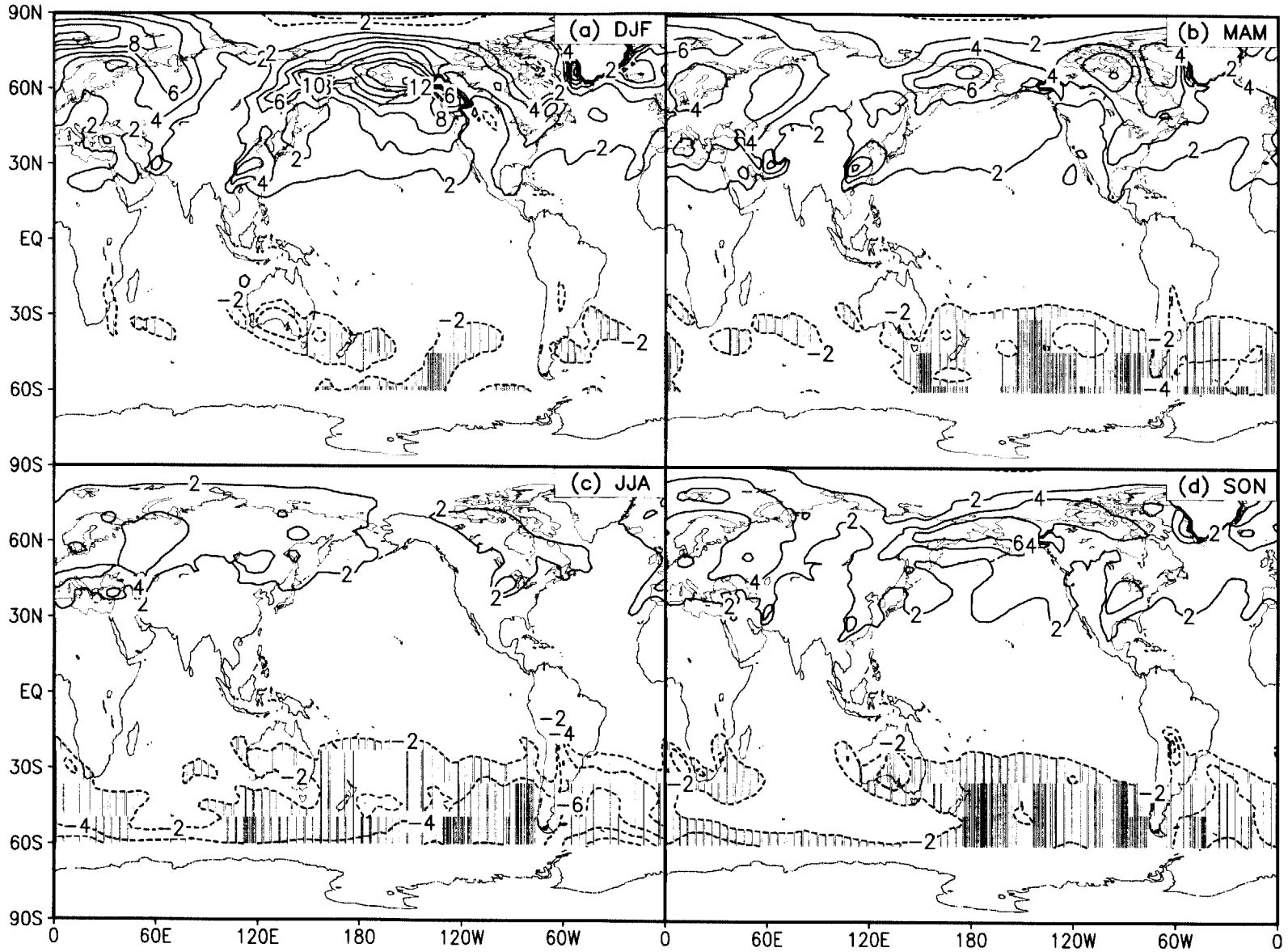

Figure 88: $\overline{v't'}$ at 850 mb for the frequency ($10 < T < 30$ days) for the model. The contour interval is 2 m s^{-1} K. Negative values are shaded.

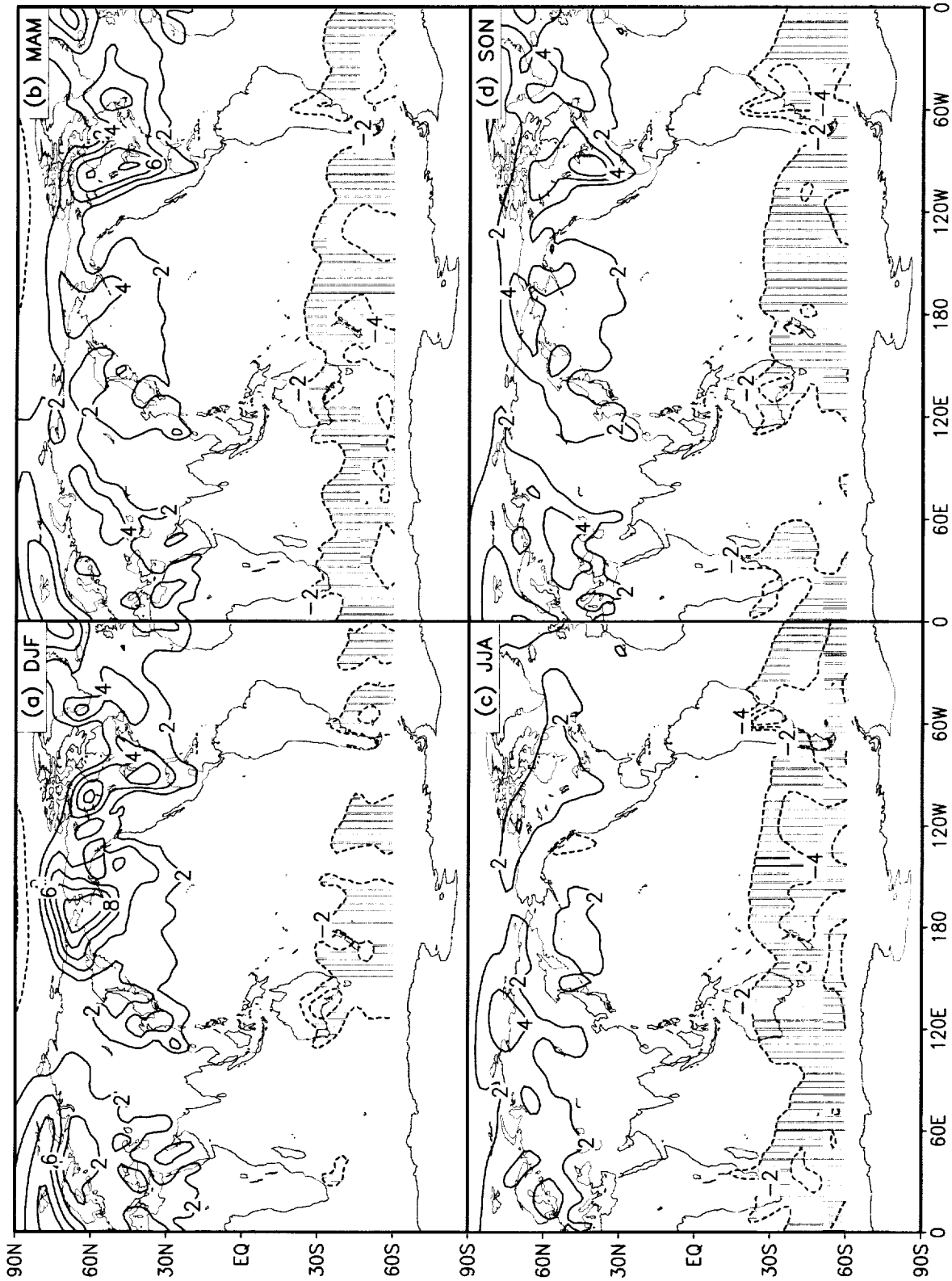

Figure 89: $\overline{v't'}$ at 850 mb for the frequency ($10 < T < 30$ days) for the reanalysis. The contour interval is 2 m s^{-1} K. Negative values are shaded.

THE MADDEN-JULIAN OSCILLATION

200mb Velocity Potential Variance (20-90 days)

CEOF 1 (20-90 day 200mb Velocity Potential)

Wavelet Decomposition of CEOF 1

Composite 200mb Velocity Potential and OLR

Composite 200mb Velocity Potential and TPW

Composite 200mb Stream Function and OLR

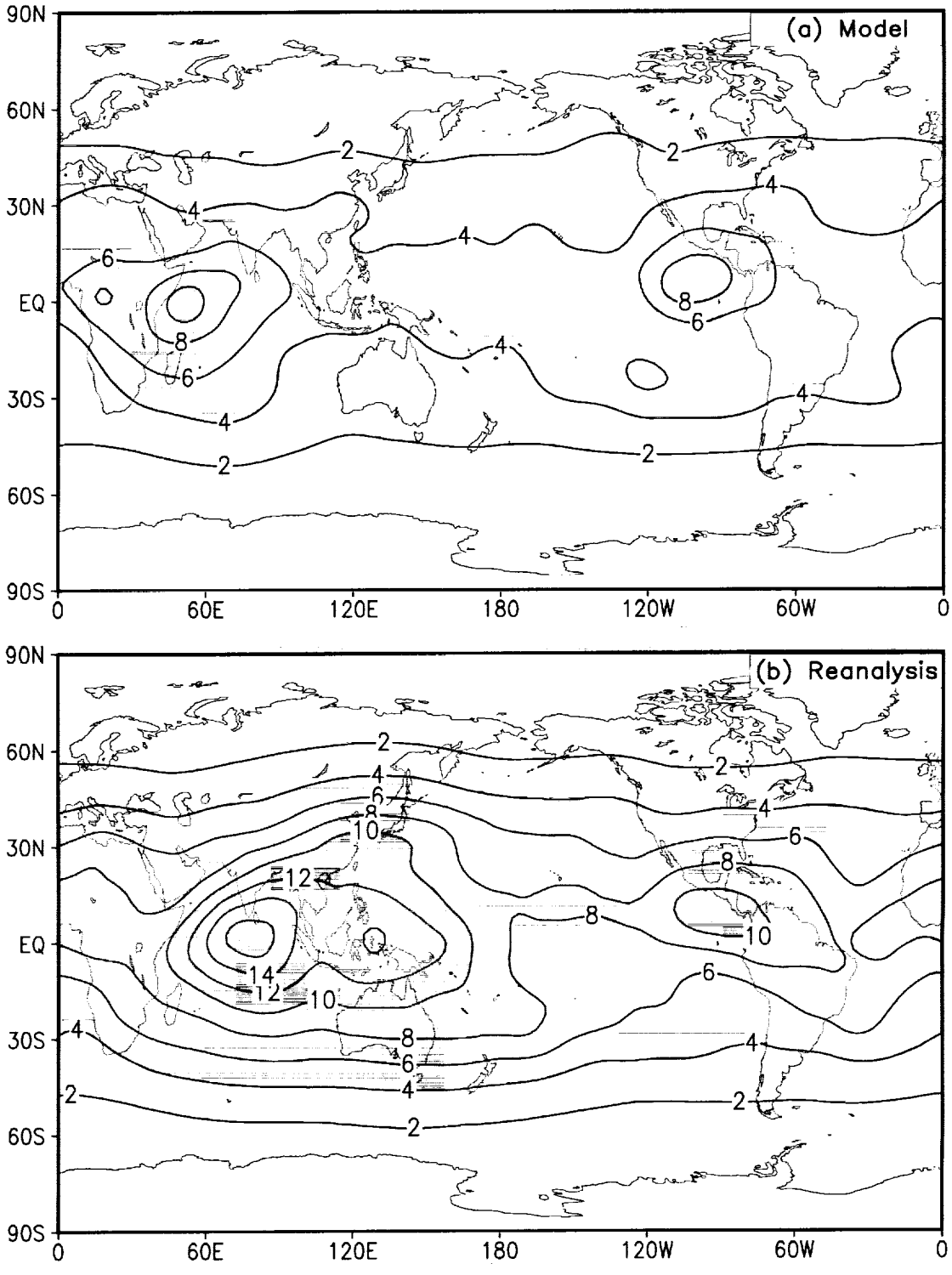

Figure 90: 200 mb velocity potential variances (20-90 days) a) for the model, b) for the reanalysis. The contour interval is 2×10^{12} m^4 s^{-2}. Values larger than 4×10^{12} m^4 s^{-2} are shaded.

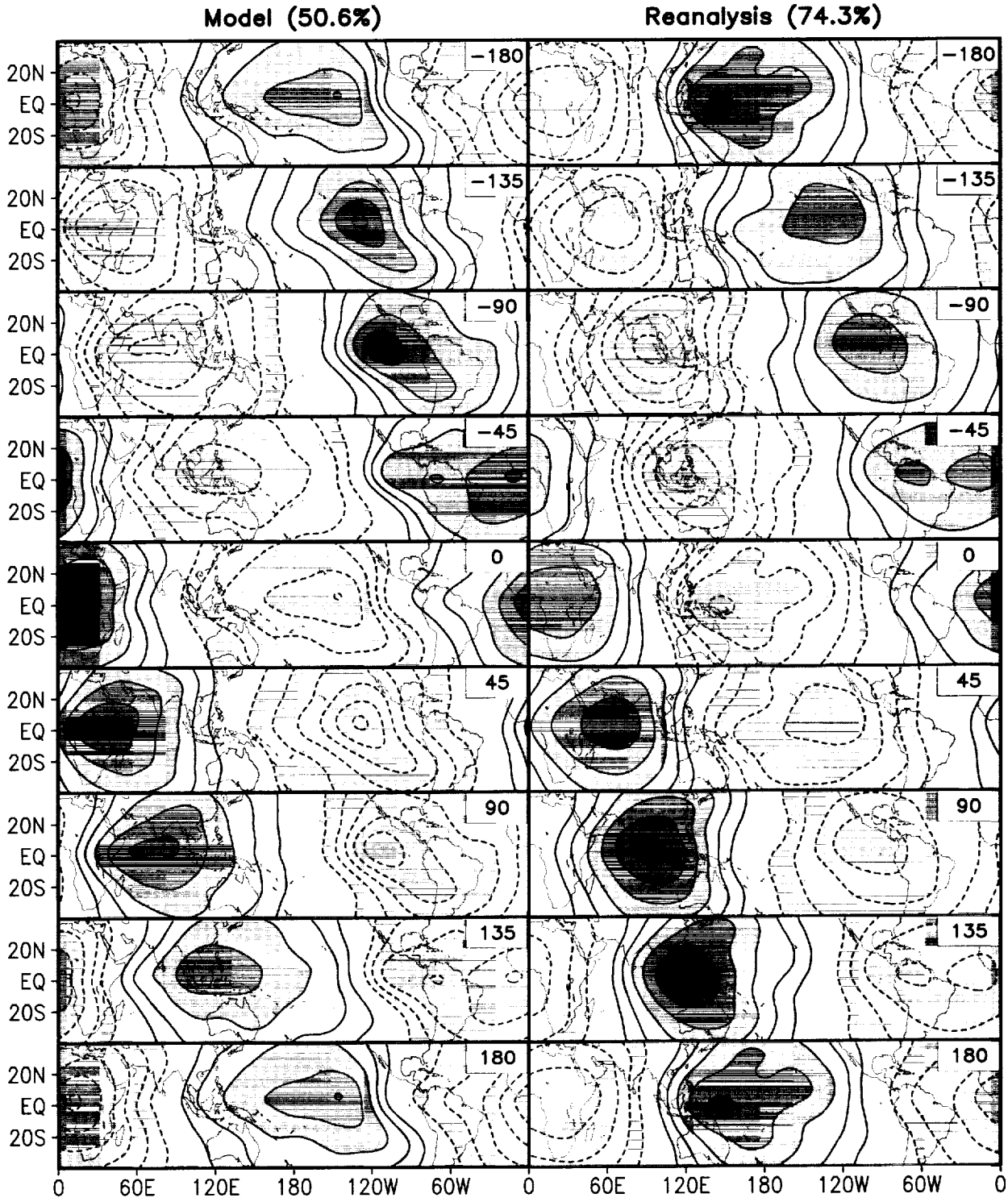

Figure 91: The first complex EOF of the 200 mb velocity potential filed from the model (left panels) and the reanalysis (right panels). The numbers in ther upper right correspond to the phase angle. Negative values are dashed.

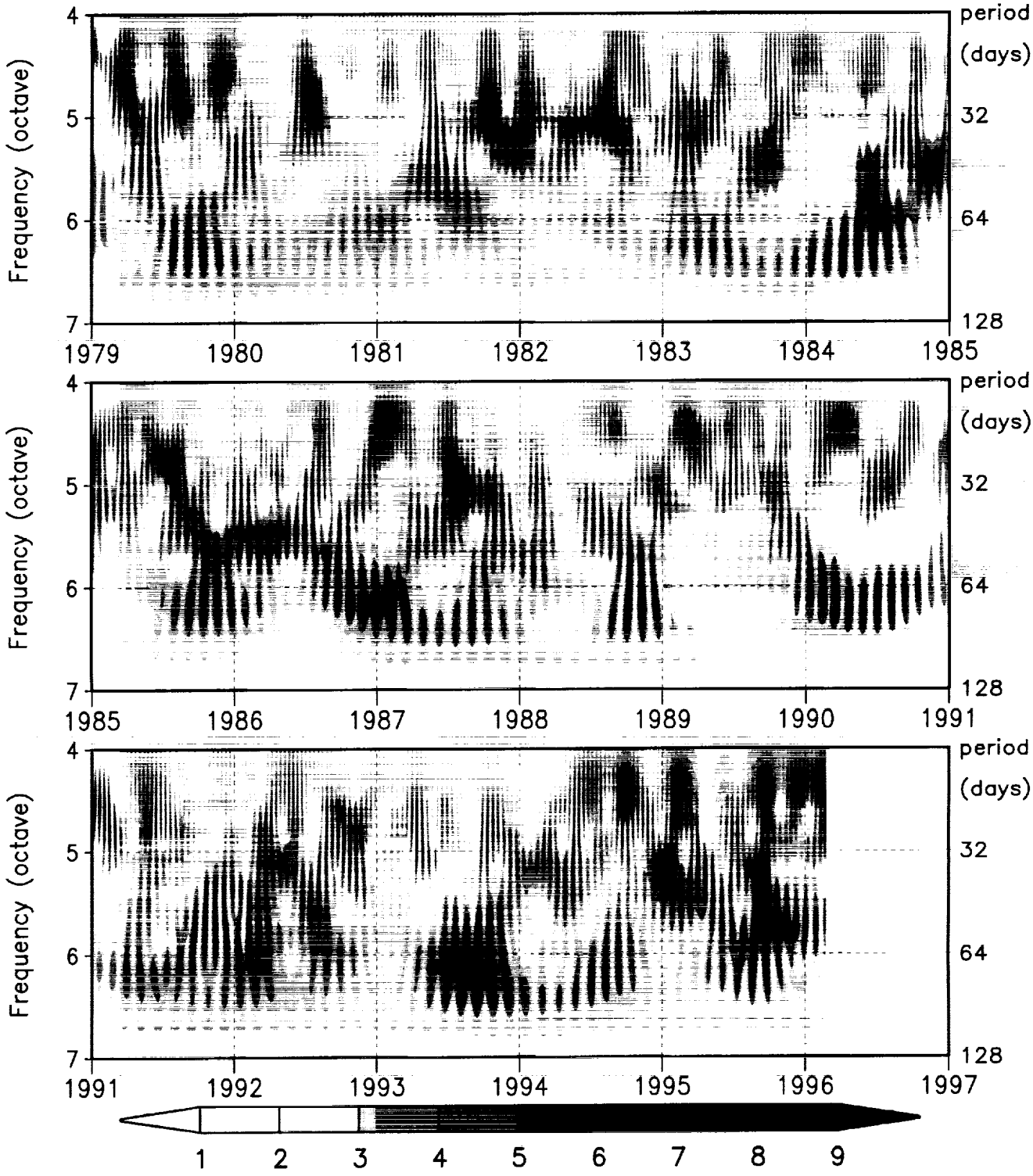

Figure 92: Time-frequency representation of the modulus of the the complex Morlet wavelet coefficients based on the first complex EOF of the 200 mb velocity potential filed from the model. The left ordinate is frequency in octive, and the right ordinate is period in day.

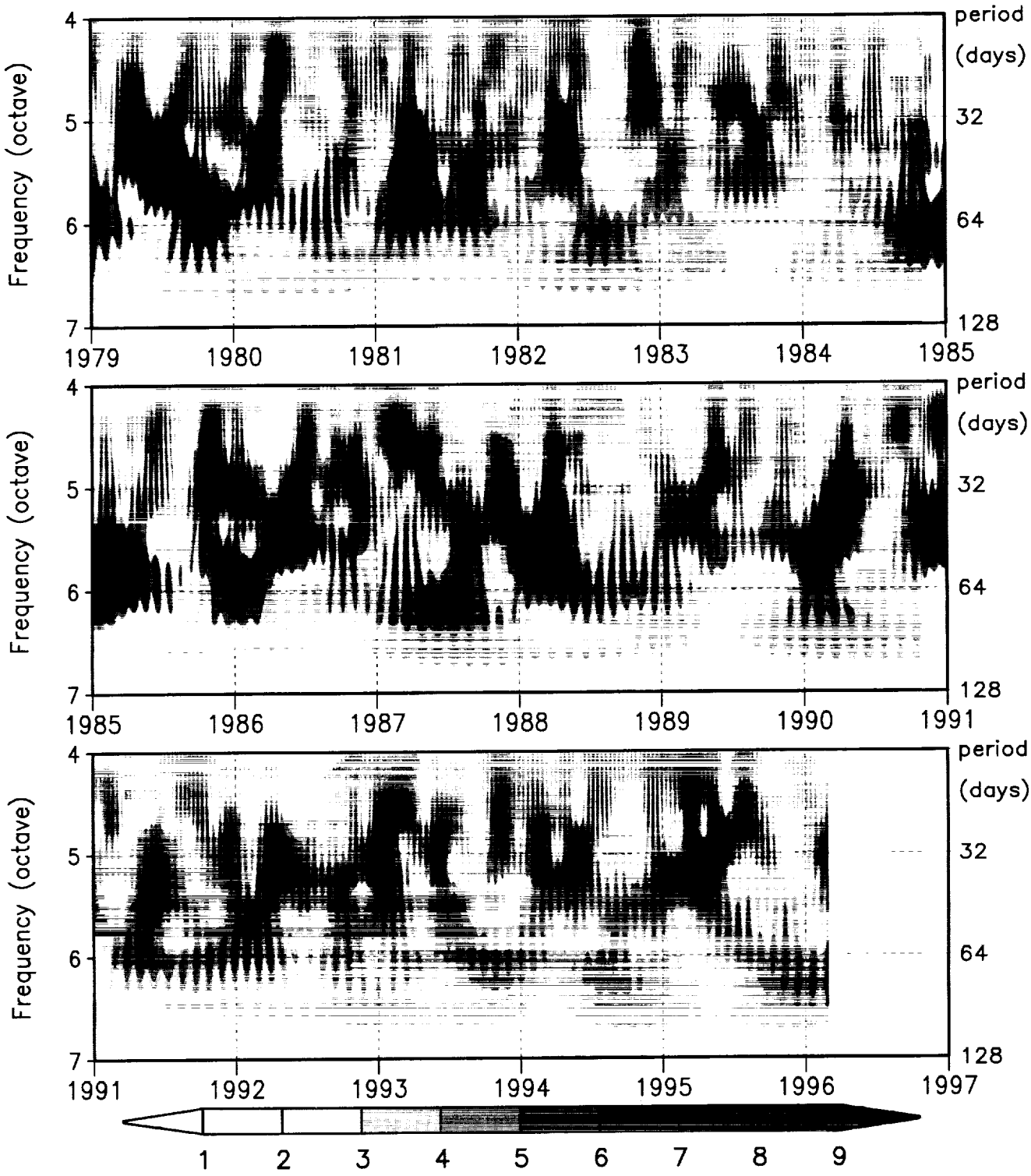

Figure 93: Time-frequency representation of the modulus of the the complex Morlet wavelet coefficients based on the first complex EOF of the 200 mb velocity potential filed from the reanalysis. The left ordinate is frequency in octive, and the right ordinate is period in day.

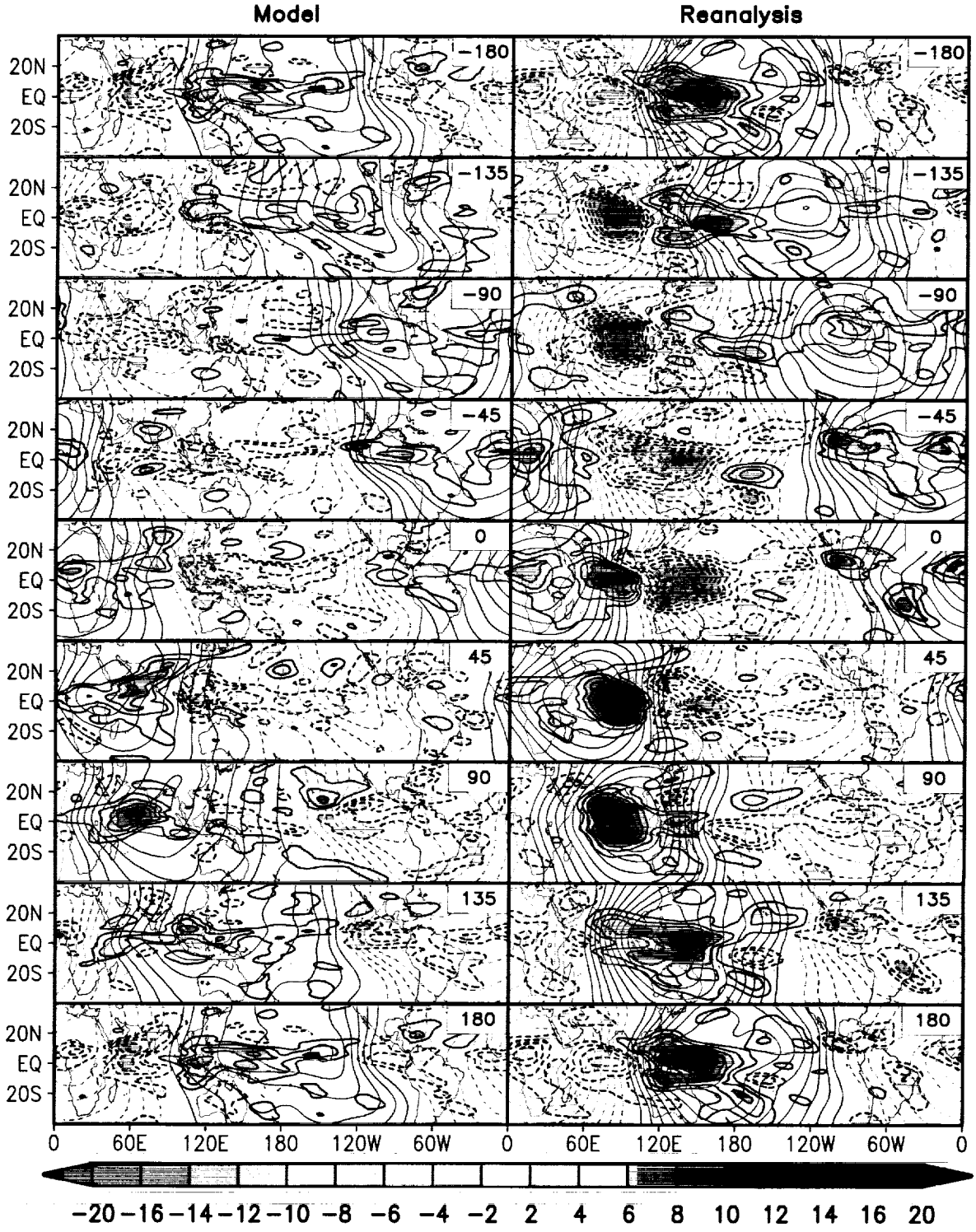

Figure 94: Composite anomalies of OLR and 200mb velocity potential at times of amplitude of the first component of 200mb velocity potential is larger than one standard deviation. The contour is for the velocity potential and the negative values are dashed. Shading is for OLR. Units are W m^{-2}.

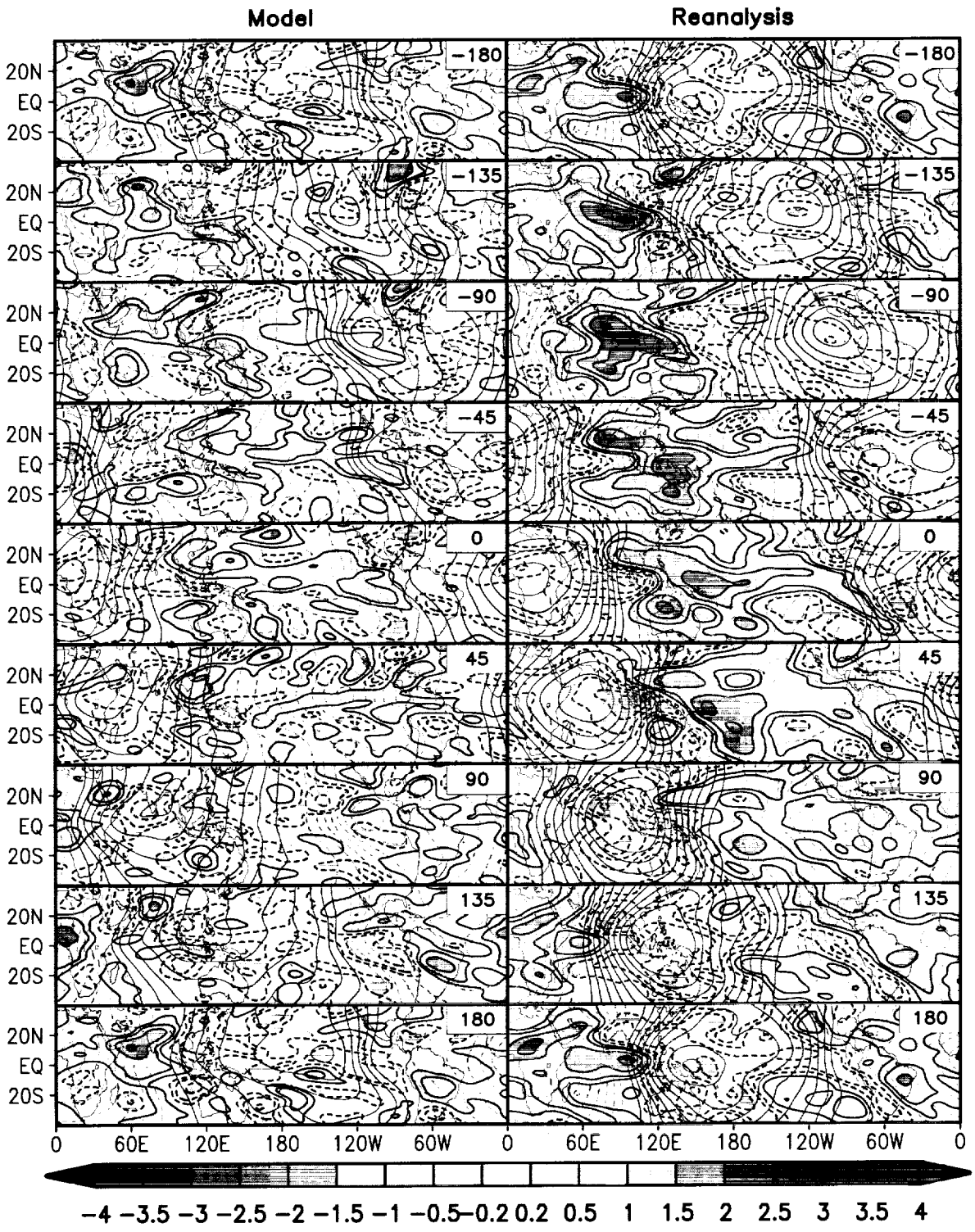

Figure 95: Composite anomalies of TPW and 200mb velocity potential at times of amplitude of the first component of 200mb velocity potential is larger than one standard deviation. The contour is for the velocity potential and the negative values are dashed. Shading is for TPW. Units are km m^{-2}.

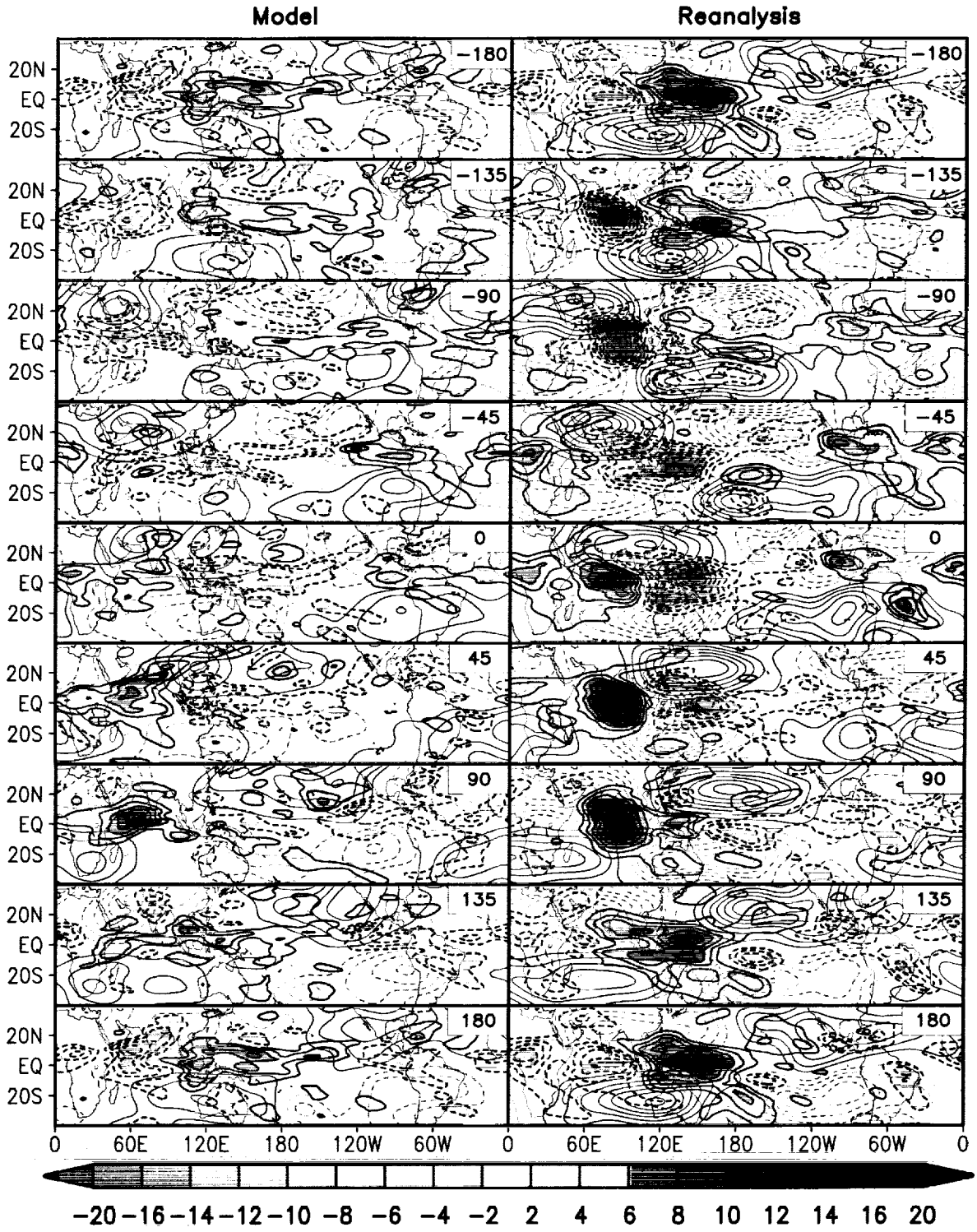

Figure 96: Composite anomalies of OLR and 200mb streamfunction at times of amplitude of the first component of velocity potential at 200mb is larger than one standard deviation. The contour is for the streamfunction and the negative values are dashed. Shading is for OLR. Units are W m^{-2}.

Previous Volumes in This Series

Volume 1 *September 1994*	Documentation of the Goddard Earth Observing System (GEOS) general circulation model - Version 1 **L.L. Takacs, A. Molod, and T. Wang**
Volume 2 *October 1994*	Direct solution of the implicit formulation of fourth order horizontal diffusion for gridpoint models on the sphere **Y. Li, S. Moorthi, and J.R. Bates**
Volume 3 *December 1994*	An efficient thermal infrared radiation parameterization for use in general circulation models **M.-D. Chou and M.J. Suarez**
Volume 4 *January 1995*	Documentation of the Goddard Earth Observing System (GEOS) Data Assimilation System - Version 1 **James Pfaendtner, Stephen Bloom, David Lamich, Michael Seablom, Meta Sienkiewicz, James Stobie, and Arlindo da Silva**
Volume 5 *April 1995*	Documentation of the Aries-GEOS dynamical core: Version 2 **Max J. Suarez and Lawrence L. Takacs**
Volume 6 *April 1995*	A Multiyear Assimilation with the GEOS-1 System: Overview and Results **Siegfried Schubert, Chung-Kyu Park, Chung-Yu Wu, Wayne Higgins, Yelena Kondratyeva, Andrea Molod, Lawrence Takacs, Michael Seablom, and Richard Rood**
Volume 7 *September 1995*	Proceedings of the Workshop on the GEOS-1 Five-Year Assimilation **Siegfried D. Schubert and Richard B. Rood**
Volume 8 *March 1996*	Documentation of the Tangent Linear Model and Its Adjoint of the Adiabatic Version of the NASA GEOS-1 C-Grid GCM: Version 5.2 **Weiyu Yang and I. Michael Navon**

Volume 9 *March 1996*	Energy and Water Balance Calculations in the Mosaic LSM **Randal D. Koster and Max J. Suarez**
Volume 10 *April 1996*	Dynamical Aspects of Climate Simulations Using the GEOS General Circulation Model **Lawrence L. Takacs and Max J. Suarez**
Volume 11 *May 1997*	Documentation of the Tangent Linear and its Adjoint Models of the Relaxed Arakawa-Schubert Moisture Parameterization Package of the NASA GEOS-1 GCM (Version 5.2) **Weiyu Yang I. Michael Navon, and Ricardo Todling**
Volume 12 *August 1997*	Comparison of Satellite Global Rainfall Algorithms **Alfred T.C. Chang and Long S. Chiu**
Volume 13 *December 1997*	Interannual Variability and Potential Predictability in Reanalysis Products **Wie Ming and Siegfried D. Schubert**
Volume 14 *August 1998*	A Comparison of GEOS Assimilated Data with FIFE Observations **Michael G. Bosilovich and Siegfried D. Schubert**
Volume 15 *June 1999*	A Solar Radiation Parameterization for Atmospheric Studies **Ming-Dah Chou and Max J. Suarez**
Volume 16 *November 1999*	Filtering Techniques on a Stretched Grid General Circulation Model **Lawrence Takacs, William Sawyer, Max J. Suarez, and Michael S. Fox-Rabinowitz**
Volume 17 *July 2000*	Atlas of Seasonal Means Simulated by the NSIPP-1 Atmospheric GCM **Julio T. Bacmeister, Philip J. Pegion, Siegfried D. Schubert, and Max J. Suarez**
Volume 18 *December 2000*	An Assessment of the Predictability of Northern Winter Seasonal Means with the NSIPP 1 AGCM **Philip J. Pegion, Siegfried D. Schubert, and Max J. Suarez**

Volume 19
July 2001

A Thermal Infrared Radiation Parameterization for Atmospheric Studies

Ming-Dah Chou, Max J. Suarez, Xin-Zhong, Michael M.-H. Yan

REPORT DOCUMENTATION PAGE

Form Approved
OMB No. 0704-0188

1. AGENCY USE ONLY *(Leave blank)*	2. REPORT DATE	3. REPORT TYPE AND DATES COVERED
	August 2001	Technical Memorandum

4. TITLE AND SUBTITLE
Technical Report Series on Global Modeling and Data Assimilation
Volume 20—The Climate of the FVCCM–3 Model

5. FUNDING NUMBERS
Code 971

6. AUTHOR(S)
Yehui Chang, Siegfried D. Schubert, Shian-Jiann Lin, Sharon Nebuda, and Bo-Wen Shen

7. PERFORMING ORGANIZATION NAME(S) AND ADDRESS (ES)
Goddard Space Flight Center
Greenbelt, Maryland 20771

8. PEFORMING ORGANIZATION REPORT NUMBER
2001–03504–0

9. SPONSORING / MONITORING AGENCY NAME(S) AND ADDRESS (ES)
National Aeronautics and Space Administration
Washington, DC 20546-0001

10. SPONSORING / MONITORING AGENCY REPORT NUMBER
TM–2001–104606, Vol. 20

11. SUPPLEMENTARY NOTES
Y. Chang, S. Nebuda, and B-W. Shen: General Sciences Corporation, Laurel, Maryland.
S. D. Schubert and S.-J. Lin: Data Assimilation Office, NASA GSFC, Greenbelt, Maryland

12a. DISTRIBUTION / AVAILABILITY STATEMENT
Unclassified–Unlimited
Subject Category: 46
Report available from the NASA Center for AeroSpace Information,
7121 Standard Drive, Hanover, MD 21076-1320. (301) 621-0390.

12b. DISTRIBUTION CODE

13. ABSTRACT *(Maximum 200 words)*

This document describes the climate of version 1 of the NASA-NCAR model developed at the Data Assimilation Office (DAO). The model consists of a new finite-volume dynamical core and an implementation of the NCAR climate community model (CCM–3) physical parameterizations. The version of the model examined here was integrated at a resolution of 2 degrees latitude by 2.5 degrees longitude and 32 levels. The results are based on asimulation that was forced with observed sea surface temperature and sea ice for the period 1979–1995, and are compared with NCEP/NCAR reanalyses and various other observational data sets. The results include an assessment of seasonal means, subseasonal transients including the Madden Julian Oscillation, and interannual variability. The quantities include zonal and meridional winds, temperature, specific humidity, geopotential height, stream function, velocity potential, precipitation, sea level pressure, and cloud radiative forcing.

14. SUBJECT TERMS
model climate, NASA-NCAR model, interannual variability, intraseasonal variability, seasonal means, Madden–Julian Oscillation

15. NUMBER OF PAGES
125

16. PRICE CODE

17. SECURITY CLASSIFICATION OF REPORT	18. SECURITY CLASSIFICATION OF THIS PAGE	19. SECURITY CLASSIFICATION OF ABSTRACT	20. LIMITATION OF ABSTRACT
Unclassified	Unclassified	Unclassified	UL